



Politecnico  
di Bari

Department of Mechanics, Mathematics and Management  
MECHANICAL AND MANAGEMENT ENGINEERING

Ph.D. Program

SSD: ING-IND/16 MANUFACTURING TECHNOLOGY AND  
SYSTEMS – ING-IND/13 APPLIED MECHANICS

**Final Dissertation**

---

Development of a predictive method of  
the response to shock loads of a  
spacecraft's structure

---

by

Ranieri Ada

Supervisors:

Prof. Michele Dassisti

Prof. Leonardo Soria

Prof. Giuseppe Carbone

*Coordinator of Ph.D. Program:*

*Prof. Giuseppe Casalino*

---



Politecnico  
di Bari

Department of Mechanics, Mathematics and Management

MECHANICAL AND MANAGEMENT ENGINEERING

Ph.D. Program

SSD: ING-IND/16– ING-IND/13

**Final Dissertation**

---

Development of a predictive method of the  
response to shock loads of a spacecraft's  
structure

---

by

Ranieri Ada



---

Referees:

Prof. Maria Cinefra

Dr. Gonalo Nuno Mendes  
da Costa Rodrigues

Supervisors:

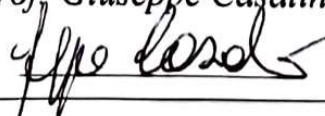
Prof. Michele Dassisti

Prof. Leonardo Soria

Prof. Giuseppe Carbone

*Coordinator of Ph.D. Program:*

*Prof. Giuseppe Casalino*



---

Course n°37, 01/11/2021-31/10/2024



LIBERATORIA PER L'ARCHIVIAZIONE DELLA TESI DI DOTTORATO

Al Magnifico Rettore  
del Politecnico di Bari

Il/la sottoscritto/a Ada Ranieri nato/a a Bari il 21/01/1997

residente a Bari in via XXIV Maggio, 36 e-mail ada210197@gmail.com

iscritto al 3° anno di Corso di Dottorato di Ricerca in Ingegneria Meccanica ciclo XXXVII

ed essendo stato ammesso a sostenere l'esame finale con la prevista discussione della tesi dal titolo:

Sviluppo di una metodologia predittiva della risposta ai carichi di shock sulla struttura di un satellite

**DICHIARA**

- 1) di essere consapevole che, ai sensi del D.P.R. n. 445 del 28.12.2000, le dichiarazioni mendaci, la falsità negli atti e l'uso di atti falsi sono puniti ai sensi del codice penale e delle Leggi speciali in materia, e che nel caso ricorressero dette ipotesi, decade fin dall'inizio e senza necessità di nessuna formalità dai benefici conseguenti al provvedimento emanato sulla base di tali dichiarazioni;
- 2) di essere iscritto al Corso di Dottorato di ricerca Ingegneria Meccanica ciclo XXXVII corso attivato ai sensi del "Regolamento dei Corsi di Dottorato di ricerca del Politecnico di Bari", emanato con D.R. n.286 del 01.07.2013;
- 3) di essere pienamente a conoscenza delle disposizioni contenute nel predetto Regolamento in merito alla procedura di deposito, pubblicazione e autoarchiviazione della tesi di dottorato nell'Archivio Istituzionale ad accesso aperto alla letteratura scientifica;
- 4) di essere consapevole che attraverso l'autoarchiviazione delle tesi nell'Archivio Istituzionale ad accesso aperto alla letteratura scientifica del Politecnico di Bari (IRIS-POLIBA), l'Ateneo archiverà e renderà consultabile in rete (nel rispetto della Policy di Ateneo di cui al D.R. 642 del 13.11.2015) il testo completo della tesi di dottorato, fatta salva la possibilità di sottoscrizione di apposite licenze per le relative condizioni di utilizzo (di cui al sito <http://www.creativecommons.it/Licenze>), e fatte salve, altresì, le eventuali esigenze di "embargo", legate a strette considerazioni sulla tutelabilità e sfruttamento industriale/commerciale dei contenuti della tesi, da rappresentarsi mediante compilazione e sottoscrizione del modulo in calce (Richiesta di embargo);
- 5) che la tesi da depositare in IRIS-POLIBA, in formato digitale (PDF/A) sarà del tutto identica a quelle **consegnate**/inviata/da inviarsi ai componenti della commissione per l'esame finale e a qualsiasi altra copia depositata presso gli Uffici del Politecnico di Bari in forma cartacea o digitale, ovvero a quella da discutere in sede di esame finale, a quella da depositare, a cura dell'Ateneo, presso le Biblioteche Nazionali Centrali di Roma e Firenze e presso tutti gli Uffici competenti per legge al momento del deposito stesso, e che di conseguenza va esclusa qualsiasi responsabilità del Politecnico di Bari per quanto riguarda eventuali errori, imprecisioni o omissioni nei contenuti della tesi;
- 6) che il contenuto e l'organizzazione della tesi è opera originale realizzata dal sottoscritto e non compromette in alcun modo i diritti di terzi, ivi compresi quelli relativi alla sicurezza dei dati personali; che pertanto il Politecnico di Bari ed i suoi funzionari sono in ogni caso esenti da responsabilità di qualsivoglia natura: civile, amministrativa e penale e saranno dal sottoscritto tenuti indenni da qualsiasi richiesta o rivendicazione da parte di terzi;
- 7) che il contenuto della tesi non infrange in alcun modo il diritto d'Autore né gli obblighi connessi alla salvaguardia di diritti morali od economici di altri autori o di altri aventi diritto, sia per testi, immagini, foto, tabelle, o altre parti di cui la tesi è composta.

Luogo e data Bari, 27/12/2024

Firma \_\_\_\_\_

Il/La sottoscritto, con l'autoarchiviazione della propria tesi di dottorato nell'Archivio Istituzionale ad accesso aperto del Politecnico di Bari (POLIBA-IRIS), pur mantenendo su di essa tutti i diritti d'autore, morali ed economici, ai sensi della normativa vigente (Legge 633/1941 e ss.mm.ii.),

**CONCEDE**

- al Politecnico di Bari il permesso di trasferire l'opera su qualsiasi supporto e di convertirla in qualsiasi formato al fine di una corretta conservazione nel tempo. Il Politecnico di Bari garantisce che non verrà effettuata alcuna modifica al contenuto e alla struttura dell'opera.
- al Politecnico di Bari la possibilità di riprodurre l'opera in più di una copia per fini di sicurezza, back-up e conservazione.

Luogo e data Bari, 27/12/2024

Firma \_\_\_\_\_



# Abstract

This thesis addresses one of the most pressing challenges in satellite development: accurately predicting shock loads during launch to optimize structural design and reduce the need for costly and time-consuming testing. As satellites are exposed to severe dynamic loads from rocket stage separations and pyrotechnic events, ensuring resilience against these forces is crucial for mission success. Traditional empirical methods for shock load prediction often rely on conservative assumptions, leading to over-design and added costs. This research, conducted in collaboration with SITAEL SpA and supported by insights and tools from the European Space Agency (ESA), introduces a novel methodology for more precise shock load prediction. The proposed model, based on modal decomposition and transfer function analysis, enables engineers to calculate shock transmissibility from low to high frequency spectrum, overcoming the limitations of empirical methods. The methodology was initially validated through simulations on simple 2-DOF systems and subsequently applied to the complex ShockSat case study, an open-source satellite project by NASA. Simulations carried out during a research period at ESA provided critical industry insights and further refined the model's accuracy and practical relevance. These simulations revealed the model's capability to predict shock responses in real satellite structures, offering potential design optimizations to mitigate shock effects. While experimental validation remains a future goal, this thesis establishes a robust foundation for advancing shock analysis in aerospace engineering. By shifting away from conservative assumptions toward more accurate prediction, the research holds promise for reducing dependency on extensive physical testing, ultimately leading to more efficient and sustainable satellite development. As the space industry places greater emphasis on cost-effectiveness and reliability, this predictive shock model meets the needs of today's market, opening up new possibilities for building more resilient spacecraft and making the design process more efficient.

**Keywords:** Shock Load Prediction, Modal Decomposition, Transfer Function Analysis, Shock Response Spectrum (SRS), Mechanical Environmental Shock Testing.

# Contents

|  |           |
|--|-----------|
| Abstract   | i         |
| List of Figures  | xi        |
| List of Tables   | xii       |
| Introduction   | 1         |
| List of Symbols  | 1         |
| <b>1 State-of-art of shock analysis: Deterministic and data-driven methods</b> | <b>7</b>  |
| 1.0.1 Numerical and experimental   | 9         |
| 1.1 Model-Based Techniques for Shock Environment Prediction                    | 11        |
| 1.1.1 From Deterministic to Statistical methods                                | 11        |
| 1.1.2 Stochastic methods   | 14        |
| 1.2 Data-Driven Techniques for Shock Environment Prediction                    | 15        |
| 1.2.1 The Role of Digital Twins in Data-Driven Models                          | 17        |
| 1.3 Hybrid Approaches: Combining Model-Based and Data-Driven Techniques        | 19        |
| <b>2 Shock Phenomena: an Overview</b>  | <b>21</b> |
| 2.1 Introduction to Vibration Analysis and Shock Response                      | 22        |
| 2.1.1 Elastic continuum viewpoint - Wave Motion                                | 23        |
| 2.1.2 Macroscopic viewpoint - Modal Analysis Using Mass-Spring-Damper Models   | 23        |
| 2.2 Dynamics of Single-Degree-of-Freedom Systems                               | 24        |
| 2.2.1 Free Vibration of an Undamped System                                     | 25        |
| 2.2.2 Damped Free Vibration  | 25        |
| 2.2.3 Forced Vibration   | 26        |
| 2.3 Response of Single-Degree-of-Freedom Systems to Nonperiodic Excitations    | 27        |

|          |   |           |
|----------|---|-----------|
| 2.3.1    | The Unit Pulse Function . . . . .                                     | 28        |
| 2.3.2    | The Unit Step Function . . . . .                                      | 31        |
| 2.3.3    | The Unit Ramp Function . . . . .                                      | 31        |
| 2.3.4    | Response to arbitrary excitations, the convolution integral . . . . . | 32        |
| 2.4      | Modal Analysis on MDOF Systems . . . . .                              | 34        |
| 2.4.1    | Free Vibration: Eigenvalue Problem . . . . .                          | 34        |
| 2.4.2    | Modal Superposition Method . . . . .                                  | 36        |
| 2.5      | Frequency Response Function (FRF) . . . . .                           | 37        |
| 2.6      | Transfer Function and Modal Decomposition . . . . .                   | 38        |
| 2.7      | Partial Fraction Expansion and FRF . . . . .                          | 39        |
| 2.8      | Modal parameters . . . . .  | 40        |
| 2.8.1    | The residue . . . . .   | 40        |
| 2.8.2    | Alternate Definition of the Residue . . . . .                         | 40        |
| 2.8.3    | The modal participation factor . . . . .                              | 41        |
| 2.8.4    | Modal Effective Mass . . . . .  | 42        |
| 2.9      | Transitioning from Low to High Frequencies . . . . .                  | 42        |
| 2.9.1    | Local Mode Phase Reconstruction . . . . .                             | 42        |
| 2.9.2    | Virtual Mode Synthesis . . . . .                                      | 44        |
| 2.10     | Statistical Energy Analysis . . . . .                                 | 45        |
| 2.10.1   | Wave Propagation in Plates . . . . .                                  | 45        |
| 2.10.2   | Fundamental Concepts of SEA . . . . .                                 | 48        |
| 2.10.3   | Applying SEA to Complex Systems . . . . .                             | 51        |
| <b>3</b> | <b>Shock Response Spectrum</b> . . . . .                              | <b>57</b> |
| 3.1      | A bit of history . . . . .  | 58        |
| 3.2      | Definition of SRS . . . . .   | 59        |
| 3.3      | SRS Analysis and Mathematical Derivation . . . . .                    | 60        |
| 3.3.1    | SRS Analysis for SDOF Systems . . . . .                               | 60        |
| 3.3.2    | Shock Response Spectrum for SDOF . . . . .                            | 61        |
| 3.3.3    | MDOF Systems and SRS . . . . .  | 62        |
| 3.4      | SRS synthesis . . . . .   | 63        |
| 3.4.1    | Time-Domain Synthesis Methods . . . . .                               | 65        |
| 3.5      | Application of SRS Methods to SDOF Systems . . . . .                  | 67        |
| 3.5.1    | LTI Single-Degree-of-Freedom System . . . . .                         | 68        |
| 3.5.2    | Viscoelastic Single-Degree-of-Freedom System . . . . .                | 70        |
| <b>4</b> | <b>Shock Analysis and Testing in Industry</b> . . . . .               | <b>77</b> |
| 4.1      | Industry Standards and Challenges . . . . .                           | 78        |
| 4.1.1    | The V Model . . . . .   | 79        |
| 4.1.2    | Types of Mechanical Shocks and Sources . . . . .                      | 80        |
| 4.1.3    | Shock Test Methods and Facilities . . . . .                           | 83        |

---

|          |   |            |
|----------|---|------------|
| 4.2      | Case Study: Multi-launcher Platform . . . . .                 | 85         |
| 4.2.1    | Mechanical properties . . . . .                               | 85         |
| 4.2.2    | Modal analysis and resonance search . . . . .                 | 88         |
| 4.2.3    | Damping evaluation . . . . .                                  | 88         |
| 4.3      | Experimental set up . . . . .                                 | 89         |
| 4.3.1    | Instrumentation . . . . .                                     | 92         |
| 4.3.2    | Input and tolerances . . . . .                                | 92         |
| 4.3.3    | Pass/Fail criteria . . . . .                                  | 93         |
| 4.4      | Shock prediction using Empirical method . . . . .             | 94         |
| <b>5</b> | <b>Shock Response Prediction in Mechanical Structures</b>     | <b>100</b> |
| 5.1      | R-FRFs and Shock Transmissibility . . . . .                   | 101        |
| 5.2      | Application of the method on simple systems . . . . .         | 103        |
| 5.2.1    | 2-DOF System . . . . .  | 103        |
| 5.3      | ShockSat Case Study . . . . .                                 | 107        |
| 5.3.1    | Extrapolation of Modal Data and computation of FRFs . . . . . | 107        |
| 5.3.2    | Shock Transmissibility . . . . .                              | 115        |
| 5.3.3    | Input identification . . . . .                                | 117        |
| 5.3.4    | Shock Response Calculation . . . . .                          | 118        |
| 5.4      | Shock through composites . . . . .                            | 121        |
| 5.4.1    | Comparison of FEM and MUL2 . . . . .                          | 123        |
| 5.4.2    | Aluminium Isotropic Plate . . . . .                           | 124        |
| 5.4.3    | Composite Orthotropic Plate . . . . .                         | 125        |
|          | <b>Conclusions</b>  | <b>130</b> |
|          | <b>Acknowledgment</b>   | <b>135</b> |
|          | <b>Appendix A</b>   | <b>136</b> |
|          | <b>References</b>   | <b>152</b> |



# Nomenclature

|                          |   |
|--------------------------|---|
| $\alpha_j, \alpha_i$     | Angles between adjoining sections in a shock path |
| $\ddot{\mathbf{x}}(t)$   | Synthesized acceleration in the time domain       |
| $\ddot{u}_b(t)$          | Base acceleration input in a shock event          |
| $\ddot{x}(t)$            | Absolute acceleration of mass in a system         |
| $\Delta dB$              | Slope in decibels per octave                      |
| $\lambda_r$              | Complex root of the system for the $r$ -th mode   |
| $\mathbf{x}_{\max}$      | Maximum displacement vector after shock event     |
| $\omega$                 | Angular frequency                                 |
| $\omega_r$               | Natural frequency of the $r$ -th mode             |
| $\phi_m$                 | Phase angle for the $m$ -th wavelet frequency     |
| $\psi_r$                 | Mode shape vector for the $r$ -th mode            |
| CoG                      | Center of gravity coordinates                     |
| $I_{xx}, I_{yy}, I_{zz}$ | Moments of inertia around principal axes          |
| $I_{xy}, I_{yz}, I_{zx}$ | Product of inertia terms                          |
| MoI                      | Moment of Inertia for composite materials         |
| $Q_{axial}, Q_{radial}$  | Shock load inputs for axial and radial directions |
| $\xi_m$                  | Damping ratio for the $m$ -th wavelet             |
| $\zeta$                  | Damping ratio                                     |
| $A_m$                    | Amplitude of wavelet in synthesis                 |

---

|                  |  |
|------------------|--|
| $Att_{Distance}$ | Distance attenuation factor  |
| $Att_{Joint}$    | Joint attenuation factor   |
| $B(s)$           | Dynamic stiffness matrix in the Laplace domain                       |
| $c$              | Damping coefficient  |
| $COR$            | Synthesis Correlation Coefficient                                    |
| $dB$             | Decibel level  |
| $e, f$           | Section orientation factors for axial and radial directions          |
| $E(t)$           | Envelope function for damped sinusoids                               |
| $f$              | Frequency in Hz  |
| $F(s)$           | Force vector in the Laplace domain                                   |
| $f_n$            | Resonant frequency for the $n$ -th mode                              |
| $f_{critical}$   | Critical frequency where damping is highest                          |
| $H(s)$           | Transfer function matrix   |
| $H_{11}, H_{21}$ | Partitions of the FRF matrix $H(i\omega)$                            |
| $k$              | Spring stiffness   |
| $K_{Joint}$      | Configuration factor for joint attenuation                           |
| $K_{Struct}$     | Configuration factor for structure attenuation                       |
| $L_i$            | Adjusted length for distance attenuation based on section properties |
| $L_r$            | Modal participation vector for the $r$ -th mode                      |
| $m$              | Mass   |
| $N_m$            | Number of oscillations in a wavelet component                        |
| $Q$              | Quality factor   |
| $r_{ax}$         | Axial ratio for attenuation calculation                              |
| $r_{rad}$        | Radial ratio for attenuation calculation                             |

- 
- $s$  Complex frequency variable in the Laplace domain
- $S_A(\omega)$  Peak response function in SRS calculation
- $SRS_{in}$  Input Shock Response Spectrum
- $SRS_{out}$  Output Shock Response Spectrum
- $T$  Time duration for a synthesized waveform
- $T(i\omega)$  Global transmissibility function in the frequency domain
- $T(i\omega)$  Global transmissibility in modal analysis
- $T_{shock}$  Shock transmissibility
- $t_{dm}$  Delay time for wavelet component in synthesis
- $X(s)$  Displacement vector in the Laplace domain
- $z(t)$  Relative displacement in the system

# List of Figures

|      |   |    |
|------|---|----|
| 1    | Launch of a rocket, render . . . . .  | 1  |
| 2    | Space launch system booster separation that causes shock loads . . . . .  | 2  |
| 3    | Shock signal, represented in form of an acceleration in the time domain, caused by a pyrotechnic explosion . . . . .              | 3  |
| 4    | Render of the Multi-Application Minisatellite with a recurrent platform, compatible for multiple launchers and missions . . . . . | 5  |
| 1.1  | Shock prediction paradigm . . . . .   | 9  |
| 1.2  | Relationship between numerical and experimental . . . . .   | 10 |
| 1.3  | Close-up on shock prediction approaches . . . . .   | 11 |
| 1.4  | From deterministic to statistical . . . . .   | 13 |
| 1.5  | Life Cycle Assessment in Space ref: ESA . . . . .   | 19 |
| 2.1  | Arbitrary excitation . . . . .  | 33 |
| 2.2  | Energy flow in single and coupled subsystems. . . . .   | 49 |
| 3.1  | SRS graphical representation . . . . .  | 59 |
| 3.2  | synthesised time history for the given shock input. . . . .   | 66 |
| 3.3  | Synthesized SRS comparison. . . . .   | 67 |
| 3.4  | Pyrotechnic signal derived by an experimental shock test . . . . .  | 68 |
| 3.5  | SRS derived by the pyrotechnic signal . . . . .   | 68 |
| 3.6  | SRS comparison between the test-derived SRS and the synthesised SRS using the three synthesis methods . . . . .                   | 69 |
| 3.7  | Single-Degree-of-Freedom Mass-Spring-Damper linear system . . . . .   | 69 |
| 3.8  | Base input acceleration in SRS form . . . . .   | 70 |
| 3.9  | Matlab lsim for LTI system . . . . .  | 70 |
| 3.10 | SRS response of a SDOF LTI system to a shock base input . . . . .   | 71 |
| 3.11 | Analytical solution of the sdof LTI system for comparison . . . . .   | 71 |
| 3.12 | SRS response of a SDOF LTI system to a shock base input, comparison with the analytical solution . . . . .                        | 72 |
| 3.13 | Standard linear viscoelastic model . . . . .  | 72 |

|      |  |     |
|------|--|-----|
| 3.14 | Relaxation and creep functions for the standard linear viscoelastic model. . . . .   | 73  |
| 3.15 | Matlab lsim for Viscoelastic linear system . . . . .   | 74  |
| 3.16 | SRS response of a SDOF viscoelastic linear system to a shock base input . . . . .  | 74  |
| 3.17 | Analytical solution of the sdof viscoelastic linear system for comparison . . . . .  | 74  |
| 3.18 | SRS response of a SDOF viscoelastic linear system to a shock base input, comparison with the analytical solution . . . . . | 75  |
| 4.1  | Honeycomb materials properties . . . . .   | 80  |
| 4.2  | Ground shock tests and shocks in service life . . . . .  | 81  |
| 4.3  | Fairing jettisoning . . . . .  | 82  |
| 4.4  | Clampband Release System . . . . .   | 83  |
| 4.5  | SHOGUN Test . . . . .  | 84  |
| 4.6  | VESTA Test . . . . .   | 84  |
| 4.7  | Drawing of the Structural Model (SM) . . . . .   | 86  |
| 4.8  | Isotropic materials properties . . . . .   | 86  |
| 4.9  | Honeycomb materials properties . . . . .   | 86  |
| 4.10 | Orthotropic materials properties . . . . .   | 87  |
| 4.11 | Composite materials list . . . . .   | 87  |
| 4.12 | Channel 5, bottom plate, x direction . . . . .   | 89  |
| 4.13 | Channel 5, bottom plate, y direction . . . . .   | 89  |
| 4.14 | Channel 38, top plate, x direction . . . . .   | 89  |
| 4.15 | Channel 38, top plate, y direction . . . . .   | 89  |
| 4.16 | Channel 5, bottom plate, z direction . . . . .   | 90  |
| 4.17 | Channel 38, top plate, z direction . . . . .   | 90  |
| 4.18 | Half-Power Damping Evaluation Method . . . . .   | 90  |
| 4.19 | Schematization of a possible experimental setup inspired by VESTA . . . . .  | 91  |
| 4.20 | Real experimental setup for pyrotechnic shock testing . . . . .  | 91  |
| 4.21 | Instrumentation plan, Bottom Plate, lower side . . . . .   | 93  |
| 4.22 | Instrumentation plan, Bottom Plate, upper side . . . . .   | 93  |
| 4.23 | Instrumentation plan, EP box . . . . .   | 94  |
| 4.24 | Shock load input plot . . . . .  | 95  |
| 4.25 | Test tolerances of +6/-3 dB . . . . .  | 95  |
| 4.26 | Load path example . . . . .  | 96  |
| 4.27 | $K_{Joint}$ definition . . . . .   | 97  |
| 4.28 | $K_{Struct}$ definition . . . . .  | 97  |
| 5.1  | Block Diagram of the roadmap for the validation of the methodology . . . . .   | 101 |
| 5.2  | Ground acceleration applied on a 2 dof mass-spring-damper system . . . . .   | 104 |

---

|      |  |     |
|------|--|-----|
| 5.3  | Frequency Response Function, H11 . . . . .   | 104 |
| 5.4  | Frequency Response Function, H12 . . . . .   | 104 |
| 5.5  | Frequency Response Function, H21 . . . . .   | 105 |
| 5.6  | Frequency Response Function, H22 . . . . .   | 105 |
| 5.7  | . . . . .  | 105 |
| 5.8  | Theoretical output via SRS . . . . .   | 106 |
| 5.9  | Theoretical output via Inverse Fast-Fourier Transform . . . . .  | 106 |
| 5.10 | ShockSat Physical model . . . . .  | 108 |
| 5.11 | ShockSat FEM model . . . . .   | 108 |
| 5.12 | Eigenvalues on the .f06 NASTRAN file . . . . .   | 109 |
| 5.13 | Eigenvectors on the .f06 NASTRAN file . . . . .  | 110 |
| 5.14 | SRS experimental output, channel 1 . . . . .   | 110 |
| 5.15 | Hammer Test on Shocksat . . . . .  | 111 |
| 5.16 | ShockSat Top Plate . . . . .   | 111 |
| 5.17 | ShockSat +X Panel . . . . .  | 112 |
| 5.18 | ShockSat +Y Panel . . . . .  | 112 |
| 5.19 | FRF of accelerometer 1, x direction . . . . .  | 113 |
| 5.20 | FRF of accelerometer 1, y direction . . . . .  | 113 |
| 5.21 | FRF of accelerometer 1, z direction . . . . .  | 113 |
| 5.22 | FRF of accelerometer 4, x direction . . . . .  | 114 |
| 5.23 | FRF of accelerometer 31, x direction . . . . .   | 114 |
| 5.24 | Pyroshock Tests performed on ShockSat . . . . .  | 115 |
| 5.25 | Shocksat Shock setup . . . . .   | 116 |
| 5.26 | Experimental SRS responses . . . . .   | 116 |
| 5.27 | Pyroshock Test on ShockSat . . . . .   | 117 |
| 5.28 | Synthesised input signal . . . . .   | 117 |
| 5.29 | Fast Fourier Transform input signal . . . . .  | 117 |
| 5.30 | Transmissibility obtained by analytical/experimental FRF . . . . .   | 119 |
| 5.31 | Output in time domain . . . . .  | 119 |
| 5.32 | Comparison between the experimental response and the prediction<br>obtained from modal data . . . . .        | 120 |
| 5.33 | Comparison between the experimental response and the prediction<br>obtained from experimental data . . . . . | 120 |
| 5.34 | Comparison between the theoretical outputs obtained by the time<br>domain method . . . . .                   | 120 |
| 5.35 | Half-sine pulse input . . . . .  | 123 |
| 5.36 | SRS of the half-sine pulse input . . . . .   | 123 |
| 5.37 | Clamped plate mesh on FEMAP . . . . .  | 124 |
| 5.38 | Natural frequencies comparison of the isotropic plate . . . . .  | 125 |
| 5.39 | Isotropic composite plate, FRF Analysis - Magnitude . . . . .  | 125 |

---

|      |   |     |
|------|---|-----|
| 5.40 | Isotropic composite plate, FRF Analysis - Phase . . . . .         | 125 |
| 5.41 | Transmissibility of the isotropic plate . . . . .                 | 126 |
| 5.42 | SRS output to half-sine input, isotropic plate . . . . .          | 126 |
| 5.43 | Natural frequencies comparison of the orthotropic plate . . . . . | 127 |
| 5.44 | Orthotropic composite plate, FRF Analysis - Magnitude . . . . .   | 127 |
| 5.45 | Orthotropic composite plate, FRF Analysis - Phase . . . . .       | 127 |
| 5.46 | Transmissibility of the orthotropic plate . . . . .               | 127 |
| 5.47 | SRS output to half-sine input, orthotropic plate . . . . .        | 128 |

# List of Tables

- 3.1 Shock load input . . . . . 66
- 3.2 Synthesis correlation coefficient . . . . . 67
  
- 4.1 Mechanical properties of the SM . . . . . 86
- 4.2 Shock load input values (Q=10) . . . . . 94



# Introduction



Figure 1: Launch of a rocket, render

The journey of satellite development and its impact on space exploration has taken off in remarkable ways since the 1970s. This period marked the beginning of a new era, transforming how we communicate, observe our planet, and even understand the universe. Satellites became essential tools, allowing us to collect data that informs everything from weather forecasts to environmental monitoring. Yet, sending these technological marvels into the unknown is fraught with challenges. Space is an extreme environment, and once we push beyond the protective veil of Earth's atmosphere, our satellites face harsh conditions. They are bombarded by intense radiation, extreme temperatures, and the vacuum of space itself. Given the immense costs involved in developing and launching these spacecraft, ensuring they can withstand these challenges is critical. Repairs in orbit are not a financially feasible option, for now. To prepare for the rigours of space, every satellite undergoes extensive testing to mimic the harsh realities of launch and operation. The launch phase is particularly intense, subjecting the spacecraft to a combination of mechanical, acoustic, thermal, and radiation stresses. However, the environmental testing process is not just necessary; it can also be time-consuming and expensive.

This has led engineers to seek more efficient ways to develop spacecraft. They use advanced mathematical models to predict how these structures will handle dynamic loads, hoping that these simulations will eliminate the need for major redesigns after testing. But getting these predictions right is vital. During launch, spacecraft experience a wide range of dynamic loads, with vibrations and shocks that vary greatly in intensity. At higher frequencies, traditional methods often fall short, making statistical approaches essential for understanding the forces at play. One of the most crucial tests is the shock test, which evaluates how well a satellite can endure the intense forces from sudden events, like when stages of a rocket separate or when the protective fairing is jettisoned. These moments generate extreme loads, largely due to pyrotechnic devices in the launch vehicle. The mechanical stresses can be brutal, and if a satellite isn't ready for them, the consequences can be disastrous [1–4]. In recent years, the space industry has really shifted focus toward making satellite launches more efficient and cost-effective. Companies like SpaceX are leading the way with reusable rockets, which are designed to return safely to Earth and be launched again. This approach not only reduces costs but also changes how we think about spacecraft durability. As we continue to explore and push the boundaries of what's possible in space, mastering the art of predicting and testing for extreme conditions will be essential. With reusable technology, the stakes are higher, and getting it right has never been more important for the future of space exploration.



Figure 2: Space launch system booster separation that causes shock loads

My research addresses the challenge of predicting shock loads on satellite structures by developing a virtual simulation methodology. This PhD project, conducted in collaboration with SITAEL SpA, an aerospace company, aims to establish a predictive shock model adaptable for multiple launchers and satellite

configurations. The goal is to optimize the design process while minimizing the number of experimental tests required. This project is part of an industrial PhD program, integrating theoretical advancements in shock analysis with both academic rigour and practical applications within the aerospace industry. Although the proposed methodology has not yet undergone experimental validation, it lays a foundation for future shock testing and design optimization. The final validation of the methodology will be carried out following the completion of my PhD, with shock tests planned according to the specifications we have developed. The aim of this research is to create a predictive shock analysis method that is both more accurate and less conservative than current industry standards, while remaining computationally efficient and straightforward to implement. By developing a versatile tool that can be tailored to various satellite configurations and launch vehicles, this research endeavours to optimize satellite design processes and reduce the need for costly experimental tests.

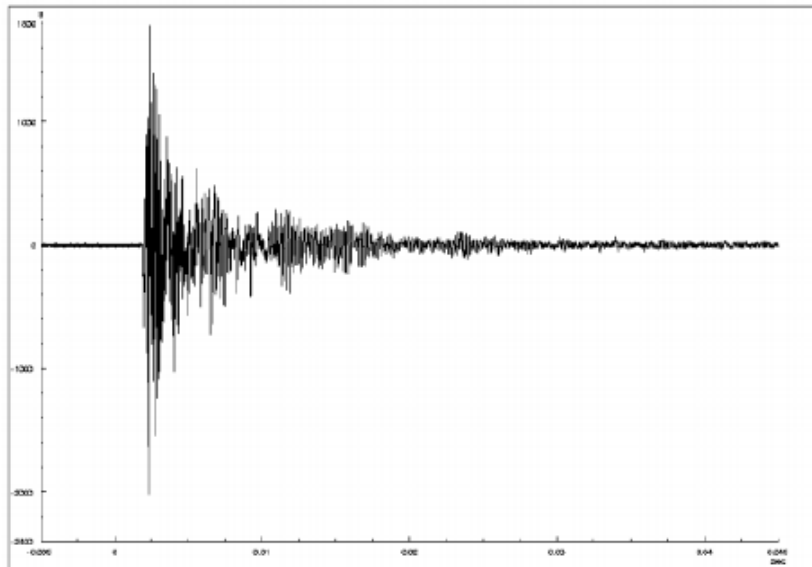


Figure 3: Shock signal, represented in form of an acceleration in the time domain, caused by a pyrotechnic explosion

This thesis is divided into several chapters that reflect the theoretical framework, industrial application, and the development of the shock prediction model. Chapter 1 provides a comprehensive overview of the state-of-the-art in shock analysis, highlighting both deterministic and data-driven methods. It traces the historical evolution of shock prediction techniques, beginning with early earthquake research and extending to modern aerospace applications. The chapter emphasizes the critical importance of predicting structural responses to dynamic loads throughout a wide frequency spectrum, illustrating how different methodologies serve this purpose. It

discusses the efficacy of traditional deterministic approaches at low frequencies and the need for statistical methods as frequencies increase, particularly in high-density modal environments. The text also introduces hybrid techniques that merge physical modelling with data-driven approaches, leveraging the strengths of both to enhance predictive capabilities. Additionally, the chapter explores the transformative role of Artificial Intelligence (AI) and Machine Learning (ML) in shock prediction, while addressing the challenges inherent in experimental and numerical methods. Ultimately, it sets the stage for understanding how these techniques can streamline spacecraft development processes and improve reliability during critical mission phases.

2 shows an extended overview of shock phenomena, focusing on the fundamental principles of vibration analysis and the response of mechanical systems to non periodic excitations, particularly shocks. For this chapter, the theoretical framework has been drawn from fundamental educational texts in vibration dynamics and vibroacoustic [5–13], providing a comprehensive basis for understanding shock phenomena and the response of mechanical systems to non-periodic excitations. It begins with an introduction to vibration analysis, followed by a discussion of wave motion and its relevance in shock contexts. The chapter then delves into modal analysis for single-degree-of-freedom (SDOF) systems, exploring the dynamic behaviour of these systems under shock loads. Furthermore, it extends to multi-degree-of-freedom (MDOF) systems, highlighting frequency response functions and modal decomposition techniques. The significance of modal parameters is addressed, along with an introduction to Statistical Energy Analysis (SEA), providing insights into energy distribution in complex systems. Lastly, the chapter covers methodologies for transitioning from low to high frequencies, establishing a framework for shock analysis applicable to various engineering contexts.

3 introduces the Shock Response Spectrum (SRS) as a critical tool in assessing system resilience to transient shock events. Beginning with the historical context, the chapter traces the evolution of SRS as a standardized method across various industries, from civil engineering to aerospace. A rigorous mathematical derivation of the SRS is presented for both SDOF and MDOF systems, emphasizing the importance of frequency response in shock analysis. Additionally, the chapter explores various time-domain synthesis methods, such as wavelets and damped sinusoids, comparing their effectiveness in replicating SRS input signals. These synthesised signals are subsequently applied to different system models, providing insight into the SRS practical applications and limitations in predicting shock responses across diverse systems.

4 investigates the industry standards for shock analysis, with a focus on the practices employed at SITAEL for the Multi-Application Minisatellite project. The chapter begins by introducing the V-Model as a framework for spacecraft development, outlining its role in managing systematic verification and validation at every design stage. The Structural Model (SM) of The Minisatellite

serves as a case study, where mechanical properties and shock response are examined through modal analysis and physical testing. The chapter proceeds to outline the shock test specifications, including the experimental setup, instrumentation, input conditions, and pass/fail criteria, which will guide future testing of the Minisatellite SM. Although the shock test for the Multi-Application Minisatellite has not yet been conducted, the methodology developed during this PhD provides a foundation for future experimental validation. Existing industrial shock testing methods are discussed, highlighting the technical challenges of simulating real-world shock conditions in a clean room setting and the limitations of current empirical methods, underlining the complexities involved in achieving accurate shock testing outcomes. The chapter also introduces the empirical methods traditionally used in industry to estimate shock loads, which serve as benchmarks for comparison with the proposed methodology. These empirical methods rely on conservative assumptions about the attenuation of shock loads through the satellite structure, often resulting in over-design and increased costs. A significant contribution of this research is the improvement of these empirical methods through a predictive shock model based on modal decomposition and transfer function analysis. This model, as demonstrated in later chapters, offers more accurate predictions of shock loads, facilitating optimised satellite designs that better balance performance with cost efficiency.



Figure 4: Render of the Multi-Application Minisatellite with a recurrent platform, compatible for multiple launchers and missions

5 introduces a novel predictive methodology for calculating the shock response of mechanical structures, aimed at improving the accuracy and reliability of traditional shock load estimation. The approach leverages modal decomposition and

transfer function analysis to calculate shock transmissibility and predict shock responses with greater precision, reducing the conservatism often associated with empirical methods. The methodology is validated through applications to both simple 2-DOF systems and complex case studies, including the ShockSat project, which serves as an open-source test-bed for shock prediction improvement. In 5.4.3 some snippets of the MATLAB code are shown. The chapter also explores shock propagation in composite materials, presenting Carrera's Unified Formulation (CUF) as an effective tool for capturing the intricate behaviour of aerospace composites under dynamic loads. Through comparative analyses of the proposed method and traditional industry standards, the chapter demonstrates the predictive model's ability to offer enhanced accuracy while optimising the design and testing process. By combining theoretical advancements with practical validation, this chapter marks a significant contribution to improving shock response prediction in aerospace engineering. In conclusion, this research provides a novel, predictive methodology for analysing shock loads in satellite structures, addressing the limitations of traditional empirical methods. Through simulations initially conducted on simple systems and later applied to the complex ShockSat case study, the methodology was rigorously tested and refined. These simulations were carried out during a visiting research period at the European Space Agency (ESA), where I was able to access industry-standard tools and collaborate with leading experts. By advancing a model that combines modal decomposition and transfer function analysis, this work contributes a more precise tool for shock prediction that holds the potential to optimize satellite design, reduce testing costs, and increase resilience. The simulations conducted on ShockSat, as well as collaborations with industry leaders like SITAEL and ESA, highlight the model's adaptability across different satellite configurations and missions. This thesis thus serves as both a theoretical and practical foundation for enhancing the efficiency and accuracy of shock analysis in aerospace engineering. Looking forward, the integration of predictive shock models in spacecraft design could drive more sustainable development practices, supporting the aerospace industry in meeting the challenges of an era marked by cost-effectiveness and increased demands for reliability in satellite missions.

# Chapter 1

## State-of-art of shock analysis: Deterministic and data-driven methods

### Contents

|       |  |    |
|-------|--|----|
| 1.0.1 | Numerical and experimental . . . . .   | 9  |
| 1.1   | Model-Based Techniques for Shock Environment Prediction . . . . .                          | 11 |
| 1.1.1 | From Deterministic to Statistical methods . . . . .  | 11 |
|       | Finite Element Method (FEM) in Vibro-Acoustic Analysis<br>of Composite Materials . . . . . | 13 |
| 1.1.2 | Stochastic methods . . . . .   | 14 |
| 1.2   | Data-Driven Techniques for Shock Environment Prediction . . . . .                          | 15 |
| 1.2.1 | The Role of Digital Twins in Data-Driven Models . . . . .                                  | 17 |
| 1.3   | Hybrid Approaches: Combining Model-Based and Data-Driven Tech-<br>niques . . . . .         | 19 |

Research on shocks began in the 1930s, focusing on the impact of earthquakes on buildings, which led to the concept of the shock response spectrum. Equipment testing gained momentum during World War II, and methods advanced further with the increased power of exciters, enabling the generation of synthetic shocks. In the 1970s, the advent of computerization brought another significant evolution, allowing tests to be conducted directly on exciters using the shock response spectrum [14]. In the aerospace industry, mechanical shock prediction and

testing are crucial not only for ensuring reliability during critical mission phases but also for enhancing the sustainability of spacecraft development. A promising approach in this context is identifying techniques that can accurately predict a spacecraft's structural response to dynamic loads across the entire frequency spectrum encountered during launch. Such methods, if integrated into the early design phase, could significantly reduce the need for mechanical environmental test campaigns, streamlining the development process and cutting costs. The prediction of mechanical responses, particularly across varying frequency bands—low, mid, and high—plays a vital role, as each range induces distinct structural behaviours. At low frequencies, deterministic models like Finite Element Method (FEM) are highly effective because they capture the first few natural modes of the structure. However, as the frequency increases, especially into the mid and high-frequency ranges, the behaviour becomes more complex due to modal density and overlap, leading to less predictable responses. This shift highlights the need for statistical methods that can handle the stochastic nature of high-frequency shock responses, reflecting the ongoing debate between deterministic and probabilistic approaches in aerospace engineering. Further complicating matters, the debate between finite element analysis (FEA) and simplified analytical methods, along with the balance between predictive software and physical testing, intersects with new predictive techniques such as model-based design and data-driven approaches. Traditional model-based methods, rooted in the physical characteristics of the spacecraft, are essential for early-stage predictions but often fall short in capturing the complexities of high-frequency dynamics. This gap is increasingly being addressed through Artificial Intelligence (AI) and Machine Learning (ML) technologies, which enhance the predictive power of Digital Twins (DT) and improve decision-making processes. These AI-driven methods align with the black box approach, where the system's dynamics are not fully known but can be learned from available data. By exciting the system with input signals and using output data to train models, AI and ML algorithms can predict how a spacecraft will respond under various dynamic conditions. However, reliance solely on black box methods has limitations, particularly when little is known about the underlying physics of the system. To address this, hybrid approaches, often referred to as grey box methods, combine rough physical knowledge of the system with data-driven techniques. This blend allows engineers to set up a preliminary model based on first principles or multi-body dynamics and refine it using data. Such hybrid models offer a balance between the flexibility of data-driven methods and the structural insights of traditional physics-based models, making them particularly valuable in aerospace applications where both accuracy and adaptability are critical. This grey box approach, known as system identification, enables engineers to learn model parameters dynamically while retaining the power to optimise other features based



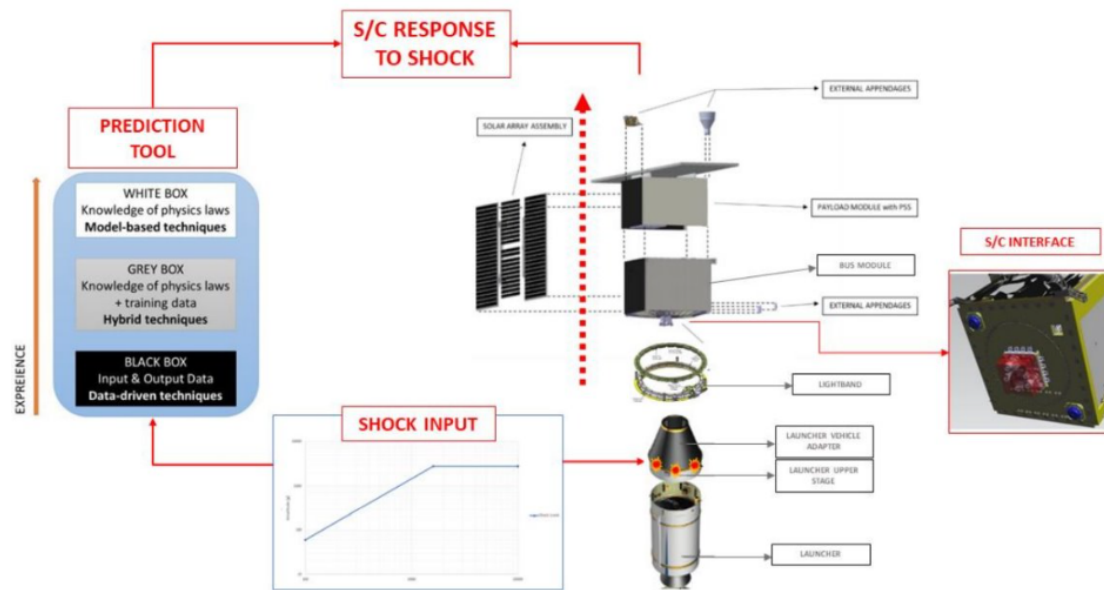


Figure 1.1: Shock prediction paradigm

on known system behaviour. In comparing these methods—model-based, data-driven, and hybrid—it becomes clear that each has its role in spacecraft shock prediction, depending on the frequency range and complexity of the system. At lower frequencies, where the system is more predictable, deterministic models are typically sufficient, but as the complexity grows with higher frequencies, more flexible, data-driven, or hybrid methods become necessary. By benchmarking these techniques, engineers can optimize their prediction strategies, combining the precision of traditional models with the adaptability of AI-driven solutions to meet the increasingly stringent demands of modern aerospace systems. Ultimately, the careful integration of these techniques into the design phase holds the potential to significantly enhance the sustainability and efficiency of spacecraft development by reducing the need for extensive physical testing and enabling more accurate predictions of dynamic responses.

### 1.0.1 Numerical and experimental

This section is dedicated to highlight the complementary roles of experimental and numerical approaches in structural analysis, particularly in aerospace applications. An effective integration of these methodologies can be achieved through an iterative, holistic approach, where low-fidelity numerical models are used in the initial stages to explore the parameter space and refine the design. These simplified models can iteratively feed into high-fidelity simulations, providing a

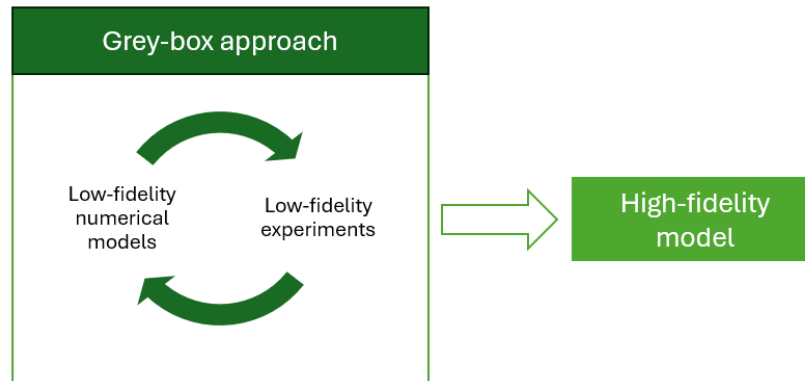


Figure 1.2: Relationship between numerical and experimental

cost-effective means to achieve an optimized balance between computational effort and predictive accuracy. The use of such a multi-tiered modelling strategy allows for the early identification of potential issues and accelerates convergence towards reliable high-fidelity results, thereby enhancing the robustness of structural validation processes and ensuring consistency between numerical predictions and experimental findings. However, both experimental and numerical approaches present significant challenges. Experimental methods often suffer from complex positioning requirements, limited instrumentation such as accelerometers, and difficulty in replicating exact launch conditions. Moreover, the static and dynamic properties can be affected by the use of dummy masses, reducing the accuracy of the experimental setup. On the other hand, numerical methods face challenges such as the need for linear approximations of shock propagation dynamics and the non-deterministic behaviour of the model at high-frequency ranges, which complicates accurate predictions. Additionally, numerical models often struggle with adequate damping estimation and boundary condition modeling, leading to uncertainties in their outcomes. To overcome these challenges, adopting an iterative approach that combines low-fidelity and high-fidelity models proves advantageous. Low-fidelity models, being less resource-intensive, enable rapid calibration and initial exploration of the parameter space, while high-fidelity models, whether experimental or numerical, provide a more detailed and accurate representation. This iterative refinement process, wherein insights from lower fidelity feed into higher fidelity, creates a robust framework that ensures the strengths of each approach are effectively leveraged, ultimately leading to a more comprehensive understanding of structural behaviour under complex loading conditions.

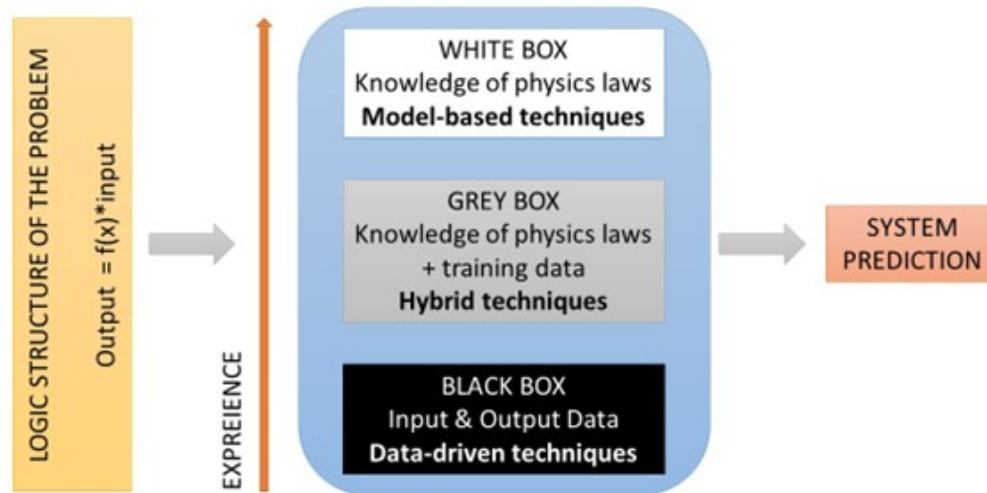


Figure 1.3: Close-up on shock prediction approaches

## 1.1 Model-Based Techniques for Shock Environment Prediction

Model-based techniques rely on physical equations and first-principles to simulate the behaviour of mechanical structures under dynamic loads. In this section, we will distinguish deterministic methods, where the outcome is fully determined by the initial conditions and inputs, from stochastic methods, in which randomness and uncertainty are involved.

### 1.1.1 From Deterministic to Statistical methods

For spacecraft, the mechanical environment during launch is typically measured in terms of acceleration (Gs) across a wide frequency range, from 10 Hz to 10,000 Hz. Predicting responses across this frequency spectrum is challenging, particularly due to the division between low and high frequencies. At low frequencies, where the first two modes usually lie, deterministic models such as the Finite Element Method (FEM) have been highly effective. FEM is widely accepted for its accuracy in predicting structural behaviour at frequencies where the first few natural modes dominate [15], [16]. For low-frequency ranges, where identical structures produce similar responses, FEM provides deterministic results. However, as frequency increases, the behaviour of the structure becomes less deterministic, particularly at

mid and high frequencies where modal density and overlap occur. In this regime, minor differences between otherwise identical structures can result in vastly different responses. Consequently, FEM becomes overly sensitive to minor details, and its accuracy diminishes as mesh sizes must decrease to capture the smallest characteristic deformations [17]. Moreover, for middle-high frequency FEM have the deficiencies of high computation costs. and statistical approach needs to be applied. [18, 19] show how FEM predictions are not comparable with test results at high frequencies. Compared to deterministic methods, energy-based methods are more efficient and statistical, among which Statistical Energy Analysis (SEA) is probably the most popular [20–22]. SEA is a powerful method used to predict the distribution of vibrational energy in complex mechanical systems, as they are described as a network of subsystems where the stored and exchanged energies are analysed [23]. The method is based on the assumption of statistical equilibrium, where the energy within each subsystem is evenly distributed among its modes, and the coupling between subsystems is relatively weak. This allows for the use of energy balance equations to describe the flow of vibrational energy between subsystems. SEA is particularly effective for systems with a large number of modes and high modal overlap, characteristics common in high-frequency regimes. In such cases, the precise behaviour of individual modes is less important than the overall statistical distribution of energy. The development of SEA began in the early 1960s, focusing on vibroacoustic challenges in aerospace engineering. "Statistical" refers to the fact that the variables are drawn from a statistical population, and the results are considered expected values. "Energy" indicates the use of energy-related variables, and as [24] explains, "Analysis" signifies that SEA represents a broad approach rather than a specific method. When dealing with mid frequency there is no universally accepted method as the structure does show neither a deterministic nor a chaotic behaviour. Accordingly, [25–27] proposed an improved methodology based on the Hybrid Finite Element-Statistical Energy Analysis (FE-SEA) method. Since SEA is able to deal with high frequency problems, combining FEM and SEA it is possible to cover the entire frequency range with rationality and sufficient accuracy of the prediction results. The hybrid method can predict the middle and high frequency shock response more effectively and reasonably, and the computational efficiency is greatly improved, compared with the traditional FEM. Dalton [28–35] proposed the Virtual Mode Synthesis Simulation (VMSS) method, where the dynamical system is numerically convoluted with a measurement or simulated excitation force to obtain the dynamic response in the time domain. This numerical method resulted to be suitable to solve the problem of transient and high frequency environment prediction. [36–39] successfully combined SEA in conjunction with VMSS for shock prediction during launch. In literature, there are many others alternative that requires a lower mesh density and fewer modes without

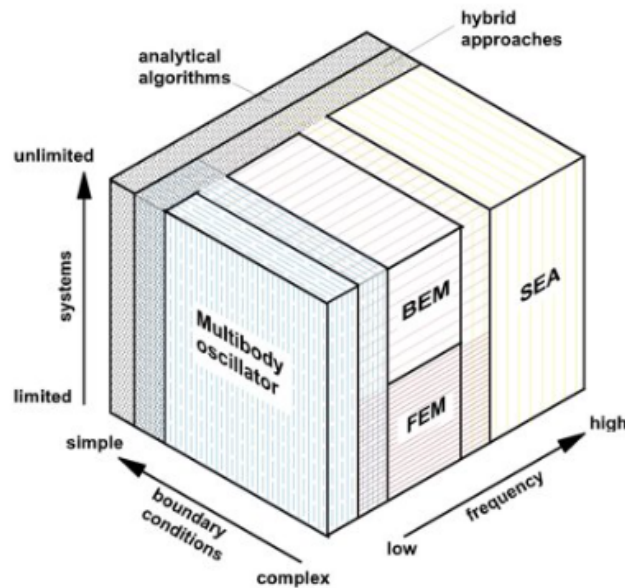


Figure 1.4: From deterministic to statistical

loss of accuracy for high-frequency vibration analysis, which makes it more computationally efficient than FEA. [40] combines the use of deterministic calculations with empirical analyses at high frequencies. The FEM provides the low-frequency content of the acceleration and a database of measured transmissibility magnitudes, coupled to a local random phase reconstruction concept, provides the high-frequency content. [41] showed a computational scaling method based on SEA as an alternative to the pyrotechnic shock scaling method used in industry [42]. [43] proposes transient energy finite element analysis (TEFEA). Energy Finite Element Analysis (EFEA) expands traditional FEM by incorporating energy transfer between subsystems, useful in damping-heavy systems [44]. [45] improved deterministic and energy-based methods. Moreover, the meshless method [46, 47], aims to make the model independent of the mesh, which reduces some computation and make it applicable to more complex structures. The dynamic stiffness method (DSM) [48] can always provide more accurate results independent of the number of elements.

### Finite Element Method (FEM) in Vibro-Acoustic Analysis of Composite Materials

For low-frequency scenarios, FEM is a widely recognised and efficient tool for modelling vibro-acoustic behaviour, particularly when system components are small compared to the wavelength of the frequency range. Atalla [49] demonstrated

FEM's efficacy in capturing physical behaviour in vibro-acoustic systems but highlighted challenges in applying it to innovative materials like composites and metamaterials, which possess orthotropic and frequency-dependent properties [50]. For high-frequency problems or complex geometries, hybrid techniques like combining FEM with SEA [?] have been proposed. In composite materials, FEM must account for orthotropic properties and layer-wise behaviours. Carrera's Unified Formulation (CUF) [51] provides advanced modelling capabilities for layer-wise methods, as implemented in tools like MUL2, enabling high-fidelity simulations. By contrast, FEM-based tools like Actran use an equivalent single-layer (ESL) approach, which, while computationally efficient, may yield inaccuracies in complex composites [?]. Hybrid LW/ESL models [?] and updated ESL formulations enhance both efficiency and accuracy. Further studies, such as those by Danu et al. [52], have explored how material microstructures, like fibre orientation and volume fraction, affect coupled responses. Works by Gorman et al. [?, ?, 53] and Yu et al. [?] have advanced understanding of modal shapes and natural frequencies in orthotropic plates. FEM's ability to predict composite materials' dynamic behaviour makes it critical for aerospace applications, particularly in launch scenarios. However, its limitations at higher frequencies necessitate hybrid methods, such as FE-SEA, to improve accuracy and computational efficiency. These advancements in FEM modelling align with the broader goal of reducing physical testing in spacecraft development while ensuring precise structural predictions.

### 1.1.2 Stochastic methods

Stochastic methodologies for mechanical shock prediction provide an alternative to deterministic models by accounting for inherent uncertainties in materials, geometry, and loading conditions. These methodologies extend classical models, such as FEM, by incorporating randomness into the analysis, making them essential for systems with unpredictable behaviour due to high variability in operating conditions. The simplest and most common of these approaches is the Full Monte Carlo simulation [54]. Although MCS approach is well known to bring accurate and robust predictions, its applicability is hindered by the high computational effort that is required [55]. Stochastic Finite Element Method (SFEM) extends the classical FEM by incorporating stochastic parameters, offering a robust framework for analysing systems under uncertainty. [56] provided a comprehensive foundation for SFEM, showing how randomness can be introduced into both mechanical and geometric properties. [57] presented a novel decomposition-based stochastic FEM specifically for spacecraft vibroacoustic simulation, which allows prediction of a nominal response and variations due to structural uncertainties as accurate as full Monte Carlo simulations but at a fraction of the computational effort. Polynomial Chaos Expansion (PCE) is an efficient tool for representing stochastic variables,

making it suitable for mechanical shock prediction under uncertainty [58, 59].

## 1.2 Data-Driven Techniques for Shock Environment Prediction

The substantial increase in computational power over recent decades has driven notable advancements in statistical and machine learning techniques. This development has produced a suite of algorithms and data mining methods that serve as the mathematical backbone of artificial intelligence (AI) systems. Although AI has a longstanding role in scientific discovery, contemporary data-driven methods in high-performance computing environments now enable large-scale algorithmic processing. These advancements are largely due to the sharply reduced costs of sensors, computational resources, and data storage technologies. As a result, the vast amounts of available data present new avenues for data-driven discovery, often described as the "4th paradigm" of science [60]. Unlike model-based approaches, data-driven methods does not require prior knowledge of the system's physical properties. Instead, they learn from input-output data and builds predictive models based on observed patterns. This characteristic makes data-driven techniques particularly attractive for predicting responses when the system's physical behaviour is complex or poorly understood. An example of this is demonstrated by system identification techniques, as discussed in [61]. Machine learning models, particularly the latest deep learning models, can extract features, namely quantifiable attributes or characteristics of the observed phenomenon, from various data types, including images, text, time series, and more. ML models of dynamic loads on mechanical structures have been carried out mainly for damage detection [62], structural health monitoring [63], and load identification [64]. For all these examples, ML requires no prior knowledge of the structure, and it is easy to be adapted for different applications. [65] used Data-Driven Surrogate Modelling in the field of computational dynamics to develop a fast and accurate predictive method for extreme close-in detonations of high explosive. [66] made use of Evolutionary Computation (EC) methods and ML techniques to predict the dynamic loads of several helicopters. The addition of EC to the traditional deterministic approach revealed to be successful in terms of accuracy and correlation. [67] developed a methodology that can determine the worst-case gust loads of a generic aircraft without excessive computation. It was shown that considerable savings in computational time can be made without sacrificing accuracy. Deep Machine Learning (DML) has been implemented to characterize material properties of dynamic shock-compression experiments [68], and fault prognostics [69]. [70] used a nonlinear autoregression (NAR) model to predict the timing and locations of random shocks. [71] presents

an alternative experimental data driven approach for virtual shaker testing. Artificial Neural Networks (ANNs) have become a dominant data-driven technique due to their flexibility in modelling nonlinear relationships in large datasets. This technology takes inspiration from a simplified biological neural network: an artificial neuron receives a signal then processes it through mathematical functions and send it to the connected neurons, which are typically aggregated in layers. The output of each layer is the weighted sum of the outputs from the previous one. During the learning or training process, the weighting factors are modified so that the calculated output match the actual output, trying to minimise the error. An ANN is thus a dynamic system. This feature would result in a highly robust system in which, changing the information stored in one element will have a little effect on the final output. [72] classified a range of different ANN systems according to four principal characteristics, each of them determining its suitability for solving certain classes of problems: the format and interpretation of data, the way neurons are connected, the operation functions, and the training scheme. The latter specify if the learning process is supervised or unsupervised, meaning that solution examples of the problem are present a priori or not. [73] proposed an ANN model for complex contacting bodies that, compared with the conventional model-based methods, is simple in principle and easy to implement. The method was capable of learning the underlying nonlinear mapping relations among data efficiently and accurately, with no extensive knowledge of the system physical behaviours being required. It demonstrates great advantages of ANN when the internal mechanisms are unknown or too complicated to be explored so far. Compared to conventional digital computing techniques, neural networks are advantageous because they can learn from example and generalize solutions to new renderings of a problem, can adapt to fine changes in a problem, are tolerant to errors in the input data, can process information rapidly, and are readily transportable between computing systems. [74] employed ANN to predict cyclic loading, displacement, stiffness, and strains of an advanced biological composite structure. [75] presented a method for solving both ordinary differential equations (ODE's) and partial differential equations (PDE's) that relies on the function approximation capabilities of feed-forward neural networks and results in the construction of a solution written in a differentiable, closed analytic form. The method could be extended for aerospace purposes, as for example eigenvalue problems for differential operators. [76] proposed an ANN model that approximately detects ice mass accumulated in different zones defined along the blade based on its natural frequencies. ANNs have been applied in various aerospace applications, such as damage detection based on the structural dynamic response [77, 78] and health monitoring [79]. Recently, some new approaches, such as deep learning neural network [80, 81], have also attracted widespread attention owing to their high efficiency and advantages in addressing



the uncertainties. Autoencoders, recurrent neural networks (RNNs), recursive long short-term memory (LSTM) network have also been employed for seismological applications [82–84]. Neural networks do, however, suffer from a few shortcomings, notably, a lack of precision, limited theory to assist in their design, no guarantee of success in finding an acceptable solution, and a limited ability to rationalise the solutions provided. The effectiveness of artificial neural networks (ANNs) is closely tied to both the quality and quantity of the training data they rely on. While data-driven methods have demonstrated significant potential and accuracy, challenges persist, particularly around securing high-quality, labelled datasets essential for training accurate predictive models. Furthermore, understanding how models can be interpreted and ensuring they generalize effectively across different contexts remain pressing research issues.

### 1.2.1 The Role of Digital Twins in Data-Driven Models

Up until recently, modelling the behaviour of a physical object was an expensive and time-consuming activity. It was necessary to physically create the object, or even a more sophisticated system, and the environment where it was impacted by actual forces. Often, the applied forces during the experimental phase would result in destruction of the system, dramatically increasing the expense. Moreover, during the actual use, many unforeseen conditions or emergent behaviours could overcome, resulting in failure of the system. Later, with CAD models, it was possible to extract more accurate information by three-dimensional static representations hanging in empty space, time independent. Nowadays simulations have become dynamic representations of the system's behaviour. We can strip the information from a physical object and create what we are calling a Digital Twin (DT), that can simulate physical forces on the system over time to determine its behaviour. The concept of the digital twin, a virtual replica of a physical system that is continuously updated with real-time data, has emerged as a significant advancement in data-driven models. Digital twins enable a more dynamic, data-driven approach to mechanical shock prediction by integrating sensor data, simulation models, and machine learning techniques. The digital twin framework typically consists of three main components: the physical system, the virtual twin (model), and the communication layer that enables real-time data exchange. The idea of the Digital Twin is to be able to design, test, manufacture, and use the virtual version of the systems, in order to understand whether our designs are manufacturable, and the modes of failure when the system is in use before the physical system is actually produced. This will reduce failures of the physical system when it is deployed and in use, reducing expenses, time, and harm to its users [85]. DT technology could potentially be implemented to simulate a mechanical environment that consider certain boundary conditions, and several variables that are update over time. The

Digital Twin (DT) concept was originally developed and applied within aerospace research and development. More recently, it has gained traction in the manufacturing sector. However, the literature indicates that DT adoption in manufacturing is still in its early stages. In this context, Cyber-Physical Systems (CPS) have expanded DT applications beyond traditional prognostics and diagnostics, establishing a foundational role for DT in production engineering. In manufacturing, the main objectives of simulation are to represent the complex behaviour of the system, also considering the possible consequences of external factors, human interactions and design constraints. [86] proposed simulation-based DT for complex behaviour of production in product life cycle. The proposed framework combining the real-life data with the simulation models from design to give predictions based on the realistic data. [87] proposed DT based simulation to optimize system behaviours during design phase in a smart CPS. In aerospace, simulations replicate the continuous time history of flights, generating extensive data to analyse an aircraft's experiences and predict future maintenance needs and interventions. These simulations employ various application-based techniques, including Computational Fluid Dynamics (CFD), Computer-Aided Engineering (CAE), Finite Element Methods (FEM), and Monte Carlo simulation [88–91], mostly for reducing unplanned downtime for engines and other systems [92]. The concept of Digital Twin (DT) is strictly linked to the aerospace field. It was conceived by National Aeronautics and Space Administration (NASA) and the US Air Force that needed to integrate a predictive tool for health maintenance and for the remaining useful life of their aerospace vehicles. They invented a way to replicate the flight model for mirroring on ground and in real time its condition during the mission [93]. In the literature, DT in aerospace is mostly used for Structural Health Monitoring (SHM) or Fatigue-damage prediction [94]. [95] pointed out that the application of DTs has reduced the time originally spent on aerospace material testing and verification by 80% and 25% respectively. Increasingly digitalisation in the aerospace industry is increasing the importance of two particular aspects of manufacturing and design: modularity and autonomy. DT can be used either for the whole life cycle and only for a step. The adoption of collaborative model-based engineering practices implies the use of aircraft digital models as the reference definition of the aircraft and the need to guarantee the data harmonisation and interoperability along the whole life cycle, from the aircraft beginning of life to the aircraft end of life.

While the use of digital twins for mechanical shock prediction has shown great potential, several challenges remain. Many digital twin models still rely on simplified assumptions, which can lead to errors in predicting shock effects on non-linear systems. Additionally, the integration of real-time data from multiple sources introduces challenges related to data fusion and uncertainty quantification in ac-



Figure 1.5: Life Cycle Assesment in Space ref: ESA

curately combining sensor data and simulation results, especially in the presence of noisy or incomplete data.

### 1.3 Hybrid Approaches: Combining Model-Based and Data-Driven Techniques

The current emphasis is put on data-centric techniques. The status of research is based on a collection of ad hoc methods, established on the earlier phases of AI-based models. We are facing the need of a more rigorous standard solution that can formalize purely data-driven models. In order to go beyond this limitation, we could combine the advantages of white and black box approach, namely grey box approach, that makes use of first-principles knowledge to put basis on more stochastic methods. The development of hybrid approaches could improve performances and overcome the limitations of individual physical and data-driven methods used separately. Pure physics-driven simulations are employed in cases where there is insufficient data for ML and the governing physical laws are well understood. On the other hand, typical data-driven approaches are for cases where data availability is high, and risks associated with failed predictions are low. Algorithmic advances need to be made to ensure that hybrid algorithms can leverage the best of both worlds i.e., retain the high predictive accuracy and computationally cheap nature of data-driven models, and at the same time incorporate elements of interpretability, encoding of physical laws and trustworthiness of simulation models [96]. [97] formulated a hybrid data-driven method for real-time prediction and uncertainty quantification (UQ) of fatigue failure under stochastic

loading. [98] developed and study an integrated analytical and computational data-driven grey box environment needed to describe transient phenomena in large-scale power system. [99] successfully trained a range of neural networks using random data and FE strains as inputs. [100] proposed a hybrid model that fuses physical modelling and data-driven techniques to predict fatigue crack growth. The hybrid approach demonstrated improved predictive performance over stand-alone models. [101] proposes a fusion of state-space modeling and artificial neural networks for the creation of predictive computational pyroshock models. In [102] hybrid state-space and data-based approach is developed for computational simulation of shock response prediction for both time histories and shock response spectra (SRS).

#### In a synthesis

- Historical development of shock analysis techniques, from early earthquake studies to modern aerospace applications.
- Importance of accurately predicting structural responses to dynamic loads across the entire frequency spectrum.
- Role of deterministic methods (like FEM) in low-frequency predictions and the transition to statistical methods for mid and high frequencies.
- Overview of hybrid approaches that integrate model-based and data-driven techniques, enhancing predictive accuracy and reliability.
- Emerging significance of AI and ML in developing more effective predictive models.
- Challenges faced by both experimental and numerical methods and the benefits of an iterative, multi-level modelling approach.

# Chapter 2

## Shock Phenomena: an Overview

### Contents

|       |   |    |
|-------|---|----|
| 2.1   | Introduction to Vibration Analysis and Shock Response . . . . .                   | 22 |
| 2.1.1 | Elastic continuum viewpoint - Wave Motion . . . . .                               | 23 |
| 2.1.2 | Macroscopic viewpoint - Modal Analysis Using Mass-Spring-Damper Models . . . . .  | 23 |
| 2.2   | Dynamics of Single-Degree-of-Freedom Systems . . . . .                            | 24 |
| 2.2.1 | Free Vibration of an Undamped System . . . . .                                    | 25 |
| 2.2.2 | Damped Free Vibration . . . . .   | 25 |
| 2.2.3 | Forced Vibration . . . . .  | 26 |
| 2.3   | Response of Single-Degree-of-Freedom Systems to Nonperiodic Excitations . . . . . | 27 |
| 2.3.1 | The Unit Pulse Function . . . . .   | 28 |
|       | Impulse Response of a Mass-Damper-Spring System . . . . .                         | 29 |
| 2.3.2 | The Unit Step Function . . . . .  | 31 |
| 2.3.3 | The Unit Ramp Function . . . . .  | 31 |
| 2.3.4 | Response to arbitrary excitations, the convolution integral . . . . .             | 32 |
| 2.4   | Modal Analysis on MDOF Systems . . . . .  | 34 |
| 2.4.1 | Free Vibration: Eigenvalue Problem . . . . .                                      | 34 |
| 2.4.2 | Modal Superposition Method . . . . .  | 36 |
| 2.5   | Frequency Response Function (FRF) . . . . .                                       | 37 |
| 2.6   | Transfer Function and Modal Decomposition . . . . .                               | 38 |
| 2.7   | Partial Fraction Expansion and FRF . . . . .                                      | 39 |
| 2.8   | Modal parameters . . . . .  | 40 |
| 2.8.1 | The residue . . . . .   | 40 |

|        |  |    |
|--------|--|----|
| 2.8.2  | Alternate Definition of the Residue . . . . .        | 40 |
| 2.8.3  | The modal participation factor . . . . .             | 41 |
| 2.8.4  | Modal Effective Mass . . . . .                       | 42 |
| 2.9    | Transitioning from Low to High Frequencies . . . . . | 42 |
| 2.9.1  | Local Mode Phase Reconstruction . . . . .            | 42 |
| 2.9.2  | Virtual Mode Synthesis . . . . .                     | 44 |
| 2.10   | Statistical Energy Analysis . . . . .                | 45 |
| 2.10.1 | Wave Propagation in Plates . . . . .                 | 45 |
| 2.10.2 | Fundamental Concepts of SEA . . . . .                | 48 |
|        | Reciprocity Relation . . . . .                       | 49 |
|        | SEA Equations for Multiple Subsystems . . . . .      | 49 |
|        | Coupling Loss Factors . . . . .                      | 50 |
|        | Modal Density . . . . .                              | 50 |
| 2.10.3 | Applying SEA to Complex Systems . . . . .            | 51 |
|        | Virtual SEA Analysis . . . . .                       | 52 |
|        | Virtual SEA (Commercial Software) . . . . .          | 54 |
|        | Virtual Power Injection Method . . . . .             | 54 |
|        | Subsystem Energy Computation . . . . .               | 54 |
|        | Analytic SEA . . . . .                               | 54 |
|        | Experimental SEA . . . . .                           | 55 |
|        | Power Injection Method . . . . .                     | 55 |

## 2.1 Introduction to Vibration Analysis and Shock Response

The study of mechanical vibration involves understanding the oscillatory behaviour of structures, which can be approached from both wave and mode perspectives. The fundamental characteristics that allow bodies to exhibit oscillatory behaviour are inertia and elasticity. Inertia enables momentum transfer between adjacent elements of the body and is related to mass density, while elasticity provides the restoring force that tends to return a body to its equilibrium position. Vibrations of a linear system can be categorized as free or forced, and this analysis can apply to both periodic and non-periodic excitations. In this work, we will focus on the behaviour of systems under non-periodic excitations such as pulses and transients.

### 2.1.1 Elastic continuum viewpoint - Wave Motion

Solids can store energy in shear and compression, hence several types of waves are possible, like compressional (longitudinal), flexural (transverse or bending), shear and torsional waves. Wave motion is a balance between potential and kinetic energies, with the potential energy being stored in different forms for different wave types. Compressional waves store potential energy in longitudinal strain, flexural waves in bending strain. It is convenient to represent the time-varying time motions as a summation of single frequency (harmonic) waves. There are two different types of velocity associated with wave motion: wave velocity, the velocity of the propagation of the disturbance through the medium (related to the characteristic of the medium and the external force), and particle velocity, the velocity of the oscillating mass particles in the medium (measure of the amplitude of the disturbance). For the compressional wave, there are alternate regions of expansion and compression of the mass particle, and particle and wave velocities are in the same direction. For flexural waves, the particle velocity is perpendicular to the direction of wave propagation. The wave motion can be represented as a function of time and space. Time variations in harmonic wave motion can be represented by the circular frequency  $\omega$ . This parameter represents the phase change per unit increase of time  $\omega = \frac{2\pi}{T}$ , where  $T$  is the temporal period of the wave motion. The phase of a wave is the time shift relative to its initial position. Space variations in wave motions are represented by the phase change per unit increase of distance. This parameter is the wave-number  $k$ , where  $k = \frac{\omega}{c}$ . With  $c$  being the wave velocity or phase velocity of the wave, because is the ratio of the phase change per unit increase of time to the phase change per unit increase of distance. The spatial period of a harmonic wave motion is described by its wavelength  $\lambda$ , such that  $k = \frac{2\pi}{\lambda}$ . If the wave velocity  $c$  of a time-varying motion is constant, then the relationship, between  $\omega$  and  $k$  is said to be non-dispersive, meaning that the spatial form of the wave does not change with time. On the other hand, if the spatial form is dependent of time the wave motion is dispersive. This is the case for groups of particle that most likely will form several waves propagating in different directions. The gradient of dispersion is called group velocity  $c_g = \frac{\delta\omega}{\delta k}$  and indicates the velocity of the overall envelope shape of the wave's amplitudes propagates through space.

### 2.1.2 Macroscopic viewpoint - Modal Analysis Using Mass-Spring-Damper Models

A macroscopic (modal) analysis requires a understanding of the concept of degrees of freedom (DOF), which represent the minimum number of independent coordinates required to describe the system's motion. For example, a single particle in

space has three degrees of freedom, a rigid body has six, and a continuous elastic body has an infinite number, one for each point in the body. A system with  $n$  degrees of freedom will have  $n$  natural frequencies and  $n$  modes of vibration. For certain structures, however, mechanical vibrations can be simplified by assuming rigid-body behaviour, reducing the infinite degrees of freedom to a finite number. In the context of modal analysis, the dynamics of a system can be approximated using lumped-parameter models, where the real structure is represented by a finite set of rigid masses, springs, and dampers. For continuous systems, the degrees of freedom are infinite, leading to a distributed-parameter model where the wave equation governs the response. The differential equation is the same but the mass, stiffness and damping are now continuous and a wave-type solution can be obtained. Modal analysis is more appropriate to study the first few natural frequencies of a system. The system is represented with multiple, discrete, mass-spring-damper oscillators and an excitation, that provides the force that is stored by the mass and the spring and dissipated by the damper. The mass is modelled as a rigid body that gains or loses kinetic energy. The spring stiffness  $k_s$  has negligible mass and possesses elasticity. The work done by the compression or expansion of the spring is converted into potential energy, because the strain energy is stored in the spring. The viscous damper will produce damping when there is a relative motion between its ends. The viscous damping  $c_v$  is proportional to velocity and is the most common model. The concepts of multiple, discrete, mass-spring-damper systems can be extended to analyse the vibrations of continuous systems at higher frequencies by re-modelling the structure in terms of continuous or distributed elements. The problem is usually first set up in terms of the wave equation and then generalised as an eigenvalue problem in terms of modal mass, stiffness and damping. The total response is the summation of the modal responses for the frequency range of interest.

## 2.2 Dynamics of Single-Degree-of-Freedom Systems

For a single-degree-of-freedom (SDOF) system, the motion is described by a single coordinate, and the system is typically modelled using a mass-spring-damper system. The governing equation of motion for an SDOF system subjected to external forces can be written as:

$$m\ddot{x}(t) + c\dot{x}(t) + kx(t) = F(t) \quad (2.1)$$

where:

- $m$  is the mass,
- $c$  is the damping coefficient,



- $k$  is the stiffness of the spring,
- $F(t)$  is the external forcing function,
- $x(t)$  is the displacement of the mass as a function of time.

### 2.2.1 Free Vibration of an Undamped System

First, consider the case where the system is undamped ( $c = 0$ ) and free of external forces ( $F(t) = 0$ ). The equation of motion becomes:

$$m\ddot{x}(t) + kx(t) = 0 \quad (2.2)$$

This is a second-order homogeneous differential equation. To solve it, assume a solution of the form:

$$x(t) = Ae^{i\omega_n t} \quad (2.3)$$

where  $\omega_n$  is the natural angular frequency of the system. Substituting this into the equation of motion gives the characteristic equation:

$$m(-\omega_n^2) + k = 0 \quad (2.4)$$

Solving for  $\omega_n$ , we obtain:

$$\omega_n = \sqrt{\frac{k}{m}} \quad (2.5)$$

The natural frequency in Hertz is given by:

$$f_n = \frac{\omega_n}{2\pi} = \frac{1}{2\pi} \sqrt{\frac{k}{m}} \quad (2.6)$$

Thus, the general solution for the displacement is:

$$x(t) = A \cos(\omega_n t) + B \sin(\omega_n t) \quad (2.7)$$

where  $A$  and  $B$  are constants determined by the initial conditions.

### 2.2.2 Damped Free Vibration

Now consider the case of a damped system ( $c \neq 0$ ) without external forcing ( $F(t) = 0$ ). The equation of motion becomes:

$$m\ddot{x}(t) + c\dot{x}(t) + kx(t) = 0 \quad (2.8)$$

To solve this, assume a solution of the form  $x(t) = e^{\lambda t}$ . Substituting this into 2.2 yields the characteristic equation:

$$m\lambda^2 + c\lambda + k = 0 \quad (2.9)$$

The solution to this quadratic equation is:

$$\lambda_{1,2} = \frac{-c \pm \sqrt{c^2 - 4mk}}{2m} \quad (2.10)$$

Define the damping ratio  $\zeta$  as:

$$\zeta = \frac{c}{2\sqrt{km}} \quad (2.11)$$

The roots of the characteristic equation are:

$$\lambda_{1,2} = -\zeta\omega_n \pm \omega_n\sqrt{\zeta^2 - 1} \quad (2.12)$$

There are three cases depending on the value of the damping ratio  $\zeta$ :

1. Underdamped System ( $\zeta < 1$ ): The solution is oscillatory with an exponentially decaying amplitude:

$$x(t) = e^{-\zeta\omega_n t} (A \cos(\omega_d t) + B \sin(\omega_d t)) \quad (2.13)$$

where  $\omega_d = \omega_n\sqrt{1 - \zeta^2}$  is the damped natural frequency.

2. Critically Damped System ( $\zeta = 1$ ): The system returns to equilibrium without oscillating:

$$x(t) = (A + Bt)e^{-\omega_n t} \quad (2.14)$$

3. Overdamped System ( $\zeta > 1$ ): The system does not oscillate and returns to equilibrium slowly:

$$x(t) = Ae^{\lambda_1 t} + Be^{\lambda_2 t} \quad (2.15)$$

where  $\lambda_1$  and  $\lambda_2$  are the real roots of the characteristic equation.

### 2.2.3 Forced Vibration

Now consider the case where the system is subjected to a periodic forcing function  $F(t) = F_0 \cos(\omega t)$ . The equation of motion is:

$$m\ddot{x}(t) + c\dot{x}(t) + kx(t) = F_0 \cos(\omega t) \quad (2.16)$$

The steady-state solution can be obtained using the method of undetermined coefficients. The steady-state response is given by:

$$x(t) = X_0 \cos(\omega t - \phi) \quad (2.17)$$

where the amplitude  $X_0$  and phase  $\phi$  are given by:

$$X_0 = \frac{F_0/m}{\sqrt{(\omega_n^2 - \omega^2)^2 + (2\zeta\omega_n\omega)^2}} \quad (2.18)$$

$$\phi = \tan^{-1} \left( \frac{2\zeta\omega_n\omega}{\omega_n^2 - \omega^2} \right) \quad (2.19)$$

The system exhibits resonance when the driving frequency  $\omega$  approaches the natural frequency  $\omega_n$ , resulting in a large amplitude response. The maximum amplitude occurs at:

$$\omega_{res} = \omega_n \sqrt{1 - 2\zeta^2} \quad (2.20)$$

In modal analysis of an SDOF system, we primarily focus on determining the natural frequencies and mode shapes (or oscillation patterns) of the system. For free vibration, these are dictated by the system's mass and stiffness. In damped systems, the damping ratio plays a critical role in shaping the response. For forced vibration, resonance and phase shift are key factors in understanding the system's dynamic behaviour. These principles are essential when analysing the response of systems to non-periodic excitations, such as shocks and transient forces, which will be explored in the following sections.

## 2.3 Response of Single-Degree-of-Freedom Systems to Nonperiodic Excitations

In practical applications, many mechanical systems are subjected to nonperiodic excitations, such as shock loads or transient pulses. The response of these systems can be analysed by solving linear differential equations derived from the system's equivalent lumped-parameter model. For single-degree-of-freedom (SDOF) systems, the response to nonperiodic excitations can be found using time-domain methods, such as the convolution integral. This chapter provides a theoretical overview of shock phenomena, focusing on time-domain techniques that are particularly effective for analysing systems subjected to deterministic, nonperiodic excitations. These excitations, often termed transient, differ from steady-state conditions in that they typically begin at  $t = 0$  and are not continuous. An example of this would be a force that is zero for  $t < 0$  and follows a sine wave for  $t \geq 0$ ; although harmonic for  $t \geq 0$ , such a force is still classified as transient. Using the superposition principle, the response of linear systems to nonperiodic

excitations can be combined with the response to initial conditions to compute the total system behaviour. Shock, as defined in this context, refers to a sudden, high-magnitude disturbance applied over a short duration. These disturbances often induce transient motion within mechanical systems, which can be effectively modelled using mathematical functions such as the unit pulse, unit step, and unit ramp. [5, 14] introduce these fundamental concepts, providing a framework for understanding how shocks influence system dynamics. The response of systems to shocks can be idealized through the use of impulse response functions, which are crucial for predicting the behaviour of a system under various input conditions. In particular, the unit pulse represents instantaneous forces, the unit step corresponds to forces that are applied suddenly and remain constant, and the unit ramp models forces that increase linearly over time. By analysing the system's response to these idealized inputs, it is possible to develop a comprehensive understanding of how shocks affect the dynamic behaviour of mechanical systems.

### 2.3.1 The Unit Pulse Function

The unit pulse, often represented by the Dirac delta function  $\delta(t)$ , is a mathematical abstraction used to model an impulse—a force of infinitesimal duration but finite magnitude. This function is frequently used to represent shock inputs in vibration analysis due to its simplicity and its role in linear systems theory. It is defined as:

$$\delta(t) = \begin{cases} 0 & \text{if } t \neq 0 \\ \infty & \text{if } t = 0 \end{cases} \quad (2.21)$$

and satisfies the following integral property:

$$\int_{-\infty}^{\infty} \delta(t) dt = 1 \quad (2.22)$$

Physically, the Dirac delta function represents an instantaneous impulse applied to the system at  $t = 0$ . The response of a linear time-invariant (LTI) system to such an impulse, denoted as the unit impulse response, enables the determination of the system's response to more complex inputs via convolution. The pulse function is ideal for modelling short-duration forces, such as impacts or collisions, which are frequently encountered in mechanical systems.

The response of a system to a unit pulse is denoted by  $h(t)$ , which characterizes the system's dynamic behaviour. For a linear time-invariant (LTI) system, the output response for any arbitrary input  $f(t)$  can be computed using the convolution integral:

$$y(t) = \int_{-\infty}^{\infty} h(\tau)f(t - \tau) d\tau \quad (2.23)$$

This response to an impulse is essential for shock analysis because it serves as the foundation for constructing the response to arbitrary time-varying inputs.

### Impulse Response of a Mass-Damper-Spring System

One of the most important concepts in vibrations is the impulse response, denoted by  $g(t)$  and defined as the response to  $\delta(t)$ , i.e., the response of a system to a unit impulse applied at  $t = 0$ , with the initial excitations being equal to zero. The importance of the impulse response derives from two facts. In the first place,  $g(t)$  embodies in a single function all the system characteristics. More important, however, is the fact that the impulse response can be used to synthesize the response of linear time-invariant systems to arbitrary excitations.

We have considerable interest in the impulse response of a mass-damper-spring system. The mass-damper-spring system can be modelled by the following second-order linear differential equation:

$$m\ddot{x}(t) + c\dot{x}(t) + kx(t) = f(t) \quad (2.24)$$

For the case of the impulse response, the external force is a Dirac delta function  $f(t) = \delta(t)$ , which models an instantaneous impulse at  $t = 0$ . Letting  $x(t) = g(t)$  and  $f(t) = \delta(t)$ , we can write the equation for the impulse response in the form

$$m\ddot{g}(t) + c\dot{g}(t) + kg(t) = \delta(t) \quad (2.25)$$

where  $m$  is the mass,  $c$  the coefficient of viscous damping and  $k$  the spring constant. The impulse response  $g(t)$  is subject by definition to the initial conditions

$$g(0) = 0, \quad \dot{g}(0) = 0 \quad (2.26)$$

so that, integrating the previous equation over the duration  $\epsilon$  of the impulse, we have

$$\int_0^{\epsilon} (m\ddot{g} + c\dot{g} + kg)dt = \int_0^{\epsilon} \delta(t)dt = 1 \quad (2.27)$$

Next, we take the limit of the integral on the left side of the equation as  $\epsilon$  approaches zero and evaluate the integral. To this end, we assume that  $g(t)$  is continuous and  $\dot{g}(t)$  is not. Now, consider Eq. 2.26 and write

$$\lim_{\epsilon \rightarrow 0} \int_0^{\epsilon} m\ddot{g}(t)dt = m\dot{g}(0^+) \quad (2.28)$$

$$\lim_{\epsilon \rightarrow 0} \int_0^\epsilon c \dot{g}(t) dt = 0 \quad (2.29)$$

$$\lim_{\epsilon \rightarrow 0} \int_0^\epsilon k g(t) dt = 0 \quad (2.30)$$

where  $\dot{g}(0^+)$  denotes the slope of the impulse response curve at the termination of the impulse, as opposed to  $\dot{g}(0) = 0$  at the initiation of the impulse, according to Eq. 2.26. Hence, inserting Eqs. 2.28, 2.29, and 2.30 into Eq. 2.27 and taking the limit as  $\epsilon \rightarrow 0$ , we obtain

$$m \dot{g}(0^+) = 1 \quad (2.31)$$

from which we conclude that the effect of a unit impulse at  $t = 0$  is to produce an equivalent initial velocity

$$\dot{g}(0^+) = \frac{1}{m} \quad (2.32)$$

which explains that impulsive forces produce initial velocities. At this point, instead of considering a non homogeneous system subjected to a unit impulse, we consider a homogeneous system subjected to an equivalent initial velocity as given by Eq. 2.31. We recall that we derived the response of a mass-damper-spring system to initial excitations

$$x(t) = C e^{-\zeta \omega_n t} \cos(\omega_d t - \phi) \quad (2.33)$$

where  $C$  and  $\phi$  represent the amplitude and phase angle of the response, respectively, having the values

$$C = \sqrt{x_0^2 + \left( \frac{\zeta \omega_n x_0 + v_0}{\omega_d} \right)^2}, \quad \phi = \tan^{-1} \left( \frac{\zeta \omega_n x_0 + v_0}{\omega_d x_0} \right) \quad (2.34)$$

Hence, inserting Eq. 2.31 into Eqs. 2.34, we have

$$C = \frac{1}{m \omega_d}, \quad \phi = \tan^{-1}(\infty) = \frac{\pi}{2} \quad (2.35)$$

so that, using Eq. 2.33 with  $x(t)$  replaced by  $g(t)$ , we obtain the impulse response of a mass-damper-spring system in the form

$$g(t) = \begin{cases} \frac{1}{m \omega_d} e^{-\zeta \omega_n t} \sin(\omega_d t) & \text{for } t > 0 \\ 0 & \text{for } t < 0 \end{cases} \quad (2.36)$$

where we recognized that the response must be zero before the impulse has occurred. The symbols appearing in Eq. 2.36 are defined as the viscous damping

factor  $\zeta = \frac{c}{2\sqrt{mk}}$ , the natural frequency  $\omega_n = \sqrt{\frac{k}{m}}$ , and the frequency of damped oscillation  $\omega_d = \omega_n \sqrt{1 - \zeta^2}$ . Equation 2.36 implies an underdamped system,  $\zeta < 1$ . A typical plot of the impulse response based on Eq. 2.36 is shown in Fig. 4.5.

### 2.3.2 The Unit Step Function

The unit step function  $u(t)$ , is defined as:

$$u(t) = \begin{cases} 0 & \text{if } t < 0 \\ 1 & \text{if } t \geq 0 \end{cases} \quad (2.37)$$

This function models a sudden force that switches on at  $t = 0$  and remains constant thereafter. The unit step function is particularly useful for analysing systems subjected to sudden load applications, such as the start of a machine or a sudden change in boundary conditions.

The unit step response of a system is the output when this type of input is applied. The relationship between the unit step and the unit pulse is crucial, as the unit step can be expressed as the integral of the unit pulse function:

$$u(t) = \int_{-\infty}^t \delta(\tau) d\tau \quad (2.38)$$

Thus, the response of a system to a step input can be obtained by integrating the impulse response:

$$y(t) = \int_0^t h(\tau) d\tau \quad (2.39)$$

Where  $h(\tau)$  is the impulse response of the system. This integration is crucial for shock analysis because it allows engineers to understand how a system evolves when subjected to a force that remains constant after its application. In real-world systems, this scenario is typical in applications involving steady forces, such as constant load bearings or sustained vibrations.

### 2.3.3 The Unit Ramp Function

The unit ramp function,  $r(t)$ , represents a continuously increasing force, defined as:

$$r(t) = \begin{cases} 0 & \text{if } t < 0 \\ t & \text{if } t \geq 0 \end{cases} \quad (2.40)$$

Ramp inputs are suitable for modelling gradually applied forces or increasing loads. For instance, the ramp function can simulate scenarios where a system is subjected to a progressively increasing stress or strain.

The unit ramp function can be interpreted as the integral of the unit step function:

$$r(t) = \int_0^t u(\tau) d\tau \quad (2.41)$$

Consequently, the response of a system to a ramp input is obtained by integrating the system's response to a step input:

$$y(t) = \int_0^t \int_0^\tau h(\sigma) d\sigma d\tau \quad (2.42)$$

This double integration demonstrates how the system reacts to a gradually increasing force, which can be critical in applications involving slow-loading processes, such as pressure build-up in hydraulic systems or structural deformation under increasing load.

### 2.3.4 Response to arbitrary excitations, the convolution integral

In this section, we focus on the response of LTI systems to arbitrary excitations. While responses to simple excitations like harmonic, impulse, step, and ramp functions can be described explicitly in terms of time, more complex excitations require a different approach to obtain their system response. The general method for handling complicated excitations is to express them as linear combinations of simpler excitations, for which the response is either readily available or can be computed with relative ease. Simple excitations, such as harmonic, impulse, step, and ramp functions, serve as fundamental building blocks, as their responses are well-known and can be used to model more complex systems. There are two primary methods for deriving the response to arbitrary excitations, based on how the excitation function is described. One method is to treat the arbitrary excitation as periodic, which allows for its representation as a Fourier series. By applying a limiting process, the period of the function is extended indefinitely, transforming the Fourier series into a Fourier integral, effectively converting a periodic function into an arbitrary one. This frequency-domain approach is typically more suitable for analysing random excitations. The second method, and the one emphasized here, is the time-domain approach. In this method, the arbitrary excitation is regarded as a superposition of impulses of varying magnitude, applied at different



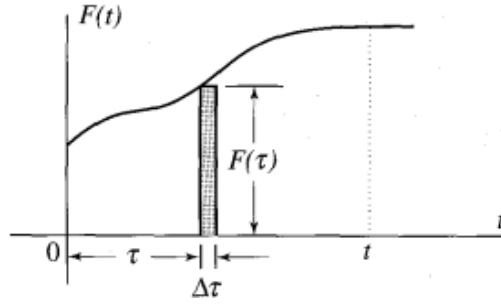


Figure 2.1: Arbitrary excitation

times. By representing the excitation as a sum of these impulse inputs, the system's response can be determined using known impulse response functions. This time-domain representation is particularly useful for deterministic excitations and provides a practical way to analyse the system's behaviour in response to complex, time-varying inputs. We consider an arbitrary excitation  $F(\tau)$  like in 2.1 and focus our attention on the contribution to the response of an impulse corresponding to the time interval  $\tau < t < \tau + \Delta\tau$ . Assuming that the time increment  $\Delta\tau$  is sufficiently small. Assuming that  $F(\tau)$  remains approximately constant over the small time interval, the shaded region can be treated as an impulse applied during  $\tau < t < \tau + \Delta\tau$ , with a magnitude of  $F(\tau)\Delta\tau$ . The excitation corresponding to this shaded area can be considered as an impulsive force represented as:

$$\hat{F}(\tau)\delta(t - \tau) = F(\tau)\Delta\tau\delta(t - \tau) \quad (2.43)$$

The response of a linear time-invariant system to this impulsive force is:

$$\Delta x(t, \tau) = F(\tau)\Delta\tau g(t - \tau) \quad (2.44)$$

where  $g(t - \tau)$  represents the system's impulse response, delayed by the time interval  $\tau$ . By considering the excitation  $F(t)$  as a series of these small impulsive forces, we can approximate the system's total response as:

$$x(t) = \sum_{\tau} F(\tau)\Delta\tau g(t - \tau) \quad (2.45)$$

In the limit, as  $\Delta\tau \rightarrow 0$ , the summation can be replaced by an integral to yield the exact response:

$$x(t) = \int_{-\infty}^t F(\tau)g(t - \tau)d\tau \quad (2.46)$$

This equation, known as the convolution integral, expresses the system's response as a superposition of impulse responses. For this reason, Eq. 2.46 is also

referred to as the superposition integral. In many cases, the excitation function is so complex that solving the convolution integral analytically becomes extremely challenging. For example, in the case of pyroshock, a high-frequency transient vibration generated by explosive events, the excitation signal is irregular and often difficult to describe with standard mathematical functions. Furthermore, there are situations where the excitation cannot be expressed analytically at all, but is instead provided as a graph or a set of discrete data points. In such instances, numerical methods must be employed to evaluate the convolution integral, as closed-form solutions are not feasible.

## 2.4 Modal Analysis on MDOF Systems

In real-world structures, the response to dynamic loading is often more complex than can be represented by a Single-Degree-of-Freedom (SDOF) system. For more complex structures, the response must be modelled using Multiple-Degree-of-Freedom (MDOF) systems, which can capture the influence of multiple modes of vibration. Modal analysis transforms the system dynamics from physical coordinates into modal coordinates in such a way that each mode of the system behaves as if it were a single degree of freedom. The SRS can then be applied to the system in the modal domain based on the mode frequency and the degree of participation that each mode has to the overall system response. The individual modal responses are then transformed back into physical coordinates using the modal transformation. The modal transformation between physical and modal coordinates is accomplished by an eigenvalue extraction of the matrix equations of motion. The resulting eigenvalues and eigenvectors are the frequencies and mode shapes for each mode of vibration of the system, respectively. The mode shapes, or eigenvectors, are used to transform the system from physical coordinates to modal coordinates and vice versa. The mathematics to accomplish this transformation are summarized below. In structural dynamics and vibration analysis, modal analysis is used to study the natural frequencies and mode shapes of a system. The frequency response function (FRF) is an essential tool that describes how a system responds to external dynamic forces in the frequency domain. This document presents the derivation of the FRF for a multi-degree-of-freedom (MDOF) system using modal analysis. The approach is based on the works of [6, 7], which cover both analytical and experimental modal analysis.

### 2.4.1 Free Vibration: Eigenvalue Problem

We begin with the general equation of motion for a linear MDOF system:

$$\mathbf{M}\ddot{\mathbf{x}}(t) + \mathbf{K}\mathbf{x}(t) = \mathbf{F}(t) \quad (2.47)$$

where:

- $\mathbf{M}$  is the mass matrix ( $n \times n$ ), representing the system's mass distribution.
- $\mathbf{K}$  is the stiffness matrix ( $n \times n$ ), representing the stiffness characteristics of the system.
- $\mathbf{x}(t)$  is the displacement vector ( $n \times 1$ ), representing the displacements of each degree of freedom.
- $\mathbf{F}(t)$  is the external force vector ( $n \times 1$ ), containing the forces applied to the system at different points.
- $n$  is the number of degrees of freedom (DOF) in the system.

For systems with proportional damping, the damping matrix  $\mathbf{C}$  is a linear combination of the mass and stiffness matrices:

$$\mathbf{C} = \alpha\mathbf{M} + \beta\mathbf{K} \quad (2.48)$$

where  $\alpha$  and  $\beta$  are constants representing mass-proportional and stiffness-proportional damping, respectively.

For the free vibration case, where no external forces are applied, i.e.,  $\mathbf{F}(t) = 0$ , the system's motion is governed by:

$$\mathbf{M}\ddot{\mathbf{x}}(t) + \mathbf{K}\mathbf{x}(t) = 0 \quad (2.49)$$

We assume a harmonic solution of the form:

$$\mathbf{x}(t) = \hat{\mathbf{x}}e^{st} \quad (2.50)$$

Substituting this assumed solution into the free vibration equation gives:

$$(\mathbf{K} - s^2\mathbf{M})\hat{\mathbf{x}} = 0 \quad (2.51)$$

This is a generalized eigenvalue problem. The goal is to solve for  $s^2 = \lambda$ , where  $\lambda$  represents the *eigenvalues* of the system, and  $\hat{\mathbf{x}}$  are the corresponding eigenvectors or mode shapes. Thus, we can write:

$$(\mathbf{K} - \lambda\mathbf{M})\hat{\mathbf{x}} = 0 \quad (2.52)$$

The eigenvectors (mode shapes) are orthogonal with respect to both the mass and stiffness matrices:

$$\hat{\mathbf{x}}_i^T \mathbf{M} \hat{\mathbf{x}}_j = M_i \delta_{ij}, \quad \hat{\mathbf{x}}_i^T \mathbf{K} \hat{\mathbf{x}}_j = K_i \delta_{ij} \quad (2.53)$$

This orthogonality property is crucial for decoupling the system of equations in the modal domain, allowing us to treat each mode separately.

## 2.4.2 Modal Superposition Method

The total displacement  $\mathbf{x}(t)$  of a MDOF system can be represented as a linear combination of its mode shapes (eigenvectors). This is the basis of the modal superposition method, where the system's response is expressed in terms of the contributions of its individual modes. The total displacement is written as:

$$\mathbf{x}(t) = \mathbf{\Phi} \mathbf{q}(t) \quad (2.54)$$

Substituting this into Eq. 2.47:

$$\mathbf{M} \mathbf{\Phi} \ddot{\mathbf{q}}(t) + \mathbf{K} \mathbf{\Phi} \mathbf{q}(t) = \mathbf{F}(t) \quad (2.55)$$

To simplify this, we pre-multiply both sides by  $\mathbf{\Phi}^T$ . Using the orthogonality properties of the eigenvectors with respect to the mass and stiffness matrices:

$$\mathbf{\Phi}^T \mathbf{M} \mathbf{\Phi} = \mathbf{M}^*, \quad \mathbf{\Phi}^T \mathbf{K} \mathbf{\Phi} = \mathbf{K}^* \quad (2.56)$$

we decouple the system of equations into  $n$  independent scalar equations:

$$M_i \ddot{q}_i(t) + K_i q_i(t) = f_i(t), \quad i = 1, 2, \dots, n \quad (2.57)$$

Each of the  $n$  modes can now be treated independently, as they are decoupled. The total displacement response of the system is obtained by summing the contributions from each mode. The displacement in the physical coordinates is given by the modal superposition:

$$\mathbf{x}(t) = \sum_{i=1}^n \hat{\mathbf{x}}_i q_i(t) \quad (2.58)$$

where  $\hat{\mathbf{x}}_i$  is the mode shape of the  $i$ -th mode, and  $q_i(t)$  is the generalized coordinate (modal coordinate) corresponding to the  $i$ -th mode.

Each of the  $n$  modes can now be treated independently, as they are decoupled. The total displacement response of the system is obtained by summing the contributions from each mode. The displacement in the physical coordinates is given by the modal superposition:

$$\mathbf{x}(t) = \sum_{i=1}^n \hat{\mathbf{x}}_i q_i(t) \quad (2.59)$$

where  $\hat{\mathbf{x}}_i$  is the mode shape of the  $i$ -th mode, and  $q_i(t)$  is the generalized coordinate (modal coordinate) corresponding to the  $i$ -th mode.

For each mode, the response can be calculated independently, using methods developed for single-degree-of-freedom (SDOF) systems. The response for non-periodic excitations, for example, can be determined using the convolution integral or the shock response spectrum (SRS) in the modal domain. Once the modal responses  $q_i(t)$  are computed for each mode, the total response is transformed back into physical coordinates using the modal transformation of Eq. 2.59:

$$\mathbf{x}(t) = \Phi \mathbf{q}(t) \quad (2.60)$$

## 2.5 Frequency Response Function (FRF)

The modal superposition method allows us to decompose the response of a multi-degree-of-freedom (MDOF) system into contributions from each mode in the time domain. This approach is particularly useful for understanding how individual modes evolve over time when the system is subjected to dynamic loading. However, many problems in structural dynamics and vibration analysis are more conveniently addressed in the frequency domain, especially when the system is excited by harmonic forces. In this context, the Frequency Response Function (FRF) provides a direct relationship between the input force and the output displacement as a function of frequency. To derive the FRF, we transform the equations of motion into the frequency domain using the Fourier transform or Laplace transform, where  $s = i\omega$  represents the frequency variable in the Laplace domain. The equation for each mode in the frequency domain is:

$$-M_i \omega^2 \hat{q}_i(\omega) + K_i \hat{q}_i(\omega) = \hat{f}_i(\omega) \quad (2.61)$$

where:

- $M_i$  is the modal mass of the  $i$ -th mode,
- $K_i$  is the modal stiffness of the  $i$ -th mode,
- $\hat{q}_i(\omega)$  is the frequency-domain modal coordinate for the  $i$ -th mode,
- $\hat{f}_i(\omega)$  is the generalized force in the frequency domain.

Solving for  $\hat{q}_i(\omega)$  gives the modal response in the frequency domain:

$$\hat{q}_i(\omega) = \frac{\hat{f}_i(\omega)}{K_i - M_i \omega^2} \quad (2.62)$$

The total system response  $\hat{\mathbf{x}}(\omega)$  in the frequency domain can be written as:

$$\hat{\mathbf{x}}(\omega) = \Phi \hat{\mathbf{q}}(\omega) = \Phi \left( \frac{\hat{\mathbf{f}}(\omega)}{\mathbf{K}^* - \mathbf{M}^* \omega^2} \right) \quad (2.63)$$

where:

- $\mathbf{K}^*$  and  $\mathbf{M}^*$  are the diagonal matrices of modal stiffnesses and modal masses, respectively,
- $\Phi$  is the modal matrix (with each column being a mode shape).

## 2.6 Transfer Function and Modal Decomposition

The transfer function,  $\mathbf{H}(\omega)$ , describes the relationship between the input force  $\hat{\mathbf{F}}(\omega)$  applied to a system and the resulting output displacement  $\hat{\mathbf{x}}(\omega)$  as a function of frequency. This function is essential for analysing the dynamic response of systems in the frequency domain. In the context of modal analysis, the transfer function can be written as a sum of contributions from each mode of vibration. For an  $n$ -degree-of-freedom system, the displacement response in the frequency domain is related to the transfer function by:

$$\hat{\mathbf{x}}(\omega) = \mathbf{H}(\omega) \hat{\mathbf{F}}(\omega) \quad (2.64)$$

Each mode  $r$  contributes to the system's response, and the transfer function for mode  $r$  is given by:

$$\mathbf{H}_r(\omega) = \frac{\hat{\mathbf{x}}_r \hat{\mathbf{x}}_r^T}{K_r - M_r \omega^2} \quad (2.65)$$

where:

- $\hat{\mathbf{x}}_r$  is the eigenvector (mode shape) corresponding to the  $r$ -th mode,
- $M_r$  is the modal mass of mode  $r$ ,
- $K_r$  is the modal stiffness of mode  $r$ ,
- $\omega$  is the excitation frequency.

The total transfer function,  $\mathbf{H}(\omega)$ , for the MDOF system is the sum of the modal contributions:

$$\mathbf{H}(\omega) = \sum_{r=1}^n \frac{\hat{\mathbf{x}}_r \hat{\mathbf{x}}_r^T}{K_r - M_r \omega^2} \quad (2.66)$$

This shows that each mode  $r$  contributes to the system's response depending on its mode shape, stiffness, and mass.

## 2.7 Partial Fraction Expansion and FRF

To analyse the system's response in the presence of damping, we introduce a damping ratio  $\zeta_r$  for each mode. Damping causes the poles of the system to shift from the imaginary axis into the complex plane. The dynamic stiffness for a lightly damped system becomes:

$$D_r(\omega) = K_r - M_r\omega^2 + i2\zeta_r\omega_r M_r\omega \quad (2.67)$$

where:

- $\zeta_r$  is the damping ratio for mode  $r$ ,
- $\omega_r$  is the natural frequency of mode  $r$ ,
- $i$  is the imaginary unit, indicating that damping introduces a complex component to the dynamic stiffness.

The transfer function now becomes a complex function of frequency due to the presence of damping. Using partial fraction expansion, the system's transfer function can be expressed in terms of its poles  $\lambda_r$ , which are the complex-valued solutions to the characteristic equation:

$$\lambda_r = -\zeta_r\omega_r \pm i\omega_r\sqrt{1 - \zeta_r^2} \quad (2.68)$$

These poles represent the system's natural frequencies modified by the damping. The transfer function in terms of the poles is:

$$\mathbf{H}(\omega) = \sum_{r=1}^n \left( \frac{\mathbf{A}_r}{i\omega - \lambda_r} + \frac{\mathbf{A}_r^*}{i\omega - \lambda_r^*} \right) \quad (2.69)$$

where:

- $\mathbf{A}_r = \frac{\hat{\mathbf{x}}_r \hat{\mathbf{x}}_r^T}{2\lambda_r M_r}$  is the modal residue for mode  $r$ ,
- $\lambda_r^*$  is the complex conjugate of  $\lambda_r$ ,
- $\mathbf{A}_r^*$  is the complex conjugate of the modal residue  $\mathbf{A}_r$ .

The poles  $\lambda_r$  represent the frequencies at which the system resonates, and the residues  $\mathbf{A}_r$  encapsulate the contribution of each mode to the overall response. The system's total response is the sum of the contributions from all modes, and each mode's behaviour is governed by its natural frequency, damping ratio, and mode shape.

## 2.8 Modal parameters

### 2.8.1 The residue

The residue, denoted as  $\mathbf{A}_r$ , is a fundamental parameter in the frequency response function (FRF) and plays an essential role in defining the contribution of each mode to the system's response. Mathematically, the residue for mode  $r$  is given by:

$$\mathbf{A}_r = \frac{\hat{\mathbf{x}}_r \hat{\mathbf{x}}_r^T}{2\lambda_r M_r} \quad (2.70)$$

where:

- $\hat{\mathbf{x}}_r$  is the eigenvector (mode shape) corresponding to mode  $r$ ,
- $\lambda_r = -\zeta_r \omega_r \pm i\omega_r \sqrt{1 - \zeta_r^2}$  are the system's complex poles for each mode, with  $\zeta_r$  being the damping ratio and  $\omega_r$  the natural frequency for mode  $r$ ,
- $M_r$  is the modal mass associated with mode  $r$ .

The residue  $\mathbf{A}_r$  determines how strongly each mode contributes to the overall system response in the frequency domain. In particular, residues describe the amplitude and phase of the system's response at frequencies near the system's poles. Large residues indicate modes that have significant influence on the dynamic behaviour, especially in systems with lightly damped modes where the response peaks sharply near the natural frequencies. In the context of FRF synthesis, the residue also provides insights into how the system's response can be reconstructed from its modal properties. Modal synthesis involves generating the FRF from the system's natural frequencies, mode shapes, and damping ratios. The residues, as a part of this synthesis process, link the modal parameters to the system's physical response in both analytical and experimental settings. When using finite element (FE) models or experimental data to generate FRFs, residues can be calculated directly from modal analysis, as explained by [9] in their work on modal scaling and FRF synthesis.

### 2.8.2 Alternate Definition of the Residue

Another way to define the residue,  $\mathbf{A}_{pq_r}$ , is in terms of the components of the eigenvectors at specific coordinates  $p$  and  $q$ . The residue can be expressed as:

$$\mathbf{A}_{pq_r} = Q_r \hat{x}_{p_r} \hat{x}_{q_r} \quad (2.71)$$

where:



- $Q_r$  is a scaling constant for mode  $r$ ,
- $\hat{x}_{p_r}$  and  $\hat{x}_{q_r}$  are the components of the mode shape  $\hat{\mathbf{x}}_r$  at coordinates  $p$  and  $q$ , respectively.

The scaling constant  $Q_r$  is typically related to the modal mass and natural frequency. When the modal mass is normalized to unity,  $Q_r$  can be expressed as:

$$Q_r = \frac{1}{j2\omega_r M_r} \quad (2.72)$$

where:

- $\omega_r$  is the damped natural frequency for mode  $r$ ,
- $M_r$  is the modal mass,
- $j$  is the imaginary unit.

This scaling ensures consistency when modal masses are normalized, simplifying the interpretation of the residues in terms of the system's physical properties. This alternative definition is especially useful when the modal components  $\hat{x}_{p_r}$  and  $\hat{x}_{q_r}$  are obtained directly from FE Modal Analysis or experimental modal testing. The scaling constant  $Q_r$  is often retrieved from modal analysis using techniques, particularly when the modal mass is set to unity.

### 2.8.3 The modal participation factor

The modal participation factor (MPF) is a measure of how much a specific mode contributes to the response of the system under a given loading condition. It quantifies the extent to which the external force excites a particular mode. The participation factor for mode  $r$  is defined as:

$$\Gamma_r = \frac{\hat{\mathbf{x}}_r^T \mathbf{M} \mathbf{v}}{M_r} \quad (2.73)$$

where:

- $\hat{\mathbf{x}}_r$  is the eigenvector corresponding to mode  $r$ ,
- $\mathbf{M}$  is the mass matrix of the system,
- $\mathbf{v}$  is the load vector, typically representing the direction or point of application of external forces,
- $M_r$  is the modal mass for mode  $r$ .

The participation factor describes how effectively the external force aligns with the mode shape  $\hat{\mathbf{x}}_r$ . A larger value of  $\Gamma_r$  means that mode  $r$  will contribute more significantly to the system's overall response. Conversely, if the participation factor is small, the mode is less likely to be excited by the applied loading. For systems with multiple modes, the total dynamic response is often dominated by a few modes with high participation factors. Thus, the MPF is critical in modal reduction techniques, where only the modes with significant participation factors are retained in the analysis.

### 2.8.4 Modal Effective Mass

Another important concept is the modal effective mass (MEM), which quantifies the contribution of each mode to the system's total mass in the dynamic response. It is defined as:

$$\text{MEM}_r = (\hat{\mathbf{x}}_r^T \mathbf{M} \mathbf{v})^2 \quad (2.74)$$

The modal effective mass is related to the participation factor and provides a way to estimate the influence of each mode on the overall motion of the system. Modes with high effective mass are critical in determining the system's dynamic response. The modal effective mass fraction (MEMF) is the ratio of the modal effective mass to the total mass of the system:

$$\text{MEMF}_r = \frac{\text{MEM}_r}{M_{\text{total}}} \quad (2.75)$$

where  $M_{\text{total}}$  is the total mass of the system. The MEMF is useful for identifying the modes that contribute most to the dynamic behaviour.

## 2.9 Transitioning from Low to High Frequencies

Analysing the dynamic behaviour of structures across a wide frequency range poses significant challenges. In the low-frequency domain, traditional modal analysis methods suffice to extract modal parameters accurately. However, as we transition to higher frequencies, modal densities increase, and modes become more closely spaced, making it difficult to identify and characterize individual modes using conventional techniques. To address this, alternative methods such as local mode phase reconstruction and virtual mode synthesis are employed [8, 13].

### 2.9.1 Local Mode Phase Reconstruction

The transition between low and high-frequency domains is often determined by transmissibility, which indicates how acceleration levels are transmitted from a

source of excitation to any other point on the structure. This transmission occurs due to global modal behaviours. Local Mode Phase Reconstruction (LMPR) is an approach used to accurately capture the modal parameters in the high-frequency range by focusing on local dynamics. To understand this, let's first review the equations of motion for a structure consisting of two subsystems: the interface subsystem (junction) and the unit subsystem (internal). Neglecting damping, the equation of motion for the system can be written as:

$$\begin{bmatrix} M_{jj} & M_{ji} \\ M_{ij} & M_{ii} \end{bmatrix} \begin{bmatrix} \ddot{u}_j \\ \ddot{u}_i \end{bmatrix} + \begin{bmatrix} K_{jj} & K_{ji} \\ K_{ij} & K_{ii} \end{bmatrix} \begin{bmatrix} u_j \\ u_i \end{bmatrix} = \begin{bmatrix} R_j \\ 0 \end{bmatrix} \quad (2.76)$$

where:

- $M$  and  $K$  are the mass and stiffness matrices, respectively,
- $u_j$  represents the displacements at the junction (interface),
- $u_i$  represents the internal displacements (unit subsystem),
- $R_j$  are the force reactions at the junction.

The dynamic transmissibility matrix  $\tilde{T}_{ij}(\omega)$  links the interface displacements  $u_j$  to the internal displacements  $u_i$ , and is defined as:

$$u_i = \tilde{T}_{ij}(\omega)u_j \quad (2.77)$$

The dynamic transmissibility matrix  $\tilde{T}_{ij}(\omega)$  can be expanded as a summation of the contributions from individual modes:

$$\tilde{T}_{ij}(\omega) = \sum_{k=1}^m T_k(\omega) \tilde{T}_{ij,k} \quad (2.78)$$

where:

- $T_k(\omega)$  is the dynamic transmissibility factor for mode  $k$ ,
- $\tilde{T}_{ij,k}$  is the effective transmissibility matrix for mode  $k$ .

The effective transmissibility matrix  $\tilde{T}_{ij,k}$  is given by:

$$\tilde{T}_{ij,k} = \frac{\Phi_{ik} L_{kj}}{m_k} \quad (2.79)$$

where:

- $\Phi_{ik}$  is the matrix of eigenmodes for the internal displacements  $u_i$ ,

- $m_k$  is the generalized mass for mode  $k$ ,
- $L_{kj}$  is the participation factor for mode  $k$ .

The participation factor  $L_{kj}$  is defined as:

$$L_{kj} = \Phi_{ik} (M_{ii} S_{ij} + M_{ij}) \quad (2.80)$$

where  $S_{ij}$  is the junction static mode matrix, defined as:

$$S_{ij} = -K_{ii} K_{ij}^{-1} \quad (2.81)$$

The static mode matrix  $S_{ij}$  represents the contribution of static modes at the junction. The summation of the effective modal transmissibility matrices across all modes converges to the junction static mode matrix:

$$\sum_{k=1}^{+\infty} \tilde{T}_{ij}(\omega) = \sum_{k=1}^{+\infty} \frac{\Phi_{ik} L_{kj}}{m_k} = S_{ij} \quad (2.82)$$

This shows that the dynamic transmissibility matrix accounts for the contribution of each mode to the overall response of the system. The combination of the transmissibility factor  $T_k(\omega)$  and the mode-specific term  $\frac{\Phi_{ik} L_{kj}}{m_k}$  characterizes the contribution of each mode to the unit system response.

## 2.9.2 Virtual Mode Synthesis

In cases where LMPR is insufficient, an alternative method known as Virtual Mode Synthesis (VMSS) can be used to estimate the modal parameters in the high-frequency domain. VMSS involves generating "virtual modes" that approximate the behaviour of the system in frequency ranges where the physical modes are difficult to extract.

Consider the generalized equation of motion:

$$M\ddot{q}(t) + C\dot{q}(t) + Kq(t) = F(t) \quad (2.83)$$

where:

- $M$ ,  $C$ , and  $K$  are the mass, damping, and stiffness matrices,
- $q(t)$  are the generalized coordinates,
- $F(t)$  is the external force.

VMSS approximates the response by using fictitious or "virtual" modes to capture the aggregate effect of the high-frequency modes. These virtual modes are synthesised by approximating the modal parameters over a selected frequency range. The virtual mode response can be written as:

$$q(t) \approx \sum_{k=1}^{n_v} q_{v_k}(t) \quad (2.84)$$

where  $q_{v_k}(t)$  are the responses due to the virtual modes and  $n_v$  is the number of virtual modes required to capture the response in the high-frequency range. The parameters for the virtual modes are chosen such that the overall response of the system matches the measured or expected response in the high-frequency domain. This method allows for accurate approximation of the system behaviour without needing to explicitly calculate each high-frequency mode.

## 2.10 Statistical Energy Analysis

Statistical Energy Analysis (SEA) is a powerful method used to predict the distribution of vibrational energy in complex mechanical systems, especially at high frequencies where traditional deterministic methods like the Finite Element Method (FEM) become computationally intensive or impractical. Originally developed in 1960 for acoustics problems, SEA has been extended to various fields, including vibration and shock analysis. SEA models a complex system as an assembly of subsystems, each representing a portion of the total structure. The method is based on the assumption of statistical equilibrium, where the energy within each subsystem is evenly distributed among its modes, and the coupling between subsystems is relatively weak. This allows for the use of energy balance equations to describe the flow of vibrational energy between subsystems. SEA is particularly effective for systems with a large number of modes and high modal overlap, characteristics common in high-frequency regimes. In such cases, the precise behaviour of individual modes is less important than the overall statistical distribution of energy. In this section, we will discuss the fundamental concepts of SEA, derive the basic energy balance equations, and explain how to apply SEA to complex systems. We will also explore wave propagation in plates, as understanding wave behaviour is essential for determining coupling between subsystems.

### 2.10.1 Wave Propagation in Plates

Understanding wave propagation in subsystems is essential for calculating coupling loss factors. In the case of plates, which are common structural elements, different

types of waves can propagate, including in-plane (longitudinal and shear) waves and bending waves. We consider thin, flat plates, which can be described by classical plate theory under the following assumptions:

1. The thickness  $h$  of the plate is much smaller than the other dimensions (length and width).
2. The in-plane strains are small compared to unity.
3. Transverse shear strains  $\epsilon_{xz}$  and  $\epsilon_{yz}$  are negligible (Kirchhoff-Love plate theory).
4. Tangential displacements  $u$  and  $v$  are linear functions of the thickness coordinate  $z$ .
5. The transverse shear stresses vanish at the surfaces  $z = \pm h/2$ , so  $\sigma_{zz} = \sigma_{zy} = \sigma_{xz} = 0$  at these surfaces.

The in-plane motion of a plate involves displacements  $u(x, y, t)$  and  $v(x, y, t)$  in the  $x$  and  $y$  directions, respectively. The governing equations for in-plane waves can be derived from the equations of motion and constitutive relations. For isotropic plates, the equations of motion in the absence of external body forces are:

$$\begin{aligned} C \frac{\partial^2 u}{\partial x^2} + S \frac{\partial^2 u}{\partial y^2} + S \frac{1 + \nu}{1 - \nu} \frac{\partial^2 v}{\partial x \partial y} - \rho h \frac{\partial^2 u}{\partial t^2} &= F''_{x,\text{ext}}, \\ C \frac{\partial^2 v}{\partial y^2} + S \frac{\partial^2 v}{\partial x^2} + S \frac{1 + \nu}{1 - \nu} \frac{\partial^2 u}{\partial x \partial y} - \rho h \frac{\partial^2 v}{\partial t^2} &= F''_{y,\text{ext}}, \end{aligned} \quad (2.85)$$

where:

- $C = \frac{Eh}{1 - \nu^2}$  is the extensional stiffness.
- $S = \frac{Eh\nu}{1 - \nu^2}$  is the coupling stiffness.
- $E$  is the Young's modulus.
- $\nu$  is the Poisson's ratio.
- $\rho$  is the material density.
- $F''_{x,\text{ext}}$  and  $F''_{y,\text{ext}}$  are external in-plane forces per unit area.

These equations show that the in-plane motions  $u$  and  $v$  are coupled due to Poisson's effect. To simplify the analysis, we can decouple the equations by introducing potential functions or considering plane wave solutions. For isotropic materials and in the absence of external forces, the equations can be decoupled into separate wave equations for longitudinal and shear waves. Assuming a plane longitudinal wave propagating in the  $x$ -direction and neglecting  $v$ , we obtain:

$$\frac{\partial^2 u}{\partial x^2} - \frac{1}{c_{LP}^2} \frac{\partial^2 u}{\partial t^2} = 0, \quad (2.86)$$

with the longitudinal plate wave speed:

$$c_{LP} = \sqrt{\frac{E}{(1 - \nu^2)\rho}}. \quad (2.87)$$

Assuming a plane shear wave and neglecting  $u$ , we obtain:

$$\frac{\partial^2 v}{\partial x^2} - \frac{1}{c_S^2} \frac{\partial^2 v}{\partial t^2} = 0, \quad (2.88)$$

with the shear wave speed:

$$c_S = \sqrt{\frac{G}{\rho}}, \quad (2.89)$$

where  $G = \frac{E}{2(1 + \nu)}$  is the shear modulus. The general in-plane motion is a superposition of longitudinal and shear waves. The coupling between  $u$  and  $v$  means that an initial disturbance in one direction will, in general, generate motion in both directions due to Poisson's ratio effects. For out-of-plane (bending) motion, the governing equation is derived from the plate's flexural rigidity. The equation of motion for bending waves in a thin plate is:

$$B \left( \frac{\partial^4 w}{\partial x^4} + 2 \frac{\partial^4 w}{\partial x^2 \partial y^2} + \frac{\partial^4 w}{\partial y^4} \right) + \rho h \frac{\partial^2 w}{\partial t^2} = p(x, y, t), \quad (2.90)$$

where:

- $w(x, y, t)$  is the transverse displacement.
- $B$  is the bending stiffness.
- $p(x, y, t)$  is the transverse load per unit area.

The bending stiffness  $B$  is given by:

$$B = \frac{Eh^3}{12(1 - \nu^2)}. \quad (2.91)$$

This is a fourth-order partial differential equation, reflecting that bending involves curvature of the plate.

### 2.10.2 Fundamental Concepts of SEA

Consider a mechanical system divided into  $n$  subsystems. Each subsystem can exchange vibrational energy with other subsystems and with the environment. The energy exchange is characterized by power inputs and losses, which are related to the vibrational energy stored in each subsystem. Let  $E_i$  denote the time-averaged vibrational energy stored in subsystem  $i$ , and  $\omega$  denote the angular frequency of interest. The power input  $P_i$  into subsystem  $i$  can be due to external excitations such as forces or moments acting on the subsystem. Each subsystem also experiences power dissipation due to internal damping, characterized by the Damping Loss Factor (DLF)  $\eta_i$ . The power dissipated within subsystem  $i$  due to damping is proportional to its stored energy:

$$P_{\text{diss},i} = \omega\eta_i E_i. \quad (2.92)$$

When subsystems are coupled, there is also power flow between them. The power transmitted from subsystem  $i$  to subsystem  $j$  is proportional to the stored energy in subsystem  $i$  and is characterized by the Coupling Loss Factor (CLF)  $\eta_{ij}$ :

$$P_{ij} = \omega\eta_{ij} E_i. \quad (2.93)$$

Similarly, the power transmitted from subsystem  $j$  to subsystem  $i$  is:

$$P_{ji} = \omega\eta_{ji} E_j. \quad (2.94)$$

Under the assumption of weak coupling, the net power flow from subsystem  $i$  to subsystem  $j$  is:

$$P_{i \rightarrow j} = P_{ij} - P_{ji} = \omega(\eta_{ij} E_i - \eta_{ji} E_j). \quad (2.95)$$

The global energy balance for subsystem  $i$  can then be written as:

$$P_i = \omega\eta_i E_i + \sum_{j \neq i} \omega(\eta_{ij} E_i - \eta_{ji} E_j), \quad (2.96)$$

where  $P_i$  is the total power input into subsystem  $i$ , including external excitations and net power exchange with other subsystems.



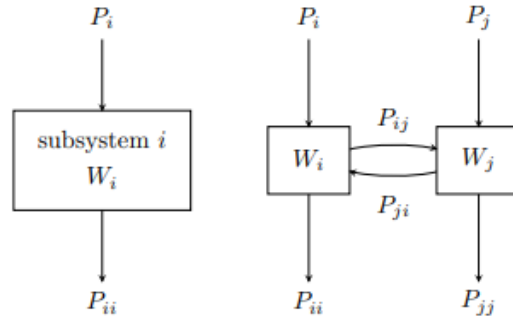


Figure 2.2: Energy flow in single and coupled subsystems.

Figure 2.2 illustrates the energy flow for a single subsystem and for coupled subsystems. In the single subsystem, energy is input and dissipated internally. In coupled subsystems, energy is also exchanged between subsystems.

### Reciprocity Relation

An important property in SEA is the reciprocity relation between the coupling loss factors  $\eta_{ij}$  and  $\eta_{ji}$ . Under certain conditions, the coupling loss factors satisfy the reciprocity relation:

$$n_i \eta_{ij} = n_j \eta_{ji}, \quad (2.97)$$

where  $n_i$  and  $n_j$  are the modal densities (modes per unit frequency) of subsystems  $i$  and  $j$ , respectively. This relation ensures energy conservation and reciprocity in energy exchange between subsystems.

### SEA Equations for Multiple Subsystems

For a system with  $n$  subsystems, we can write a set of  $n$  energy balance equations:

$$P_i = \omega \eta_i E_i + \sum_{j \neq i} \omega (\eta_{ij} E_i - \eta_{ji} E_j), \quad i = 1, 2, \dots, n. \quad (2.98)$$

These equations can be arranged into matrix form:

$$\mathbf{P} = \omega(\mathbf{\Gamma}\mathbf{E}), \quad (2.99)$$

where:

- $\mathbf{P} = [P_1, P_2, \dots, P_n]^T$  is the vector of power inputs,
- $\mathbf{E} = [E_1, E_2, \dots, E_n]^T$  is the vector of stored energies,

- $\Gamma$  is the system matrix incorporating damping and coupling loss factors:

$$\Gamma_{ii} = \eta_i + \sum_{j \neq i} \eta_{ij}, \quad \Gamma_{ij} = -\eta_{ji} \quad (i \neq j). \quad (2.100)$$

Solving these equations yields the vibrational energy levels  $E_i$  in each subsystem, from which other quantities of interest, such as vibration amplitudes and response spectra, can be derived.

### Coupling Loss Factors

In SEA, the coupling loss factor between two subsystems depends on the power transmitted across their interface. For plates connected at an angle, the coupling loss factor can be calculated based on the wave transmission coefficients for bending and in-plane waves. Consider two plates connected along a common edge at an angle  $\theta$ . The coupling loss factor  $\eta_{ij}$  can be expressed as:

$$\eta_{ij} = \frac{c_{g,i}}{2\pi f n_i} T_{ij}, \quad (2.101)$$

where:

- $c_{g,i}$  is the group velocity of waves in subsystem  $i$ .
- $f$  is the frequency.
- $n_i$  is the modal density of subsystem  $i$ .
- $T_{ij}$  is the transmission coefficient from subsystem  $i$  to  $j$ .

The transmission coefficient  $T_{ij}$  depends on the properties of the connection, material properties, and wave types involved. For bending waves at a joint between plates,  $T_{ij}$  can be calculated using continuity conditions for displacements and moments.

### Modal Density

The modal density  $n_i$  is a key parameter in SEA, representing the number of modes per unit frequency in subsystem  $i$ . For rectangular plates simply supported on all edges, the modal density for bending waves is:

$$n(f) = \frac{A f^2}{2\pi c_B^2}, \quad (2.102)$$

where:

- $A$  is the area of the plate.
- $c_B$  is the bending wave speed, given by:

$$c_B = \left( \frac{\omega^2 B}{\rho h} \right)^{1/4} = \left( \frac{2\pi f}{c_g} \right)^{1/2}, \quad (2.103)$$

- $c_g$  is the group velocity for bending waves:

$$c_g = 2 \left( \frac{B}{\rho h} \omega \right)^{1/2} = 2 \left( \frac{B}{\rho h} 2\pi f \right)^{1/2}. \quad (2.104)$$

By combining the understanding of wave propagation in plates with the SEA framework, we can model the energy distribution in complex structures made up of plate-like components. The SEA method allows us to estimate the vibrational energy levels in each subsystem and predict the system's response to external excitations. The key steps involve calculating the modal densities, damping loss factors, and coupling loss factors for each subsystem, and then solving the SEA energy balance equations. This approach is particularly powerful for high-frequency vibration analysis, where traditional deterministic methods are less effective.

### 2.10.3 Applying SEA to Complex Systems

To apply SEA to a complex system, the following steps are typically followed:

1. **Subdivision into Subsystems:** The system is divided into subsystems based on structural features, material properties, and expected modal behaviour. Subsystems should be large enough to contain many modes in the frequency range of interest.
2. **Calculation of Modal Densities:** The modal density  $n_i$  of each subsystem is calculated, usually using analytical expressions for simple geometries or numerical methods for complex shapes.
3. **Determination of Damping Loss Factors:** The damping loss factor  $\eta_i$  for each subsystem is determined, either from experimental measurements or estimated based on material properties and empirical data.
4. **Calculation of Coupling Loss Factors:** The coupling loss factors  $\eta_{ij}$  between subsystems are calculated. This often involves understanding the wave transmission between subsystems, which depends on their interface properties and the types of waves involved.

5. Assembly of SEA Equations: The energy balance equations are assembled using the calculated parameters.
6. Solution of SEA Equations: The equations are solved for the stored energies  $E_i$ .
7. Post-Processing: From the stored energies, other response quantities are calculated, such as mean-square velocities, accelerations, or sound pressure levels.

### Virtual SEA Analysis

Computational Vibroacoustic analysis at high frequencies presents several challenges. The grid refinement needed to accommodate short wavelengths often leads to overwhelming requirements in computational resources. But even when such requirements are met, the high modal density and high modal overlap of both structure and acoustic components introduce variability and uncertainty in local response results, rendering them highly inefficient indicators. Spatial and frequency averaging techniques, on the other hand, provide global indicator results that offer a better insight into the behaviour of complex systems under such circumstances. Originally, the theoretical foundations of SEA were set in a modal context. This description starts by considering two subsystems that are denoted in the following with subscripts 1 and 2, and are connected via non-dissipative coupling. The subsystems have a large number of modes  $N_1, N_2$ , with similar damping values, spread in equidistant frequency intervals throughout the frequency range of interest. Further, it is assumed that each mode of one subsystem is coupled to all modes of the other subsystem, but not to any of the modes within the same subsystem. For an isolated pair of two oscillators  $p$  and  $q$  that are excited with white noise forces, Lyon showed that the time-averaged energy flow between them is proportional to their vibration energy difference. In particular, the energy flow from  $p$  to  $q$  is given by:

$$p_{pq} = g_{pq} \cdot (e_p - e_q) \quad (2.105)$$

where  $e_p$  and  $e_q$  stand for the vibrational energy of the oscillators, and  $g_{pq}$  depends only on their characteristics. Back to the interaction of the two subsystems, it is now additionally assumed that the total vibration energy  $E$  of each subsystem is equally distributed among its modes, so that if  $p$  is a mode of subsystem 1,  $e_p = E_1/N_1$ . Then, the total energy flow from subsystem 1 to subsystem 2,  $P_{12}$ , equals the sum of the energy flows between the individual mode interactions. At this point, another important expression in SEA theory is introduced, the reciprocity relation:

$$n_{11}\eta_{12} = n_{12}\eta_{21} \quad (2.106)$$

where  $n_1, n_2$  are the modal densities, and  $\eta_{12}, \eta_{21}$  are the coupling loss factors (CLFs). The coupling loss factor is a parameter that appears exclusively in SEA.

$$P_{12} = \omega(\eta_{12}E_1 - \eta_{21}E_2) \quad (2.107)$$

This expresses the energy that flows out of subsystem 1 due to its interaction with subsystem 2. Further, introducing the power that is injected into subsystem 1, and the power dissipated in each subsystem due to its damping,  $\eta_j = \omega\eta_j E_j$ , the power balance for subsystem 1 becomes:

$$P_1 = P_{11} + P_{12} = \omega\eta_1 E_1 + \omega(\eta_{12}E_1 - \eta_{21}E_2) \quad (2.108)$$

The coefficient  $\eta_j$  that appears in the above expression is also called the Damping Loss Factor (DLF) of subsystem  $j$ . The power balance can be generalized to express the power balance of subsystem 1 in a global system that comprises an arbitrary number of  $k$  subsystems by invoking the Coupling Power Proportionality assumption. According to it, the energy flow between two subsystems is independent of the presence of a third subsystem or any number of subsystems. Then, the power balance for subsystem  $j$  in the general case can be written as:

$$P_i = \omega\eta_i E_i + \omega \sum_{i \neq j} (\eta_{ij} E_i - \eta_{ji} E_j), \quad i = 1, \dots, k \quad (2.109)$$

Or in compact matrix form:

$$P = \omega \cdot [\eta] E \quad (2.110)$$

As soon as matrix  $[\eta]$  is known, it can be used repeatedly to predict the response of the subsystems for any given vector of injected powers at a negligible computational cost. This matrix constitutes a reduced model, which describes the global system in terms of the energy content of its subsystems. This is what renders it well-suited for high-frequency simulations, where local indicator results are inefficient. We can deduce that the following relations hold for the CLFs and DLFs:

$$\eta_{ij} = -\eta_{ji} \quad \text{and} \quad \eta_j = \sum_{i \neq j} \eta_{ij} \quad (2.111)$$

### **Virtual SEA (Commercial Software)**

Virtual SEA is a novel method that proposes to compute the SEA parameters via an energy distribution model, similar to the experimental SEA, but using FEM computations instead of performing experiments in a laboratory. All the challenges linked to setting up experiments in the lab are now irrelevant. Also, the energies used to build the energy model no longer depend exclusively on bending waves. Instead, the contributing wave types can be controlled by the analyst, by appropriately configuring their simulation and computing the corresponding quantities.

### **Virtual Power Injection Method**

The numerical tool relies on the global modes of the components to compute frequency- and space-averaged injected powers and energy quantities. The virtual PIM is implemented by launching a series of automatically configured FE simulations, in which each of the subsystems is excited in turn. The setup of these simulations requires the frequency- and space-averaging parameters of the problem.

### **Subsystem Energy Computation**

Once the results of the virtual Power Injection Method are obtained, it is possible to produce the SEA parameter matrix, which in turn will yield the CLFs and DLFs of the model.

### **Analytic SEA**

Even though the underlying idea for the derivation of SEA equations is based on a modal context, most of the commercially available implementations of SEA employ Analytic SEA, which is a method based on the wave approach. According to this method, each subsystem of the physical model is represented in the SEA matrix by as many subsystem entries as the number of wave-types assumed to propagate in it. For example, a plate may correspond to three subsystems in the SEA matrix, standing for its bending, longitudinal, and shear waves. Further, the CLF at the junction between two subsystems is derived from the transmission coefficient of the junction. In other words, the coupling coefficient is derived as the ratio of energy flow associated with outgoing waves and energy associated with incident waves. A side effect of this process is that, since the transmission coefficients must only be calculated at the junctions between subsystems that are physically in contact, otherwise known as indirect CLFs, are zero. This, in general, results in sparse SEA matrices.

### Experimental SEA

One way to obtain the SEA parameters in complex geometries is via an energy flow analysis in situ.

### Power Injection Method

In this approach, the SEA parameter matrix  $[\eta]$  is regarded as a transformation matrix, and its computation is carried out by successive substitutions of  $P$  and  $E$  values in the same expression. The simplest way to achieve this is by injecting power into a single subsystem and taking energy measurements for the ensemble of the subsystems in the model. Iterating on these processes as many times as the number of subsystems, and injecting power in a different subsystem each time, eventually produces a diagonal matrix  $P$  on the left-hand side and a full  $E$  matrix on the right-hand side. Since the values of these matrices are the measurement results from the experiments, computing  $[\eta]$  is then a trivial task. For example, energy  $E_{ij}$  corresponds to the energy measured on subsystem  $i$  when power is injected on subsystem  $j$ . Given the size of the model, the SEA parameter matrix will be of size  $2 \times 2$ . The following system of equations can then be solved:

$$P_1 = \omega \cdot [\eta] \begin{bmatrix} E_{11} \\ E_{21} \end{bmatrix}, \quad P_2 = \omega \cdot [\eta] \begin{bmatrix} E_{12} \\ E_{22} \end{bmatrix} \quad (2.112)$$

Matrix  $[\eta]$  results from the above expression with a simple matrix inversion. Once the SEA matrix is known, the CLFs and DLFs can be computed.

**In a synthesis**

- Introduction to vibration analysis and shock response.
- Discussion on wave motion and its significance in shock analysis.
- Overview of modal analysis using mass-spring-damper models.
- Response of single-degree-of-freedom systems to nonperiodic excitations.
- Response of multi-degree-of-freedom systems to nonperiodic excitations.
- Frequency response function (FRF) analysis.
- Transfer function and modal decomposition techniques.
- Importance of modal parameters in understanding system dynamics.
- Statistical Energy Analysis (SEA) and its role in shock analysis.
- Strategies for transitioning from low to high frequencies in dynamic analysis.
- Application of SEA to complex systems and energy flow analysis.



# Chapter 3

## Shock Response Spectrum

### Contents

|       |  |    |
|-------|--|----|
| 3.1   | A bit of history . . . . .                             | 58 |
| 3.2   | Definition of SRS . . . . .                            | 59 |
| 3.3   | SRS Analysis and Mathematical Derivation . . . . .     | 60 |
| 3.3.1 | SRS Analysis for SDOF Systems . . . . .                | 60 |
|       | Damped SDOF System . . . . .                           | 61 |
| 3.3.2 | Shock Response Spectrum for SDOF . . . . .             | 61 |
| 3.3.3 | MDOF Systems and SRS . . . . .                         | 62 |
|       | Absolute Sum (ABSSUM) . . . . .                        | 63 |
|       | Square Root of the Sum of the Squares (SRSS) . . . . . | 63 |
| 3.4   | SRS synthesis . . . . .                                | 63 |
| 3.4.1 | Time-Domain Synthesis Methods . . . . .                | 65 |
|       | Wavelets . . . . .                                     | 65 |
|       | Damped sinusoids . . . . .                             | 65 |
|       | Enveloped sinusoids . . . . .                          | 65 |
| 3.5   | Application of SRS Methods to SDOF Systems . . . . .   | 67 |
| 3.5.1 | LTI Single-Degree-of-Freedom System . . . . .          | 68 |
| 3.5.2 | Viscoelastic Single-Degree-of-Freedom System . . . . . | 70 |

## 3.1 A bit of history

The concept of the Shock Response Spectrum (SRS) has a rich history that reflects the advancements in both theoretical mechanics and computational tools. It began in the early 20th century when engineers and scientists sought ways to understand and predict how mechanical systems respond to transient, high-intensity loads. During World War II, there was a growing need to analyse the effects of shock waves on structures and equipment, particularly in military contexts such as naval and aerospace applications. One of the early foundational works was by [103] in 1942, who explored the elastic and viscoelastic response of systems to transient excitations. Biot's work was significant because it laid the groundwork for the mathematical framework used to describe how structures behave when subjected to sudden, short-duration forces. Early research and application of the SRS began in the 1950s within the seismic community [104, 105], primarily to characterize the shock environment associated with earthquakes. Following, the use of SRS expanded considerably across the seismic, aerospace, and defence fields. In the early 1960s, the advent of digital computers significantly advanced the calculation of shock responses. Researchers like [106, 107] contributed to developing methods for numerically solving differential equations that governed system dynamics under transient loads. As computational power grew, engineers could simulate more complex systems and shocks with higher accuracy. This period saw the gradual adoption of the SRS as a standardised tool, especially in defence and aerospace fields [108–112]. By the 1970s, the SRS had become widely recognized as a tool for designing equipment that could survive the rigours of shock environments. [113] in 1979 introduced an improved recursive formula for calculating shock response spectra, which further simplified the process of determining how structures react to shock. Smallwood's formula made the calculation of SRS more efficient, which was especially important for real-world applications that required engineers to analyse complex systems in a timely manner. In subsequent decades, the automotive industry also saw the value of the SRS in understanding how vehicles and their components withstand impacts, such as crash scenarios. The development of more advanced computational tools and software, such as finite element analysis (FEA), has further enhanced the precision and ease with which engineers can calculate and interpret the SRS. Today, the Shock Response Spectrum remains an essential tool in engineering design, safety testing, and failure analysis. Modern applications of SRS range from evaluating the effects of earthquakes on structures to testing the durability of consumer electronics subjected to accidental drops or vibrations during shipping. As technology continues to evolve, especially with advancements in high-performance computing and real-time data analysis, the SRS will likely see further refinements and applications in new areas of engineering and technology.

## 3.2 Definition of SRS

Many structures are occasionally subjected to relatively large forces that are applied suddenly and over time intervals much shorter than the structure's natural period. These forces can lead to local damage or excite undesirable vibrations within the structure. In some cases, this vibration causes significant cyclic stresses, potentially damaging the structure or degrading its performance. Forces of this nature are referred to as shocks. Understanding the structural response to shocks is crucial for effective design. The severity of a shock is typically quantified by the maximum response of the system. For comparison, it is common practice to reference the response of an undamped single-degree-of-freedom system. The plot showing the peak response of a mass-spring system to a particular shock, as a function of the system's natural frequency, is known as a Shock Response Spectrum (SRS). The SRS helps in characterizing the dynamic behaviour of a structure or component under shock conditions by revealing which frequencies are most affected by the transient shock. Engineers commonly use SRS analysis in industries like aerospace, automotive, and defence to ensure components can survive and perform under sudden shock loads, like those encountered during rocket launches, seismic events, or explosions. This methodology not only helps in identifying the critical frequencies where the system might fail or suffer damage but also in designing structures or components to mitigate these effects by adjusting the system's natural frequencies to avoid excessive resonance or using damping to limit peak responses.

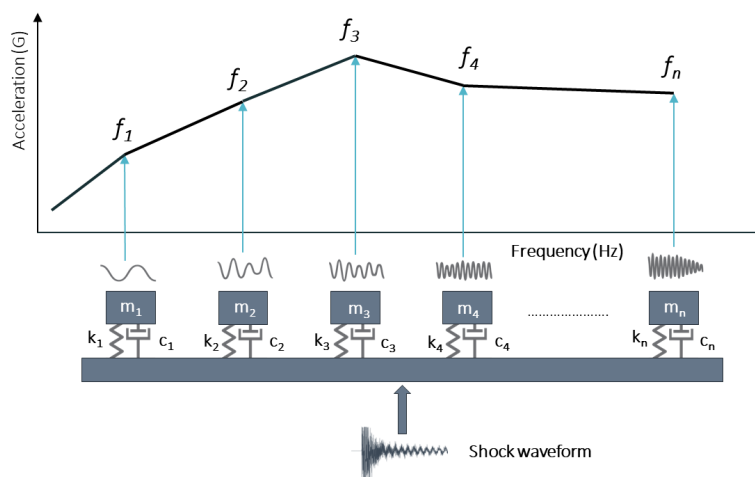


Figure 3.1: SRS graphical representation

A Shock Response Spectrum (SRS) provides a graphical representation that illustrates the maximum response of a system subjected to a shock input. The

SRS graph is created by considering a series of Single Degree of Freedom (SDOF) systems with varying natural frequencies. These systems are exposed to a transient shock event, and the maximum response for each system is plotted as a function of its natural frequency, as shown in 3.1. In constructing the SRS, the assumption is made that the base input to these SDOF systems does not interact with the systems themselves, meaning that the base motion remains unaffected by the oscillators. As you progress through the frequencies, each SDOF system responds differently. Lower-frequency systems tend to show smaller peak responses, while systems at intermediate frequencies may exhibit the highest peak accelerations. After reaching this peak, the response tends to decrease as the frequencies continue to increase, as observed in "stiffer" systems with higher natural frequencies. The damping values used in an SRS measurement are constant for all frequencies. For pyrotechnic events the damping used is typically 5% critical damping. In earthquake testing, 2% critical damping is typically used. The highest damage potential due to a shock input is at the natural frequencies of the test article. The SDOF model is used to predict the response of a product at its natural frequency to a given shock input. Since the natural frequency can be anywhere within the test frequency range, the SRS computes the peak SDOF response as a function of frequency at nth octave spacing.

### 3.3 SRS Analysis and Mathematical Derivation

In this section, we will derive and explain the SRS for both SDOF and MDOF systems.

#### 3.3.1 SRS Analysis for SDOF Systems

The SRS represents the maximum response of a system subjected to a base acceleration  $\ddot{u}_b(t)$  across a range of natural frequencies. This is widely used in dynamic analysis to evaluate how systems respond to transient shock events. The equation of motion for an SDOF system subjected to base motion is given by:

$$m\ddot{x}(t) + k(x(t) - u_b(t)) = 0 \quad (3.1)$$

where:

- $m$  is the mass,
- $k$  is the spring stiffness,
- $x(t)$  is the absolute displacement of the mass,

- $u_b(t)$  is the base displacement.

We define the relative displacement  $z(t)$  as:

$$z(t) = x(t) - u_b(t) \quad (3.2)$$

Substituting this into the equation of motion and rearranging, we obtain the standard form:

$$\ddot{z}(t) + \omega^2 z(t) = -\ddot{u}_b(t) \quad (3.3)$$

where  $\omega = \sqrt{k/m}$  is the natural frequency of the system.

### Damped SDOF System

In the case of a damped SDOF system, the equation of motion is modified to include a damping term:

$$\ddot{z}(t) + 2\zeta\omega\dot{z}(t) + \omega^2 z(t) = -\ddot{u}_b(t) \quad (3.4)$$

where:

- $\zeta$  is the damping ratio.

The response of the system can be solved using Duhamel's Integral or numerically:

$$z(t) = -\frac{1}{\omega} \int_0^t \ddot{u}_b(\tau) e^{-\zeta\omega(t-\tau)} \sin(\omega(t-\tau)) d\tau \quad (3.5)$$

The absolute acceleration of the mass is then related to the relative displacement by:

$$\ddot{x}(t) = -\omega^2 z(t) \quad (3.6)$$

### 3.3.2 Shock Response Spectrum for SDOF

The SRS is defined as the maximum absolute acceleration  $\ddot{x}(t)$  for each natural frequency  $\omega$ :

$$S_A(\omega) = \max_t |\ddot{x}(t)| \quad (3.7)$$

Substituting the expression for  $\ddot{x}(t)$  into this formula gives:

$$S_A(\omega) = \max_t \left| \omega \int_0^t \ddot{u}_b(\tau) e^{-\zeta\omega(t-\tau)} \sin(\omega(t-\tau)) d\tau \right| \quad (3.8)$$

This equation calculates the peak response at each frequency, which is key in determining the dynamic performance of the system when subjected to transient loads.

### 3.3.3 MDOF Systems and SRS

When analysing MDOF systems, the response is more complex because the system has multiple natural frequencies and mode shapes. The response of each mode can be approximated using mode superposition, where the system's dynamics are transformed from physical coordinates to modal coordinates. The governing equation of motion for the displacement  $\eta_i(t)$  of mode  $i$  in an MDOF system subjected to base excitation is:

$$\ddot{\eta}_i + 2\zeta_i\omega_i\dot{\eta}_i + \omega_i^2\eta_i = -\Gamma_i\ddot{u}_b(t) \quad (3.9)$$

where:

- $\eta_i(t)$  is the generalized coordinate for mode  $i$ ,
- $\zeta_i$  is the damping ratio for mode  $i$ ,
- $\omega_i$  is the natural frequency for mode  $i$ ,
- $\Gamma_i$  is the modal participation factor for mode  $i$ ,
- $\ddot{u}_b(t)$  is the base excitation acceleration.

This equation is similar to the SDOF system, but now each mode of the system has its own natural frequency and damping. The modal participation factor  $\Gamma_i$  accounts for how much each mode contributes to the overall response. Using mode superposition, the physical coordinates are transformed into modal coordinates:

$$\mathbf{x}(t) = \mathbf{\Phi}\boldsymbol{\eta}(t) \quad (3.10)$$

where:

- $\mathbf{x}(t)$  is the vector of physical displacements,
- $\mathbf{\Phi}$  is the modal matrix (containing eigenvectors),
- $\boldsymbol{\eta}(t)$  is the vector of modal displacements.

The equations of motion for each mode decouple into a series of independent SDOF systems, allowing the use of the SRS method for each mode. The maximum response for the system in terms of physical displacements can be calculated using:

$$\mathbf{x}_{\max} = \sum_{i=1}^n \Gamma_i \mathbf{\Phi}_i \max(S_A(\omega_i)) \quad (3.11)$$

This equation sums the contributions from all modes, using the modal participation factors and the peak SRS values for each mode. Since the maxima for all modes

do not occur at the same time, a root-sum-square (RSS) method is often used to estimate the total maximum response:

$$\mathbf{x}_{\max} = \sqrt{\sum_{i=1}^n (\Gamma_i \Phi_i S_A(\omega_i))^2} \quad (3.12)$$

Two common methods for estimating the total maximum response in MDOF systems are:

### Absolute Sum (ABSSUM)

This method conservatively assumes that all modes reach their maximum at the same time. The maximum relative displacement is calculated as:

$$(z_i)_{\max} \leq \sum_{j=1}^N |\hat{q}_{ij}| |\eta_j|_{\max} \quad (3.13)$$

where  $\hat{q}_{ij}$  is the mass-normalized eigenvector coefficient for coordinate  $i$  and mode  $j$ .

### Square Root of the Sum of the Squares (SRSS)

This method assumes that the maxima of different modes occur at different times and calculates the maximum displacement as:

$$(z_i)_{\max} \approx \sqrt{\sum_{j=1}^N (\hat{q}_{ij} \eta_j)_{\max}^2} \quad (3.14)$$

## 3.4 SRS synthesis

When a physical system must be shock tested to SRS requirements, the SRS itself cannot directly control the test machine. Synthesizing an acceleration time-history compatible with a design SRS is crucial, especially for tests using electrodynamic shakers [114, 115]. These machines have physical constraints on force and displacement. The peak shaker force is determined by the peak acceleration of the time-history and the test equipment's mass, while low-frequency tests face peak displacement issues. Therefore, in both cases, a synthesised SRS-compatible shock acceleration time-history is essential for accurate testing and analysis [116]. The transformation from the time domain to the Shock Response Spectrum (SRS) is relatively straightforward because it involves calculating the peak responses of

a series of single-degree-of-freedom (SDOF) systems subjected to a given time-domain acceleration input. The steps are as follows:

1. A known time-domain acceleration input is applied to a range of SDOF systems with varying natural frequencies and damping ratios.
2. The differential equation governing the motion of each SDOF system is solved to determine the response at each frequency.
3. For each SDOF system, the peak response (e.g., maximum displacement, velocity, or acceleration) is extracted from the time history.
4. The peak responses are plotted against the natural frequencies to generate the SRS.

This process is straightforward because it involves a direct calculation of the system's response to a known input using established equations of motion. The inverse transformation from SRS to the time domain is much more complex due to several factors:

- **Loss of Temporal Information:** The SRS only captures the peak responses of the system and does not retain any information about the time sequence or phase of the original acceleration signal. This means that multiple time-domain signals can produce the same SRS, making the inverse problem underdetermined.
- **Non-uniqueness:** Given an SRS, there are infinitely many possible time-domain signals that can correspond to it because the SRS is a summary of peak responses without phase information. This non-uniqueness requires additional constraints or assumptions to narrow down the possible solutions.
- **Causality and Physical Constraints:** Ensuring that the synthesised time-domain signal is causal (i.e., physically realizable) and adheres to the laws of physics adds another layer of complexity. Methods must carefully balance matching the SRS with maintaining causality, often leading to the use of iterative and approximate techniques.

These challenges highlight the need for iterative methods to accurately extract time-domain signals that are consistent with physical constraints. [117–125] have significantly contributed to defining SRS synthesis methods using various approaches such as wavelets, damped and enveloped sinusoids. Their work provides detailed methodologies for generating time-history waveforms that meet specific SRS criteria. These methods are particularly valuable for creating realistic shock testing scenarios and ensuring that synthesised signals can be effectively used in practical applications like electro-dynamic shakers [126].



### 3.4.1 Time-Domain Synthesis Methods

This section aims to compare different SRS synthesis methods to determine the most suitable technique for various types of systems subjected to a ground impulse load. The comparative analysis involves generating artificial SRS accelerations to replicate the input of a real experimental pyrotest and applying these to an LTI system and a viscoelastic system. Previous studies by [127, 128] have provided foundational methods for SRS synthesis, but this study aims to provide a comprehensive comparison of wavelets, damped sinusoids, and enveloped sinusoids. In this section, we explain the process of generating artificial SRS accelerations to replicate the input profile of a pyroshock pulse and we compare the effectiveness of the SRS synthesis on two single-degree-of-freedom systems, respectively LTI and viscoelastic.

#### Wavelets

A wavelet is a discrete waveform of limited duration that is suited for approximating data with sharp discontinuities [129]. The original signal can be reconstructed as a summation of a set of wavelets with specified parameters. The equation of a single wavelet  $W_m(t)$  is:

$$W_m(t) = \begin{cases} 0 & \text{for } t < t_{dm} \\ A_m \sin(2\pi f_m N_m(t - t_{dm})) \sin(2\pi f_m(t - t_{dm})) & \text{for } t_{dm} \leq t \leq t_{dm} + \frac{N_m}{2f_m} \\ 0 & \text{for } t > t_{dm} + \frac{N_m}{2f_m} \end{cases} \quad (3.15)$$

#### Damped sinusoids

The sinusoid approach shows a difference in the way the rise, peak, and decay of the waveform are controlled compared to the previously presented method. In this case, the parameters to control are slightly different:

$$W_m(t) = \begin{cases} 0 & \text{for } t < t_{dm} \\ A_m e^{-\xi_m 2\pi f_m(t-t_{dm})} \sin(2\pi f_m N_m(t - t_{dm})) \sin(2\pi f_m(t - t_{dm})) & \text{for } t \geq t_{dm} \end{cases} \quad (3.16)$$

It can be noted an extra term  $\xi_m$  that is the damped sinusoid damping ratio.

#### Enveloped sinusoids

The enveloped sinusoids with random phase angles approach is similar to the one of damped sinusoids. The equation for enveloped sinusoids is given by:

$$W_m(t) = E(t)A_m \sin(2\pi f_m t + \phi_m) \quad (3.17)$$

Where  $\phi_m$  are random phase angles for each frequency  $n$ . The rise, plateau, and decay of  $W_m(t)$  is controlled by an envelope function  $E(t)$  rather than damping. For all the three methods, iterations for the parameters of a set of  $m$  waveforms at time  $t$  yield a synthesised acceleration that is expressed as:

$$\ddot{\mathbf{x}}(t) = \sum_{m=1}^{N_m} \mathbf{W}_m(t) \quad (3.18)$$

An example of a synthesized time history from the SRS input in Table 3.1 with a duration of  $T = 0.06$  s can be seen in Fig. 3.2.

| Frequency [Hz] | Amplitude [g] |
|----------------|---------------|
| 100            | 56            |
| 1000           | 2820          |
| 10000          | 2820          |

Table 3.1: Shock load input

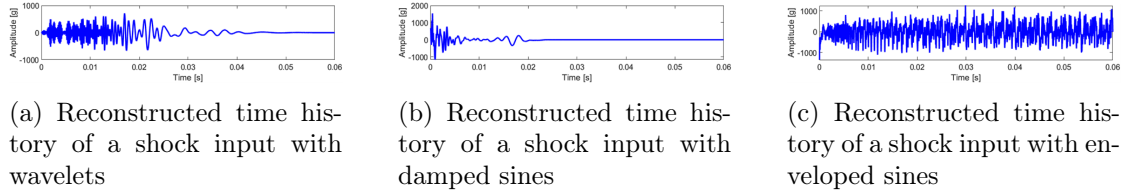


Figure 3.2: synthesised time history for the given shock input.

The synthesized accelerations have been converted to SRS and compared to the reference input as shown in 3.3.

Furthermore, the Synthesis Correlation Coefficient (COR) [6] in 3.2 has been computed in low, middle and high frequency range to compare the efficiency.

$$COR = \frac{\left| \sum_{f_1}^{f_2} f_n^2 SRS_r(f_n) SRS_s(f_n) \right|^2}{\sum_{f_1}^{f_2} f_n^2 SRS_r(f_n)^2 \sum_{f_1}^{f_2} f_n^2 SRS_s(f_n)^2} \quad (3.19)$$

Where  $SRS_r$  and  $SRS_s$  are respectively the reference and synthesised SRS. Globally, a good level of accuracy (near the unity) has been achieved. In particular, the enveloped sines method seems to be the most effective. It can be observed that the methods are less accurate in the middle frequency range (200-1000 Hz).

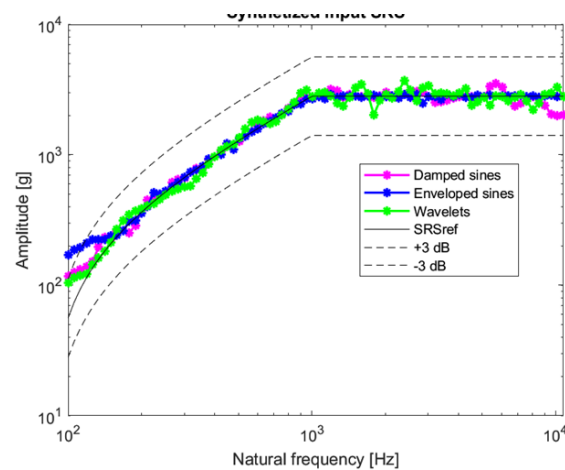


Figure 3.3: Synthesized SRS comparison.

| Frequency Range | Damped sines | Enveloped sines | Wavelets |
|-----------------|--------------|-----------------|----------|
| 100-200 Hz      | 0.98186      | 0.99566         | 0.99773  |
| 200-1000 Hz     | 0.97651      | 0.98699         | 0.96599  |
| 1000-10K Hz     | 0.98934      | 0.99421         | 0.98707  |

Table 3.2: Synthesis correlation coefficient

Overall, the investigated techniques, namely the summation of damped sines, enveloped sines, and wavelets, have shown good levels of accuracy in reproducing the desired SRS input. Further studies should be conducted by exploring different parameter settings and types of input profiles to enhance the understanding of these techniques. Additionally, the development of an optimization algorithm, such as the least square fitting method or genetic algorithm, should be pursued to combine the methods and synthesize a single SRS that minimizes the error and achieves a higher level of accuracy.

### 3.5 Application of SRS Methods to SDOF Systems

The synthesised SRS have been applied on a SDOF. A pyrotechnic signal derived by an experimental shock test was used 3.4. From the time domain we derived the signal in frequency domain using the SRS form 3.5. Using this SRS as a reference, an algorithm was employed to generate synthesised signals through three different methods (see Figures 3.6a, 3.6b, and 3.6c). Each synthesised signal was crafted to closely replicate the original shock response, resulting in a high degree of overlap between the original and reproduced signals across all methods. These synthesised signals were then used as input for both the Single Degree of Freedom (SDOF)

linear time-invariant (LTI) system and the viscoelastic system to analyse their respective responses.

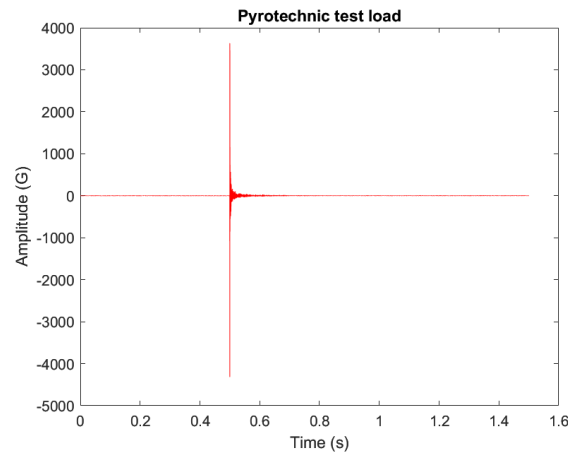


Figure 3.4: Pyrotechnic signal derived by an experimental shock test

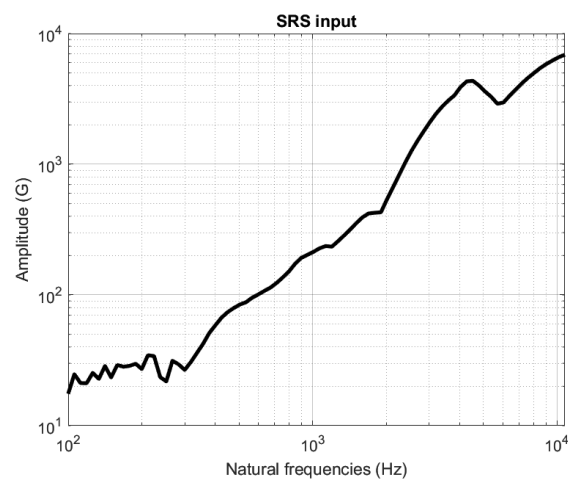


Figure 3.5: SRS derived by the pyrotechnic signal

### 3.5.1 LTI Single-Degree-of-Freedom System

The three synthesised SRS were applied to a system to compare the resulting responses with the solution obtained when using the original signal as input. The responses of the system to the synthesised signals were computed by solving the equation of motion of a single-degree-of-freedom (SDOF) linear time-invariant (LTI) system, chosen here as a simple example (see 3.7). The four SRS inputs

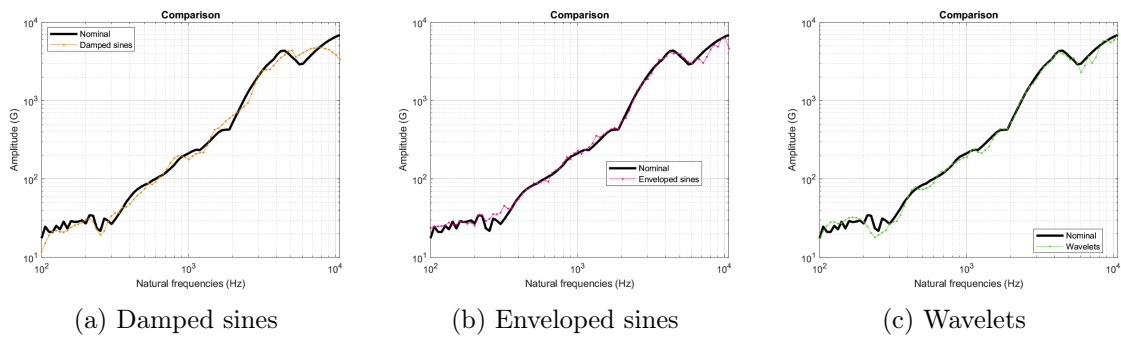


Figure 3.6: SRS comparison between the test-derived SRS and the synthesised SRS using the three synthesis methods

were applied as base acceleration, and the system's response over time was computed by numerically integrating the differential equations, as illustrated in 3.9a, 3.9b, and 3.9c. A close overlap among the system responses in SRS form can be observed in Figure 3.10. Subsequently, the original signal was used to analyse the system's behaviour through frequency response analysis. In this approach, the frequency response of the SDOF system is derived from the transfer function:

$$H(j\omega) = \frac{1}{m(j\omega)^2 + cj\omega + k} \quad (3.20)$$

where  $j\omega$  is the frequency variable in the complex domain, and  $m$ ,  $c$ , and  $k$  are the system's mass, damping, and stiffness, respectively. By evaluating  $H(j\omega)$  across a range of frequencies, the magnitude and phase of the system's response to the original signal can be determined 3.11. This frequency-domain response serves as a comparison point to verify the accuracy of the responses obtained using the synthesised inputs 3.12.

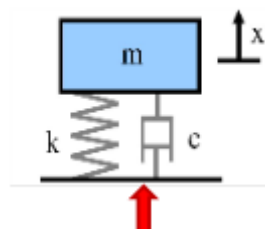


Figure 3.7: Single-Degree-of-Freedom Mass-Spring-Damper linear system

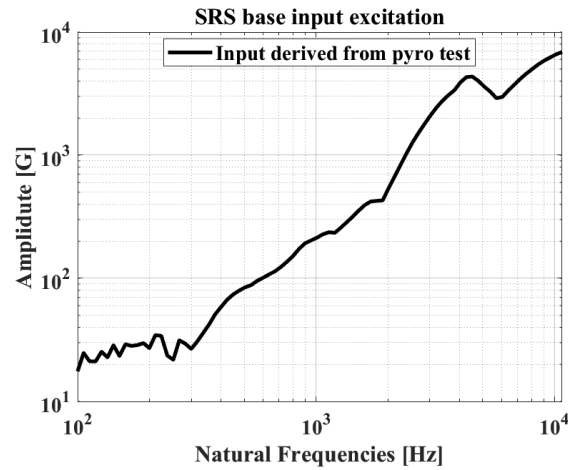
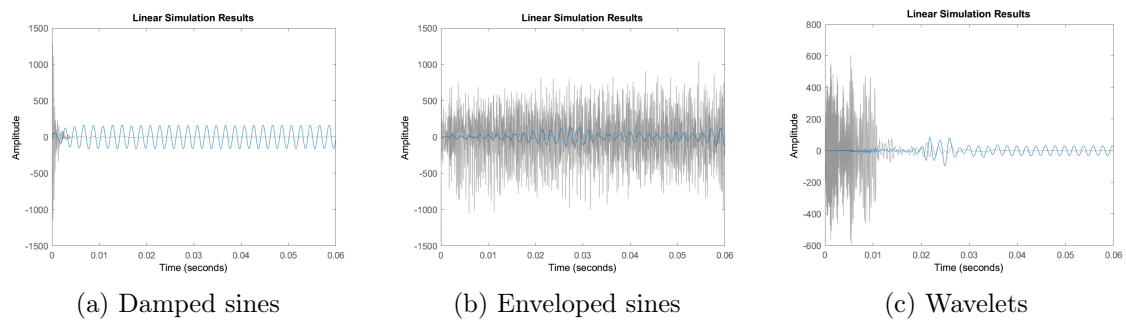


Figure 3.8: Base input acceleration in SRS form



(a) Damped sines

(b) Enveloped sines

(c) Wavelets

Figure 3.9: Matlab lsim for LTI system

### 3.5.2 Viscoelastic Single-Degree-of-Freedom System

In this subsection, we repeat the same procedure as in the previous analysis, but now applied to a viscoelastic system, as shown in 3.13 .

The viscoelastic model chosen is the standard linear viscoelastic model, which consists of a Maxwell element (a spring in series with a dashpot) arranged in parallel with a purely elastic spring. This configuration captures both immediate elastic behaviour and delayed viscous response, representing the time-dependent properties characteristic of viscoelastic materials. In a viscoelastic system, the total force applied,  $F(t)$ , is the sum of the forces on each branch of the model. For the Maxwell element, which consists of a spring  $k_1$  in series with a dashpot  $c$ , the force can be expressed as:

$$F_2(t) = k_1 (u(t) - v(t)) = c\dot{v}(t) \quad (3.21)$$

where  $u(t)$  is the displacement,  $v(t)$  is the displacement of the dashpot, and  $\dot{v}(t)$  is its velocity. The force in the parallel spring, with stiffness  $k_0$ , is:

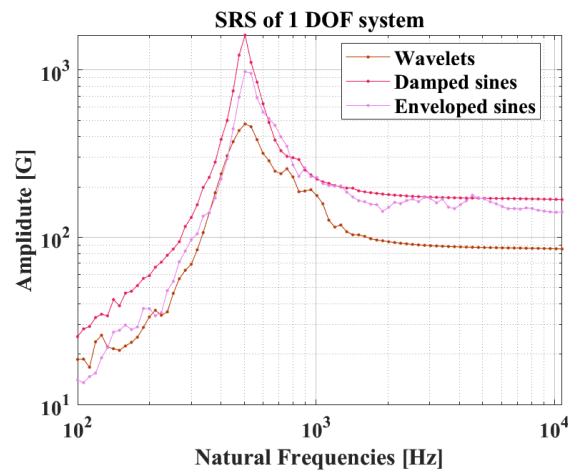


Figure 3.10: SRS response of a SDOF LTI system to a shock base input

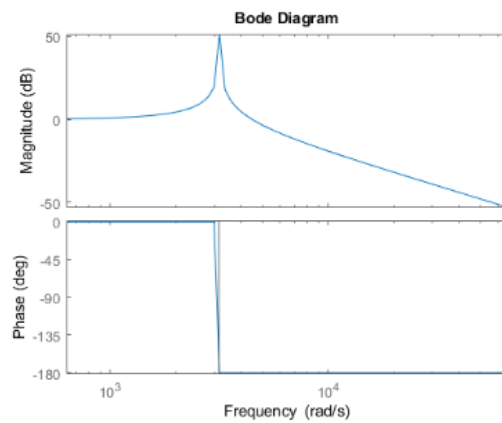


Figure 3.11: Analytical solution of the sdof LTI system for comparison

$$F_1(t) = k_0 u(t) \quad (3.22)$$

Thus, the total force is given by:

$$F(t) = F_1(t) + F_2(t) = k_0 u(t) + k_1 (u(t) - v(t)) = k_0 u(t) + c \dot{v}(t) \quad (3.23)$$

By manipulating these equations, we can derive a linear differential equation for the system's behaviour with respect to the unknown displacement  $u(t)$ , as shown in [130]. Next, to express the creep function  $J(t)$ , which describes the time-dependent deformation under a constant load, we solve the differential equation with an applied force  $F(t)$  as a step function. The creep function for this standard linear model is given by:

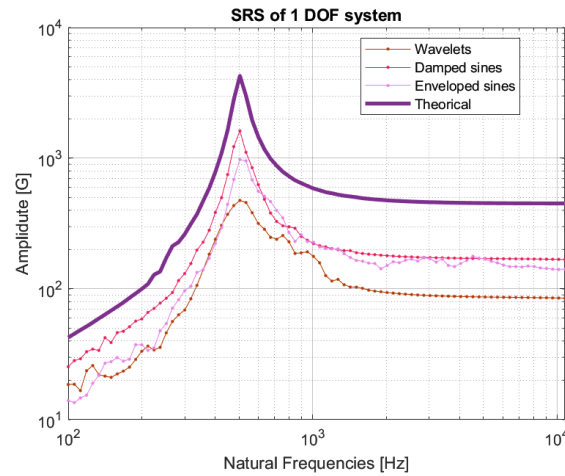


Figure 3.12: SRS response of a SDOF LTI system to a shock base input, comparison with the analytical solution

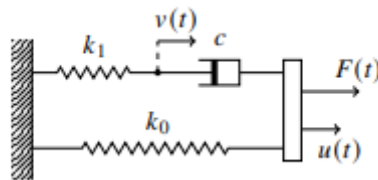


Figure 3.13: Standard linear viscoelastic model

$$J(t) = \frac{1}{k_0} \left( 1 + \frac{1}{\beta} (1 - e^{-t/\beta}) \right) \quad (3.24)$$

where  $\beta = \frac{k_0}{k_1}$ , representing a characteristic time for the viscoelastic response. The relaxation function  $G(t)$ , which describes the system's response to a unit step in strain, also reflects the viscoelastic nature. For the standard linear model, the relaxation function is expressed as:

$$G(t) = k_0 + k_1 e^{-t/\tau} \quad (3.25)$$

where  $\tau = \frac{c}{k_1}$  is the characteristic relaxation time associated with the Maxwell element.

Finally, in the frequency domain analysis, the viscoelastic behaviour can be fully described by the complex modulus  $K(\omega)$ , which combines the real (storage) and imaginary (loss) components of the material's response. For the standard linear viscoelastic model, the complex modulus  $K(\omega)$  is given by:



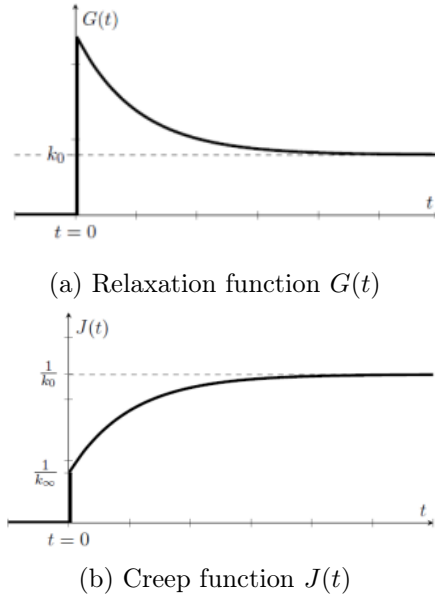


Figure 3.14: Relaxation and creep functions for the standard linear viscoelastic model.

$$K(\omega) = k_0 + k_1 \frac{i\omega\tau}{1 + i\omega\tau} \quad (3.26)$$

Splitting  $K(\omega)$  into its real and imaginary parts, we obtain:

$$K(\omega) = k_0 + k_1 \frac{\omega^2\tau^2}{1 + \omega^2\tau^2} + ik_1 \frac{\omega\tau}{1 + \omega^2\tau^2} \quad (3.27)$$

The response of the system to the synthesised SRS inputs was obtained in the same manner as with the LTI system, by numerically solving the differential equations of motion for the system under base excitation. The solution involves applying the synthesised accelerations as base input and computing the system's response over time using numerical integration techniques 3.15a, 3.15b, and 3.15c. The results for each input signal in terms of system response and comparison with the analytical solution are shown in Figures 3.16. For frequency-domain analysis, the transfer function of the viscoelastic system is derived, analogous to the transfer function used in the previous LTI system analysis 3.17. This frequency response was calculated to compare with the response obtained using the synthesised signals, allowing us to validate the accuracy of the synthesised inputs 3.18.

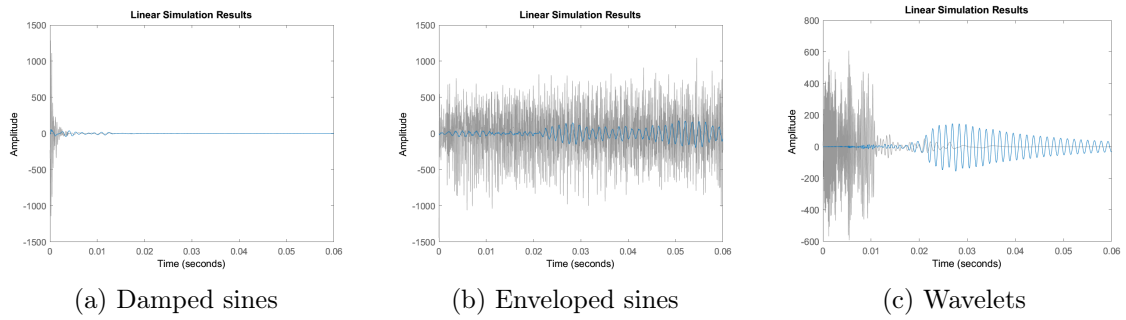


Figure 3.15: Matlab lsim for Viscoelastic linear system

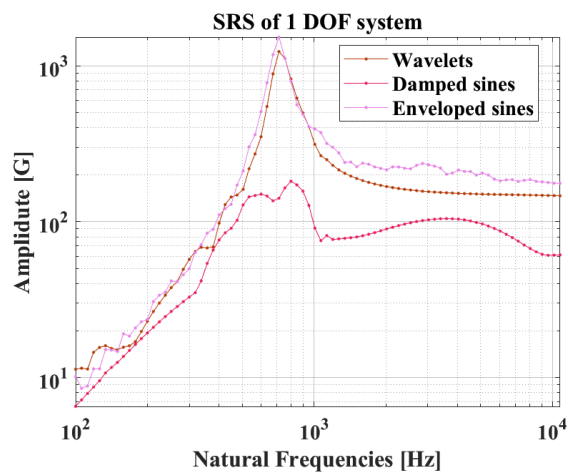


Figure 3.16: SRS response of a SDOF viscoelastic linear system to a shock base input

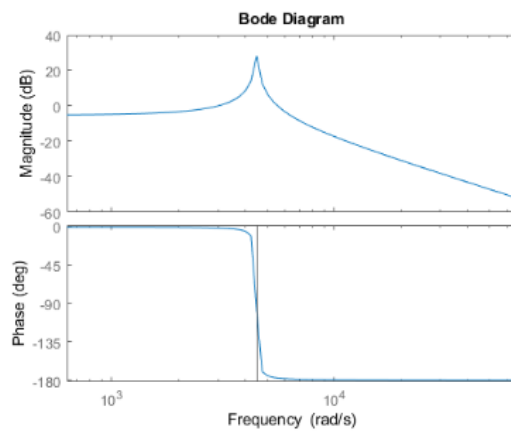


Figure 3.17: Analytical solution of the sdoF viscoelastic linear system for comparison

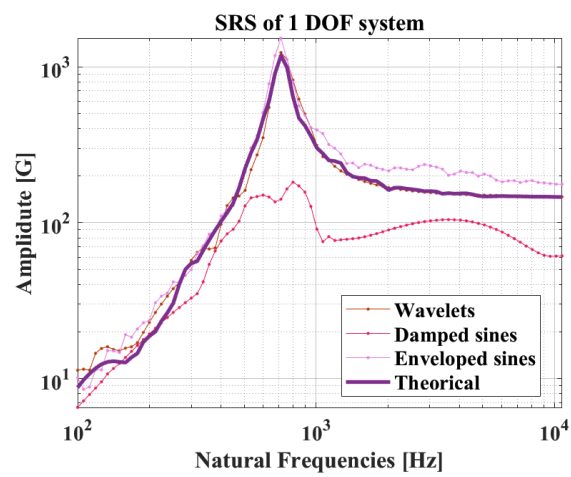


Figure 3.18: SRS response of a SDOF viscoelastic linear system to a shock base input, comparison with the analytical solution

**In a synthesis**

- Historical development and significance of the Shock Response Spectrum (SRS) in engineering.
- Definition and construction of the SRS, including its role in evaluating system responses to transient shocks.
- Detailed derivation of the SRS for Single-Degree-of-Freedom (SDOF) and Multi-Degree-of-Freedom (MDOF) systems.
- Overview of time-domain synthesis methods for constructing SRS-compatible waveforms, such as wavelets, damped sinusoids, and enveloped sinusoids.
- Comparative analysis of time-domain synthesis methods and their effectiveness across frequency ranges.
- Application of the time-domain synthesis methods to calculate the response of a SDOF Linear-Time-Invariant (LTI) system and to a SDOF viscoelastic linear system
- Application of synthesised SRS signals to SDOF and viscoelastic systems for practical shock response evaluation.

# Chapter 4

## Shock Analysis Standard in Industry

### Contents

|       |   |    |
|-------|---|----|
| 4.1   | Industry Standards and Challenges . . . . .       | 78 |
| 4.1.1 | The V Model . . . . .                             | 79 |
| 4.1.2 | Types of Mechanical Shocks and Sources . . . . .  | 80 |
|       | Launcher-induced shocks . . . . .                 | 81 |
|       | Clampband Release . . . . .                       | 82 |
| 4.1.3 | Shock Test Methods and Facilities . . . . .       | 83 |
|       | Clampband Release Test . . . . .                  | 83 |
|       | Pyronuts Release System . . . . .                 | 83 |
|       | SHOGUN Method . . . . .                           | 83 |
|       | VEGA/VESTA Method . . . . .                       | 84 |
|       | Appendage release . . . . .                       | 85 |
|       | Real launch vehicle stage separation . . . . .    | 85 |
| 4.2   | Case Study: Multi-launcher Platform . . . . .     | 85 |
| 4.2.1 | Mechanical properties . . . . .                   | 85 |
| 4.2.2 | Modal analysis and resonance search . . . . .     | 88 |
| 4.2.3 | Damping evaluation . . . . .                      | 88 |
| 4.3   | Experimental set up . . . . .                     | 89 |
| 4.3.1 | Instrumentation . . . . .                         | 92 |
| 4.3.2 | Input and tolerances . . . . .                    | 92 |
| 4.3.3 | Pass/Fail criteria . . . . .                      | 93 |
| 4.4   | Shock prediction using Empirical method . . . . . | 94 |

In this chapter, we will explore the industrial aspect of this work, focusing on the activities carried out at SITAEL, specifically on a Multi-Application Minisatellite project. The case study presented here centres on the Structural Model (SM) of the Minisatellite, a satellite developed by the company. In this section, we will describe SITAEL's spacecraft development processes, provide an overview of shock phenomena during the service life of the launcher/spacecraft and tests that are performed on ground. Successively, we will present the Minisatellite structure and its key parameters, share the results of the modal analysis, and present the shock test specification developed to validate the predictive shock method. Finally, we will introduce the empirical standard methodology used in industry to predict the shock response at the critical units.

## 4.1 Industry Standards and Challenges

A critical step of the spacecraft development process is the qualification phase, which is where the mechanical environmental test campaign is performed. Qualification testing shall be performed to provide evidence that the spacecraft performs in accordance with its specifications in the intended environments with the specified qualification margins [131]. Among the several tests that can be applied to a spacecraft during the mechanical environmental test campaign, one of the most severe is the shock test. Shocks in space structures are produced by pyrotechnic devices placed in the launchers initiating the stage or fairing separations. In addition, other less intense shock sources can be the deployment mechanisms for solar cells, antennas, and other satellite components [132]. Because of the high frequency content, many hardware elements and small components are susceptible to pyroshock failure while resistant to a variety of lower frequency environments. Specifically, cracks and fractures in crystals, ceramics epoxies and solder joints, relay and switch chatter and transfer, failures in circuit boards and computer memory are attributed to pyroshock exposure [110]. Hence, shock tests are performed to measure how much an electronic unit can withstand at the interface. High frequencies may make traditional analytical methods and computational procedures insufficient for system verification under pyroshock loading. Thus, after the analysis on the model, pyroshock verification should be accomplished experimentally. However, shock test results to be expensive and time consuming. There are two notably reasons. The former is due to the shock properties: they are very high amplitude and short duration transient loads that mainly occurs through impact or pyrotechnic explosions. In order to prevent damage of any component, the Structural Model (SM) of the spacecraft is commonly built. The SM usually consists of a representative structure, with structural dummies of the flight equipment, and also includes representative mechanical parts of other subsystems

(e.g., mechanisms and solar panels). Shock tests are hardly ever executed on the flight model, which is the spacecraft manufacture prefixed to launch. The latter reason is that replicating a pyrotechnic explosion could be very challenging. [133] found out that the pyrotechnic explosion shock and strain energy release shock are the two sources of the separation shock, which are difficult to simulate due to their boundary conditions. Also, boundary conditions can significantly affect the behaviour of the spacecraft during tests. There is another issue related to the spacecraft qualification. Even if the test is well performed and successful, the dynamic response of the SM could be above the expected levels. Thus, it is necessary to inspect and, eventually, fix any problem that has occurred in the manufacturing and design processes. For these reasons, being able to predict the response to any input, boundary condition, and design of the structure would be very advantageous. There would not be any need to qualify the SM through a test and redesign the structure. The aim of the work within the industry framework is to model, with a certain accuracy and robustness, the dynamical behaviour of the spacecraft when it is subjected to shock loads. This approach helps optimise both time and cost during the environmental test campaign, ensuring the spacecraft can reliably operate in the extreme conditions of space.

### 4.1.1 The V Model

At SITAEL, the V-Model is employed as a systematic development methodology. It provides a structured, step-by-step approach that ensures each phase of the spacecraft's design and development is thoroughly verified and validated. It can be observed in 4.1. The V-Model is similar to a waterfall approach, where broad design phases lead into progressively more detailed ones, with testing and verification occurring in parallel to ensure alignment with the system's requirements. In spacecraft development, this model is crucial as it helps to map the various stages of satellite design, moving from the satellite level down to its subsystems and finally individual components. In the case of the Multi-Application Minisatellite, for example, the spacecraft's structure includes the bus module, which houses key systems such as avionics, propulsion, and thermal regulation, and the payload module, which is designed to support the main mission. Each step of this process has associated requirements, and the V-Model helps ensure that these requirements are met at each level. Once the design phase is complete, the analysis phase begins. This involves developing mathematical models that simulate how the spacecraft will respond to various environmental factors, including mechanical stress and thermal conditions. These simulations are then tested against real-world data, allowing for a cycle of verification and adjustment. For instance, in our case study, thermomechanical analysis on the spacecraft provides data that feeds into the mechanical environmental tests, such as the shock tests performed

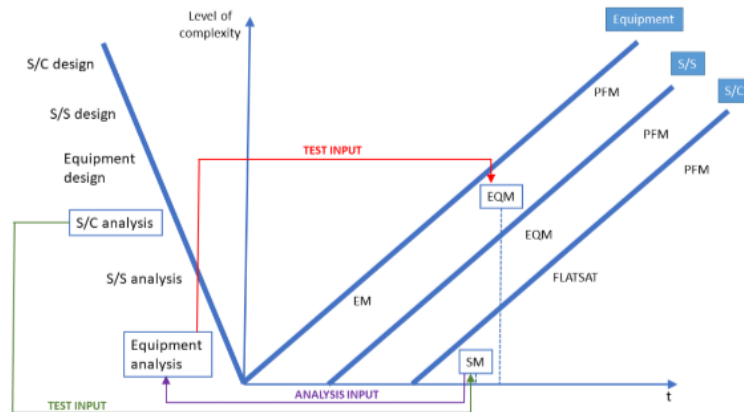


Figure 4.1: Honeycomb materials properties

on the Structural Model (SM). After the tests are conducted, the data collected (such as the loads transmitted to individual units) is compared with the values predicted by earlier models, including those calculated using the "linear extrapolation law." The goal is to determine whether the real-world results align with the predictions:

- If the transmitted loads match or fall below the predicted values, no further action is needed, and the components can proceed to qualification on the Engineering Qualification Model (EQM).
- If the transmitted loads exceed the predicted values, further analysis and testing must be conducted. This may involve adjusting the design specifications and performing new tests to ensure the equipment can withstand the actual conditions.

If the equipment has already passed the EQM/EM tests, a "delta test" may be performed to quickly confirm its ability to handle the updated load conditions. If the load exceeds the design's tolerance, modifications to the unit may be required to bring it up to standard. In short, SITAEL's use of the V-Model ensures that each phase of spacecraft development is rigorously tested and validated, preventing issues from escalating during later stages, such as flight testing.

### 4.1.2 Types of Mechanical Shocks and Sources

As presented in 4.2 we can make a distinction between shocks that happen in real life, and the tests we can perform on ground in order to ensure that the structure and the equipment will withstand the operational loads. In this subsection a



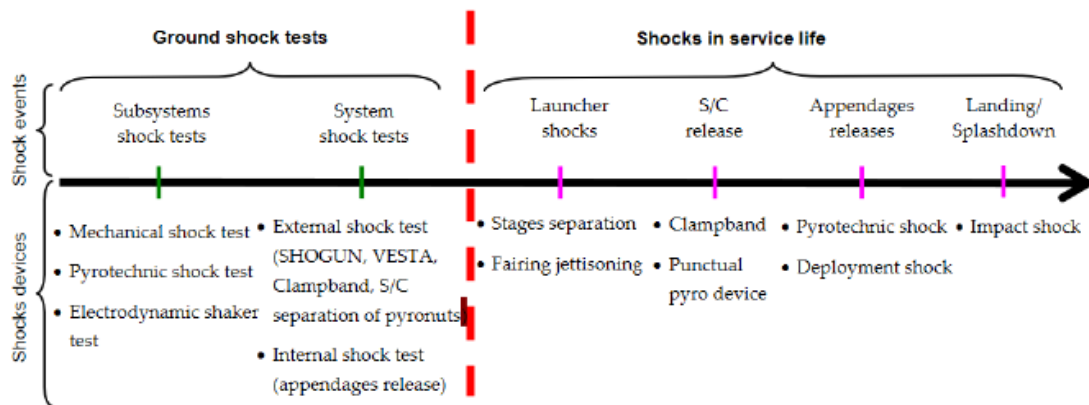


Figure 4.2: Ground shock tests and shocks in service life

brief explanation of the shocks that occur during service life of the spacecraft is provided.

### Launcher-induced shocks

Launcher-induced shocks encompass all shocks generated within the launcher structure, which propagate through both the launcher itself and the payload adapter up to the spacecraft interface. These shocks are predominantly attributed to stage separation and fairing jettisoning events. However, clampband release is not typically classified as a launcher-induced shock. The intensity of the launcher-induced shock experienced by the spacecraft largely hinges on the type of separation devices utilized during stage separation or fairing jettisoning 4.3, as well as on the overall architecture of the launcher, specifically the spatial separation and load path characteristics between the shock sources and the spacecraft interface. Each launcher exhibits unique characteristics in terms of shock transmission, preventing a universal rule from being applied across all designs. For example, the VEGA launcher experiences its most significant shock from fairing separation, primarily for frequencies up to approximately 3 kHz. For higher frequencies, however, the dominant shock source shifts to upper stage separation. The nature of launcher-induced shocks is shaped by the type of separation mechanism employed, and several key characteristics can be identified:

- Frequency Content of the Excitation:** Launcher-induced shocks contain mainly low-frequency components, typically ranging from 300 Hz to 1 kHz. These components stem from the modal responses of certain launcher elements, which effectively transmit to the spacecraft-launcher interface. The stiffness and diameter of the separation interface critically influence these



Figure 4.3: Fairing jettisoning

low-frequency components.

- **Distance-Related Attenuation:** High-frequency shock levels attenuate more rapidly with increasing separation distance from the shock source, due to dissipation and diffraction effects, which are amplified by the complexity of the propagation path, such as structural joints. This attenuation effect is less prominent for low and medium frequencies, which are efficiently transmitted to the spacecraft-launcher interface.

### Clampband Release

The clampband release system is a commonly used separation mechanism, comprising a clampband set, release mechanism, and separation springs, as depicted in 4.4. The clampband typically includes clamp segments that secure the payload adapter to the spacecraft rings, and a retaining band that applies clamping forces to the segments. For separation, a pyrotechnic mechanism (e.g., bolt-cutters) severs the tension bolts, allowing the clamp segments to release the payload adapter and spacecraft rings. This release event generates a shock with two main components:

- A high-frequency component, induced by the pyrotechnic device used to cut the clampband tension.
- A medium-frequency component, resulting from the rapid relaxation of the clampband's pre-tension.

When cylindrical symmetry is maintained, the pre-tension release excites the first breathing mode ( $n=0$ ), leading to radial expansion and contraction. The frequency of this mode is directly linked to the interface diameter and the material properties of the pre-loaded structure. Analytical expressions for the frequency and associated

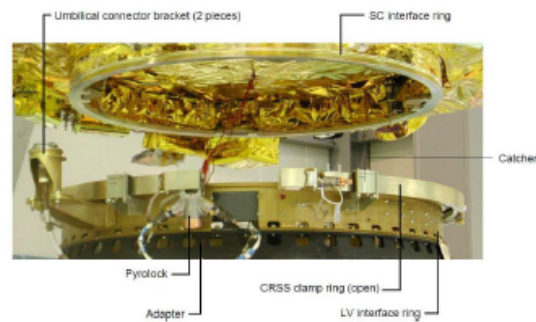


Figure 4.4: Clampband Release System

maximum acceleration can be derived, accounting for material characteristics, ring radius, tensile load distribution, and effective ring area.

### 4.1.3 Shock Test Methods and Facilities

These industry-standard test methods provide reliable approaches to qualifying spacecraft for the shocks expected during various stages of launch. Each method is tailored to replicate specific launcher configurations, thereby supporting effective spacecraft shock qualification.

#### Clampband Release Test

In this test, the spacecraft and launch vehicle adapter are hoisted in a free-free condition, with the clampband tension set close to its flight value. The assembly is lifted with a dedicated frame, and a foam mat is positioned to cushion the drop upon clampband release. This setup aims to replicate the physical separation of the spacecraft from its adapter.

#### Pyronuts Release System

For pyronuts systems, it is essential to replicate flight boundary conditions. The spacecraft is hung, and after firing, the pyronut is released, simulating in-flight conditions.

#### SHOGUN Method

The SHock Generator UNit (SHOGUN), shown in 4.5, is a specialised tool for replicating Ariane 5 launcher shock characteristics. The SHOGUN method mimics stage separation by utilizing a pyrotechnic tube that generates shock through

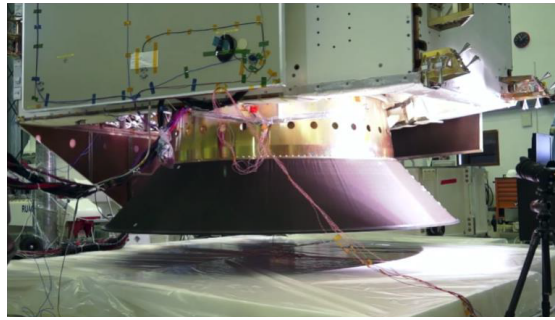


Figure 4.5: SHOGUN Test



Figure 4.6: VESTA Test

controlled expansion, though with boundary conditions distinct from actual flight conditions.

### **VEGA/VESTA Method**

The VEGA Shock Test Apparatus (VESTA) is a test tool specifically designed for the VEGA launcher to simulate shocks during fairing jettisoning. It employs a realistic model of the VEGA upper composite, which includes key components like the fairing belt and bolt cutters, achieving shock levels representative of in-flight events. The VESTA method allows for shock tuning by adjusting the tension of the Horizontal Separation System (HSS) belt, providing a validated procedure for spacecraft qualification. 4.6 illustrates the VESTA setup, highlighting the components involved and the control over shock levels through belt tension adjustments.

### Appendage release

It is not necessary to have a free-free configuration as the boundary conditions for the appendage and its supporting structure are made by the neighbouring parts of the structure and not by the spacecraft global boundary conditions. However installation of zero-g compensation equipment is usually necessary.

### Real launch vehicle stage separation

When fully representative LV stage separations are performed at system level, the test configuration and the associated boundary conditions are more complex as several pieces of structure are involved.

## 4.2 Case Study: Multi-launcher Platform

The Multi-launcher Platform of the Multi-Application Minisatellite is composed by:

- Bus Module structure: supports mechanically the overall Payload Module.
- Payload Module (PM) structure is mated onto the Bus Module and includes the specific supporting structure required to link (thermo-)mechanically the Payload System to Platform Module.

Our study case is the Structural Model of the spacecraft. The SM is designed to be mechanically representative of the spacecraft and it is used to perform qualification tests. A drawing of the SM is shown in Figure 4.7. The SM is composed by two parts:

- Structural part
- Dummy masses, that simulate the mechanical properties of the equipment and the harness.

The peculiarity of this item lies in its recurrent platform, meaning that the platform can be adapted to multiple launchers and payloads.

### 4.2.1 Mechanical properties

In 4.1 the mechanical properties of the SM are reported, namely its mass, CoG, MoI.

The material properties are summed up in 4.8, 4.9, 4.10 and 4.11:

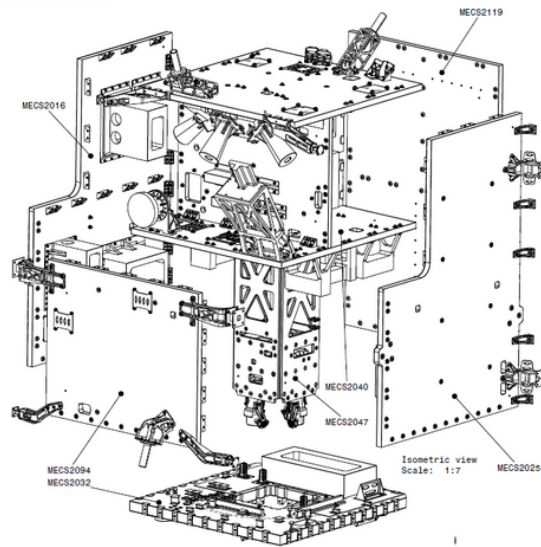


Figure 4.7: Drawing of the Structural Model (SM)

|                          | Value       |             |             | Property |
|--------------------------|-------------|-------------|-------------|----------|
| Mass [Kg]                | 324         |             |             |          |
| CoG [mm]                 | X: 5.86     | Y: -6.097   | Z: 569.862  |          |
| MoI [Kg m <sup>2</sup> ] | Ixx: 69.512 | Iyy: 81.774 | Izz: 50.196 |          |
|                          | Ixy: -0.511 | Iyz: -1.351 | Izx: 0.506  |          |

Table 4.1: Mechanical properties of the SM

| ID | Material     | Thickness /diameter (mm) | Young's Modulus E [GPa] | Poisson's ratio $\nu$ | Density $\rho$ [kg/m <sup>3</sup> ] | Tensile Yield Strength $\sigma_y$ [Mpa] | Tensile Ultimate Strength $\sigma_u$ [Mpa] | Thermal Expansion Coefficient [ppm/°C] | Ref.          | Use         | Remarks |
|----|--------------|--------------------------|-------------------------|-----------------------|-------------------------------------|---|--|--|---------------|-------------|---------|
| 1. | AA7075-T7351 | t<63.5                   | 71.0                    | 0.33                  | 2800                                | 359                                     | 455  | 22.0                                   | MMPDS         | Plates      | A-Basis |
| 2. | AA7075-T6    | t<1.0                    | 71.0                    | 0.33                  | 2800                                | 462                                     | 524  | 22.0                                   | MMPDS         | Face Sheet  | A-Basis |
| 3. | AA6061-T6    | w<12.5                   | 68.0                    | 0.33                  | 2710                                | 241                                     | 290  | 23.6                                   | MMPDS         | Wave Guides | A-Basis |
| 4. | AISI 316L    | -                        | 190.0                   | 0.27                  | 7920                                | 172                                     | 483  | 16.2                                   | ASME B31.3    | Tube        | S-Basis |
| 5. | Ti6Al4V      | t<50.8                   | 110.3                   | 0.31                  | 4430                                | 827                                     | 896  | 8.8                                    | MMPDS         | Plates      | A-Basis |
| 6. | AA6060-T6    | <3                       | 69.0                    | 0.33                  | 2680                                | 150                                     | 190  | 22.0                                   | EN 755-2:2008 |             |         |
| 7. | AA6082-T651  |                          | 70                      | 0.325                 | 2670                                | 270                                     | 230  | 22.5                                   | MAPTIS        |             |         |

Figure 4.8: Isotropic materials properties

| ID | Material   | Cell Size | Pcf | Compressive         |                |                | Crush Strength [MPa] | Plate Shear   |                |               |                | Ref.      | Remark |
|----|------------|-----------|-----|---------------------|----------------|----------------|----------------------|---------------|----------------|---------------|----------------|-----------|--------|
|    |            |           |     | Bare Strength [MPa] | Stabilized     |                |                      | L Direction   |                | W Direction   |                |           |        |
|    |            |           |     |                     | Strength [MPa] | Strength [MPa] |                      | Modulus [GPa] | Strength [MPa] | Modulus [GPa] | Strength [MPa] |           |        |
| 8. | AA5056-H39 | 3/16"     | 3.1 | 1.724               | 1.793          | 0.669          | 1.172                | 1.379         | 0.310          | 0.758         | 0.138          | Datasheet |        |
| 9. | AA5056-H39 | 1/8"      | 4.5 | 3.275               | 3.447          | 1.276          | 2.206                | 2.413         | 0.483          | 1.413         | 0.193          | Datasheet |        |

Figure 4.9: Honeycomb materials properties

| ID  | Material                              | Thickness (mm) | Young's Modulus<br>E <sub>1</sub> [GPa]<br>E <sub>2</sub> [GPa] | Shear Modulus G <sub>12</sub> [GPa] | Poisson's ratio ν <sub>12</sub> | Density ρ [kg/m <sup>3</sup> ] | Tensile Strength σ <sub>t</sub> [MPa] | Shear Strength τ <sub>t</sub> [MPa] | Thermal Expansion Coefficient [ppm/°C] | Ref.            | Use        | Remarks |
|-----|---------------------------------------|----------------|---|-------------------------------------|---------------------------------|--------------------------------|---------------------------------------|-------------------------------------|--|-----------------|------------|---------|
| 10. | RS-36 AFC49 M55JB UD 6K - 135g - 33%  | 0.125          | 279.0   | 3.0                                 | 0.272                           | 1689                           | 1005.0                                | 44.0                                | 0.06                                   | Test - Bercella | Face Sheet | B-Basis |
|     |                                       |                | 5.5   |                                     |                                 |                                | 12.0                                  |                                     | 33.0                                   |                 |            |         |
| 11. | RS-36 HS0704-A 40% T300 3K CAR199g PW | 0.200          | 48.0  | 2.64                                | 0.01                            | 1552                           | 495.0                                 | 69.6                                | 3.2                                    | Test - Bercella | Face Sheet | B-Basis |
|     |                                       |                | 48.0  |                                     |                                 |                                | 495.0                                 |                                     | 3.2                                    |                 |            |         |

Figure 4.10: Orthotropic materials properties

| ID                   | Ply ID | Material                              | Thickness [m] | Angle |
|----------------------|--------|---------------------------------------|---------------|-------|
| CFRP_Sandwich_10.4mm | 1      | RS-36 HS0704-A 40% T300 3K CAR199g PW | 0.0002        | 0     |
|                      | 2      | RS-36 AFC49 M55JB UD 6K - 135g - 33%  | 0.000125      | 0     |
|                      | 3      | RS-36 AFC49 M55JB UD 6K - 135g - 33%  | 0.000125      | 90    |
|                      | 4      | RS-36 AFC49 M55JB UD 6K - 135g - 33%  | 0.000125      | 0     |
|                      | 5      | RS-36 AFC49 M55JB UD 6K - 135g - 33%  | 0.000125      | 90    |
|                      | 6      | Honeycomb 5056 - 3/16" - 3.1          | 0.009         | 0     |
|                      | 7      | RS-36 AFC49 M55JB UD 6K - 135g - 33%  | 0.000125      | 90    |
|                      | 8      | RS-36 AFC49 M55JB UD 6K - 135g - 33%  | 0.000125      | 0     |
|                      | 9      | RS-36 AFC49 M55JB UD 6K - 135g - 33%  | 0.000125      | 90    |
|                      | 10     | RS-36 AFC49 M55JB UD 6K - 135g - 33%  | 0.000125      | 0     |
|                      | 11     | RS-36 HS0704-A 40% T300 3K CAR199g PW | 0.0002        | 0     |
| Al_Sandwich_40.6mm   | 1      | AA7075-T6                             | 0.0008        | 0,    |
|                      | 2      | Honeycomb 5056 - 1/8" - 4.5           | 0.039         | 0,    |
|                      | 3      | AA7075-T6                             | 0.0008        | 0     |
| Al_Sandwich_25mm     | 1      | AA7075-T6                             | 0.0005        | 0,    |
|                      | 2      | Honeycomb 5056 - 3/16" - 3.1          | 0.024         | 0,    |
|                      | 3      | AA7075-T6                             | 0.0005        | 0     |
| Al_Sandwich_20mm     | 1      | AA7075-T6                             | 0.0005        | 0,    |
|                      | 2      | Honeycomb 5056 - 3/16" - 3.1          | 0.019         | 0,    |
|                      | 3      | AA7075-T6                             | 0.0005        | 0     |
| Al_Sandwich_25mm     | 1      | AA7075-T6                             | 0.0005        | 0,    |
|                      | 2      | Honeycomb 5056 - 1/8" - 4.5           | 0.024         | 0,    |
|                      | 3      | AA7075-T6                             | 0.0005        | 0     |
| Al_Sandwich_20mm     | 1      | AA7075-T6                             | 0.0005        | 0,    |
|                      | 2      | AA7075-T7351                          | 0.019         | 0,    |
|                      | 3      | AA7075-T6                             | 0.0005        | 0     |
| Al_Sandwich_40.6mm   | 1      | AA7075-T6                             | 0.0008        | 0,    |
|                      | 2      | AA7075-T7351                          | 0.039         | 0,    |
|                      | 3      | AA7075-T6                             | 0.0008        | 0     |
| Al_Sandwich_25mm     | 1      | AA7075-T6                             | 0.0005        | 0,    |
|                      | 2      | AA7075-T7351                          | 0.024         | 0,    |
|                      | 3      | AA7075-T6                             | 0.0005        | 0     |

Figure 4.11: Composite materials list

## 4.2.2 Modal analysis and resonance search

The SM has undergone a modal analysis to evaluate the main modes of the S/C structure. The goal of the analysis was to identify the set of modes with effective mass higher than 5% of the total mass. The results of the modal analysis are computed for the first 55 modes of the S/C stand-alone, meaning that the Vibration Test Fixture (VTF) has been removed from the analysis. The analysis considered the S/C in hard-mounted boundary conditions. For modal extraction from 100 to 10k Hz, a new modal analysis has to be conducted, because the boundary conditions are different. In this case, the S/C will be hanged from above, simulating free-free configuration that will give different results. Furthermore, the SM has undergone a mechanical vibration test campaign. Among other tests, the spacecraft was subjected to a sine sweep low level test on a shaker from 10 to 2k Hz, in order to find the resonant points. During the test, the response of 64 triaxial accelerometers has been collected and correlated with the FEM analysis. As an example, the relevant results of the correlation are reported in 4.12, 4.13, 4.16, 4.14, 4.15 and 4.17. The plots display the values collected by accelerometers AC05 and AC38, that were mounted on the bottom and top plates, respectively. The correlation criteria are:

- The difference on the principal modes shall be less than 5% for frequency shifts.
- The difference on the principal modes shall be less than 20% for amplitude shifts.
- Only modes of the S/C with a mass fraction higher than 10% are correlated. These are:
  - The first mode in the Y direction at 28.8 Hz (test);
  - The first mode in the X direction at 30.6 Hz (test);
  - The first two modes in the Z direction at 78.0 Hz and 83.9 Hz (test);

## 4.2.3 Damping evaluation

The damping has been derived from the Frequency Response Functions (FRFs) of the mechanical vibration test campaign. The damping has been hypothesized as viscous and computed through the Half-power Method. In this method, the peak is qualitatively selected from the FRF values of each measurement where the peak of a global mode is evident and well isolated, providing both amplitude and frequency ( $f_n$ ). The -3dB line is derived from the peak value reduced of 3dB, and intersects the curve in two points, at frequencies  $f_1$  and  $f_2$ , as shown in 4.18.



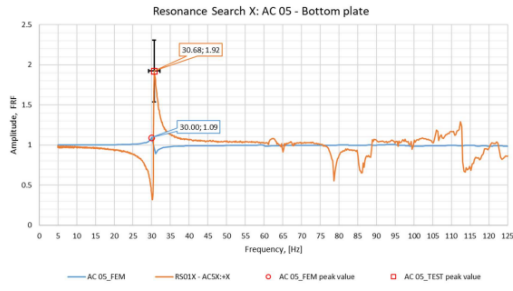


Figure 4.12: Channel 5, bottom plate, x direction

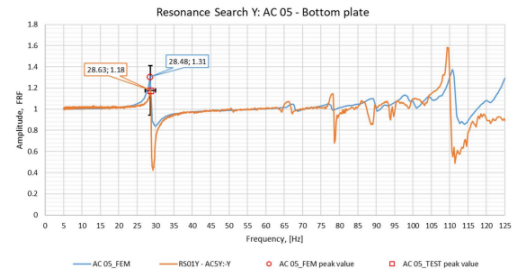


Figure 4.13: Channel 5, bottom plate, y direction

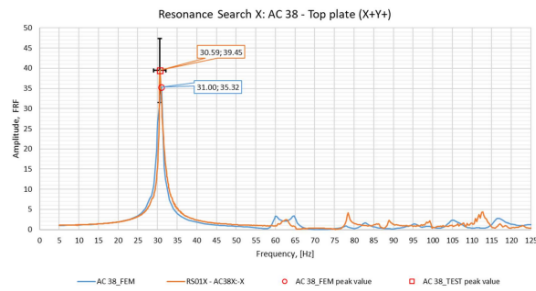


Figure 4.14: Channel 38, top plate, x direction

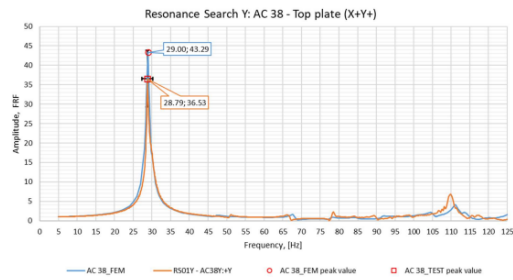


Figure 4.15: Channel 38, top plate, y direction

The damping value is evaluated by means of the following formula:

$$\zeta = \frac{f_1 - f_2}{2f_n} \quad (4.1)$$

### 4.3 Experimental set up

In this section the potential experimental set up is described. It has been tailored for a shock test that will be performed on the SM. A graphical representation of it is depicted in 4.19 and 4.20. The aim of the test is to measure the SRS response, that are induced by the stage's separation of the launcher during flight, in the relevant locations of the spacecraft. The test will be conducted in the following configuration:

- The SM will be hoisted on a crane, representing free-free boundary conditions.
- The SM will be connected to a dummy launcher, representing the mechanical properties of the last stage of the launcher, through the Launcher Vehicle

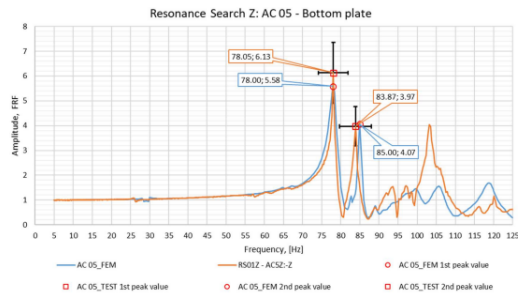


Figure 4.16: Channel 5, bottom plate, z direction

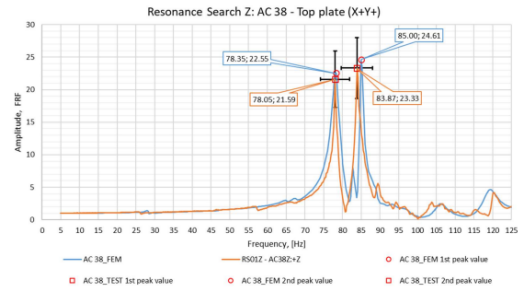


Figure 4.17: Channel 38, top plate, z direction

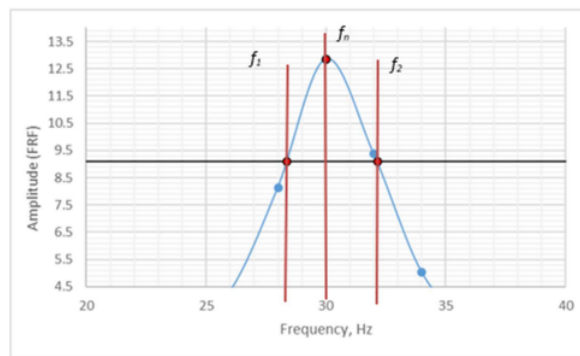


Figure 4.18: Half-Power Damping Evaluation Method

Adapter (LVA).

- The LVA will be connected to the spacecraft interface with the use of a Marman Clampband, which is held closed by pre-loaded screws that apply pressure to secure the structure.
- Pyrotechnic devices will be positioned at the bottom interface of the spacecraft, near the screws.

When the pyrotechnic devices are activated, the screws break, releasing the clampband and allowing the LVA and dummy launcher to separate from the spacecraft.

Ensuring that an experimental setup accurately replicates real shock phenomena, especially in terms of boundary conditions (BCs), presents significant technical challenges. In shock testing for space systems, the aim is to replicate the forces and vibrations that occur during actual events, such as stage separation in flight. However, achieving this fidelity in a lab setting requires careful control over the setup's boundary conditions, which often differ from the real operational environment. Here are some specific technical challenges:

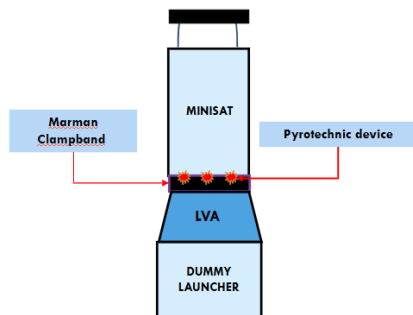


Figure 4.19: Schematization of a possible experimental setup inspired by VESTA

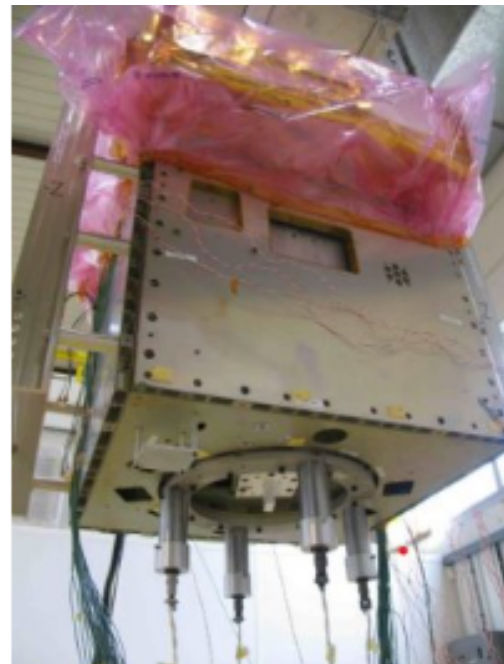


Figure 4.20: Real experimental setup for pyrotechnic shock testing

- In an actual space environment, the spacecraft and launcher are essentially "free" in space, meaning they aren't rigidly fixed to anything. This condition is simulated in the lab by suspending the Structure Model (SM) on a crane, intending to minimize the influence of external constraints. However, true free-free conditions are hard to achieve. Any residual interaction with the suspension (e.g., vibrations or slight oscillations) may alter the shock response, potentially reducing the accuracy of the test results.
- The dummy launcher and Launcher Vehicle Adapter (LVA) are meant to represent the mechanical properties of the actual launcher stage. If these components do not accurately mimic the stiffness, damping, and mass distribution of the real launcher, the shock response could differ. Variances in these properties could alter the natural frequencies and modes of vibration, which play a critical role in determining the Shock Response Spectrum (SRS) observed at different points on the spacecraft.
- The Marman Clampband is designed to release the spacecraft by breaking screws using pyrotechnic devices. In the lab, replicating the exact dynamics of this release can be challenging, as it involves complex, non-linear interactions that influence the shock waves transmitted through the structure. If

the timing or energy release from the pyrotechnics differs even slightly from actual conditions, the test setup might not replicate the precise shock levels experienced in flight.

- Even small differences in material damping between the dummy components and actual flight components can influence the shock response. In a controlled lab environment, damping characteristics might not fully match those of the actual system, especially if real materials age differently under the unique stresses of the space environment.
- Suspension methods or test equipment in contact with the SM can introduce unintended constraints that absorb or reflect shock waves differently than in flight.

### 4.3.1 Instrumentation

The structure will be equipped with triaxial piezo-electric accelerometers (on critical equipment and structure locations) suitable to measure the shock event in the bandwidth 100-10k Hz. The accelerometers should be triaxial to measure the shock levels in all three axes and not only in the main excitation direction. The accelerometers situated near the shock source should be bolted to the structure. Among the other mounting techniques, the direct coupling, stud mounted to a very smooth surface, generally yields the highest transmissibility, mechanical resonant frequency and, therefore, the broadest usable frequency range. For the accelerometers located in the upper part of the structure, adhesive mounting is recommended, since vibrations are damped and there is less risk of detachment of sensors. About 30 sensors have been chosen to cover all the location of interest. Some examples are shown in 4.21, 4.22 and 4.23. The registration shall be delivered as time history and SRS graphical representations, each of them plotting acceleration, velocity, and position.

### 4.3.2 Input and tolerances

The input values to be applied to the bottom interface of the spacecraft, where the shock source is located, are shown in 4.2 and 4.24. The input is represented in form of SRS. A SRS is a powerful tool used to assess the shock response of a physical structure to a transient input shock. It provides a graphical representation of the maximum accelerations response at each frequency point. Each point on the graph represents the maximum acceleration response of an SDOF system, each one with a different natural frequency. Regarding the tolerances, the lower test tolerance of -3 dB is a minimum requirement to ensure coherence with the qualification margin.

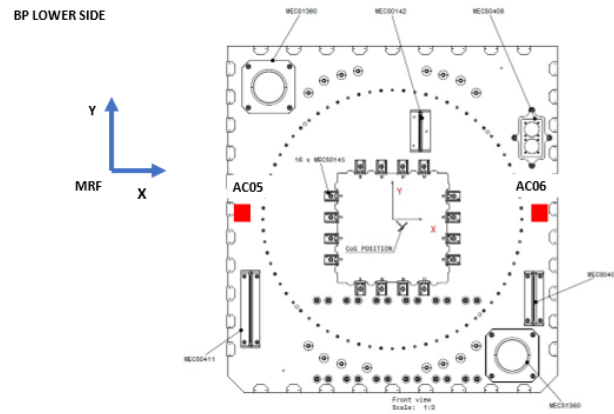


Figure 4.21: Instrumentation plan, Bottom Plate, lower side

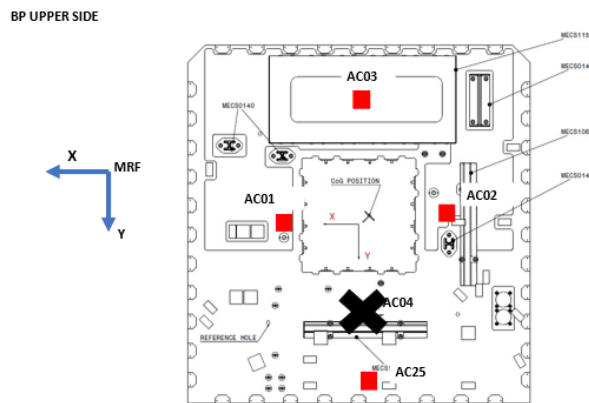


Figure 4.22: Instrumentation plan, Bottom Plate, upper side

Whereas the upper test tolerance of +6 dB acts as the upper bound to reduce the risk of failure, as displayed in 4.25.

### 4.3.3 Pass/Fail criteria

The Pass/Fail criteria after vibration test are:

- All the measurements are properly acquired and stored
  - The initial slopes of both the positive and negative SRS curves shall have an overall trend of 6 to 1 dB/octave. The corresponding slope equations for sine and shock are:

$$N = \frac{\log \frac{y_2}{y_1}}{\log \frac{f_2}{f_1}} \quad (4.2)$$

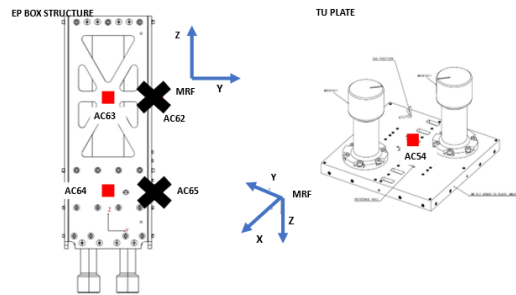


Figure 4.23: Instrumentation plan, EP box

| Frequency [Hz] | Value [g] |
|----------------|-----------|
| 100            | 56        |
| 1600           | 2820      |
| 10000          | 2820      |

Table 4.2: Shock load input values (Q=10)

The dB/octave slope is:

$$\Delta dB = 20N \log 2 \quad (4.3)$$

The initial slope (100 – 1600 Hz) of the shock test levels indicated in Figure is acceptable as it measures 8,5 dB/octave.

- The velocity time history should oscillate in a stable manner about the zero baselines
- The shock loads are correctly applied within the tolerances (see Figure)
- No detectable cracks with the naked eye on the test item parts will be observed

## 4.4 Shock prediction using Empirical method

*The Unified Approach And Practical Implementation Of Attenuation Rules For Typical Spacecraft Shock Generated Environments*, explained thoroughly in [132], is a common technique that allows to determine the acceleration at the mounting points of most critical components. This method traces the path of the shock load that propagates from its source (or S/C interface), where the acceleration is known, to the locations of the critical units. An example of a load path is shown in 4.26. The attenuation factor is computed for each section of the path. It depends mainly on distance, angle, type of structure (e.g., honeycomb, skin-frame,

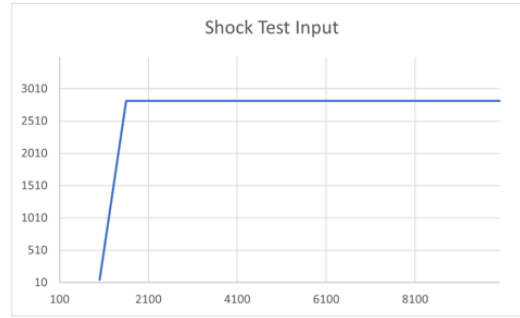


Figure 4.24: Shock load input plot

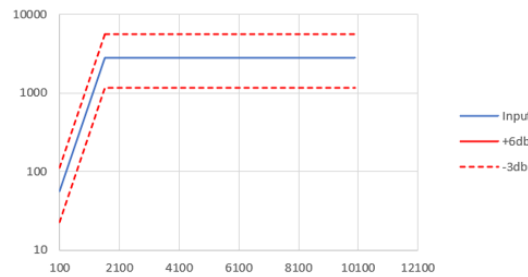


Figure 4.25: Test tolerances of +6/-3 dB

monocoque, etc.) and presence of joints. These data have been collected mainly during an experimental activity performed several years ago.

More in details, Junction Attenuation Factor  $Att_{Joint(axial,radial)}$  and Distance Attenuation Factor  $Att_{Distance(axial,radial)}$  are calculated from the procedure. In order to calculate the attenuation over a joint, the section orientation factors  $e$  and  $f$  are introduced (where  $\alpha_j$  is the angle between section  $i$  and section  $(i + 1)$ ):

$$f_j = \frac{1 + \cos^2(\alpha_j)}{2} \quad (4.4)$$

for axial direction and

$$e_j = \frac{1 + \sin^2(\alpha_j)}{2} \quad (4.5)$$

for radial direction. Then we have

$$Att_{Joint}^j(axial) = 1 - r_{ax,j} * \frac{K_{joint}}{20} \quad (4.6)$$

and

$$Att_{Joint}^j(radial) = 1 - r_{rad,j} * \frac{K_{joint}}{20} \quad (4.7)$$

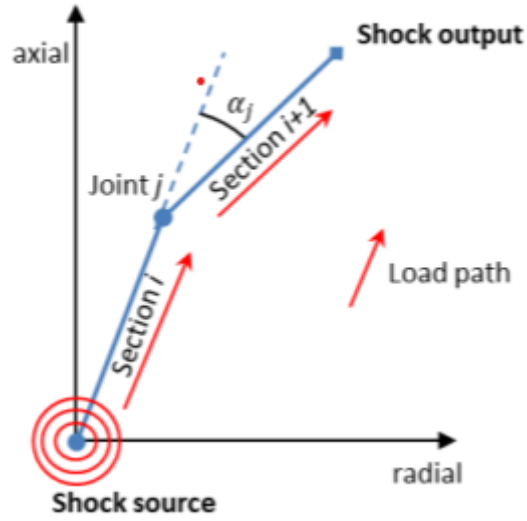


Figure 4.26: Load path example

with

$$r_{ax,j} = \frac{e_j}{f_j} \quad (4.8)$$

$$r_{rad,j} = \frac{f_j}{e_j} \quad (4.9)$$

The axial/radial total junction attenuation factors  $Att_{Joint}(axial)$  and  $Att_{Joint}(radial)$  are the product of all single junction attenuation factors.  $K_{Joint}$  is a factor that depends on 3 different types of joint configuration, as shown in 4.27. For distance attenuation, the formulas are the following

$$Att_{Distance}^i(axial) = e^{-e_i * L_i} \quad (4.10)$$

for axial direction and

$$Att_{Distance}^i(radial) = e^{-f_i * L_i} \quad (4.11)$$

for radial direction. With

$$e_i = \frac{1 + \sin^2 \alpha_i}{2} \quad (4.12)$$

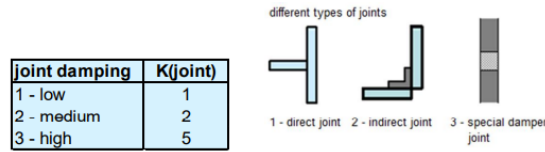
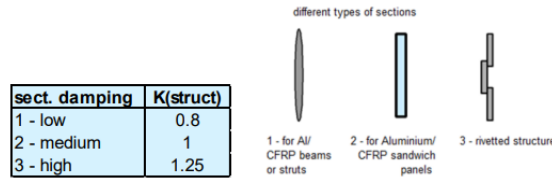
and

$$f_i = \frac{1 + \cos^2 \alpha_i}{2} \quad (4.13)$$

Moreover,

$$L_i = l_i * K_{Struct} \quad (4.14)$$



Figure 4.27:  $K_{Joint}$  definitionFigure 4.28:  $K_{Struct}$  definition

is the adjusted length calculated in order to consider different types of sections influencing the section attenuation factors with the help of an additional factor  $K_{struct}$ , which depends from the structural characteristic of the section, as in 4.28. Again, the axial/radial total distance attenuation factors  $Att_{Distance}(axial)$  and  $Att_{Distance}(radial)$  are the product of all single distance attenuation factors.

Finally, two total attenuation factors are defined:

$$Att(axial) = Att_{Joint}(axial) * Att_{Distance}(axial) \quad (4.15)$$

and

$$Att(radial) = Att_{Joint}(radial) * Att_{Distance}(radial) \quad (4.16)$$

The attenuation should be scaled to their input specification. This last step requires the knowledge of the nature of shock input to the spacecraft (e.g. axial input, radial input or balanced axial/radial input) provided by the launcher authority. Therefore, the shock output results from a multiplication between attenuation factor and shock input.

- **Case of shock specification defined for each direction axial and radial** (e.g., Ariane 5 HSS1 separation event, with 2 specifications provided by the launcher authority):

$$\text{Shock output} = \max(\text{SPEC}(\alpha \text{ axial}) \times Att(axial), \text{SPEC}(radial) \times Att(radial)) \quad (4.17)$$

- **Case of balanced input axial/radial to the spacecraft** (case of lack of knowledge on the nature of the shock input, e.g., typical launcher separation event):

$$\text{Shock output} = \max(\text{SPEC}(envelope) \times Att(axial), \text{SPEC}(envelope) \times Att(radial)) \quad (4.18)$$

- **Case of shock specification dominated by axial input to the spacecraft** (e.g., VEGA HSS separation, or point source excitation):

$$\text{Shock output} = \text{SPEC(axial)} \times \text{Att(axial)} \quad (4.19)$$

- **Case of shock specification dominated by radial input to the spacecraft** (e.g., Clampband):

$$\text{Shock output} = \text{SPEC(radial)} \times \text{Att(radial)} \quad (4.20)$$

However, it must be stressed that the procedure does not considers a number of parameters, e.g., material and thickness of the panels, so that it often leads to inaccurate results. It follows that alternative techniques are needed.

### In a synthesis

- Exploration of SITAEL's application of the V-Model in spacecraft development, focusing on the systematic verification and validation processes.
- Analysis of shock testing methods in industry and their issues, emphasizing the rigorous qualification tests required for spacecraft components to withstand shock loads.
- Detailed description of the Multi-Application Minisatellite project Structural Model (SM) as a case study for shock response testing and structural integrity verification.
- Outline of shock test specifications, including the experimental setup, instrumentation, input conditions, and pass/fail criteria developed to guide future testing on the Minisatellite SM.
- Overview of empirical methods traditionally used in industry to estimate shock loads, highlighting the conservative assumptions about shock attenuation that often result in overdesign and increased costs.
- Introduction of an improved predictive shock model using modal decomposition and transfer function analysis, offering more accurate shock load predictions to enable optimized satellite design.

# Chapter 5

## Shock Response Prediction in Mechanical Structures

### Contents

|       |   |     |
|-------|---|-----|
| 5.1   | R-FRFs and Shock Transmissibility . . . . .               | 101 |
| 5.2   | Application of the method on simple systems . . . . .     | 103 |
| 5.2.1 | 2-DOF System . . . . .                                    | 103 |
| 5.3   | ShockSat Case Study . . . . .                             | 107 |
| 5.3.1 | Extrapolation of Modal Data and computation of FRFs . . . | 107 |
|       | Analytical FRF . . . . .                                  | 107 |
|       | Experimental FRF . . . . .                                | 108 |
|       | FRF Comparison . . . . .                                  | 113 |
| 5.3.2 | Shock Transmissibility . . . . .                          | 115 |
| 5.3.3 | Input identification . . . . .                            | 117 |
| 5.3.4 | Shock Response Calculation . . . . .                      | 118 |
| 5.4   | Shock through composites . . . . .                        | 121 |
| 5.4.1 | Comparison of FEM and MUL2 . . . . .                      | 123 |
| 5.4.2 | Aluminium Isotropic Plate . . . . .                       | 124 |
| 5.4.3 | Composite Orthotropic Plate . . . . .                     | 125 |

In the final chapter, we present the development and preliminary application of the shock prediction methodology. The chapter begins with a theoretical explanation of the method, followed by an initial application to a simple 2-DOF mass-spring-damper system. Here, an input SRS is synthesised using the three

methods discussed in previous chapters, and the system response is evaluated. Additional analyses were conducted on other configurations, including a single plate and two orthogonal plates, to explore the methodology's applicability further. Furthermore, using the same methodology, an analysis of shock propagation through composite materials was conducted to evaluate its potential for complex material structures. Due to the absence of experimental data, however, validation of these results remains pending, despite comparisons with commercial software, which provided no absolute confirmation of accuracy. Subsequently, we extended the application to NASA's open-source ShockSat platform, which includes a FEM and provides valuable test data, including both modal (hammer test) and shock (pyroshock test) results. ShockSat serves as an essential reference point, supporting the refinement of this methodology, which is still undergoing validation. Upon validation, the ultimate goal will be to apply the method to the Multi-Application Minisatellite and validate it with pyroshock tests conducted at SITAEL, as represented in the block diagram 5.1.

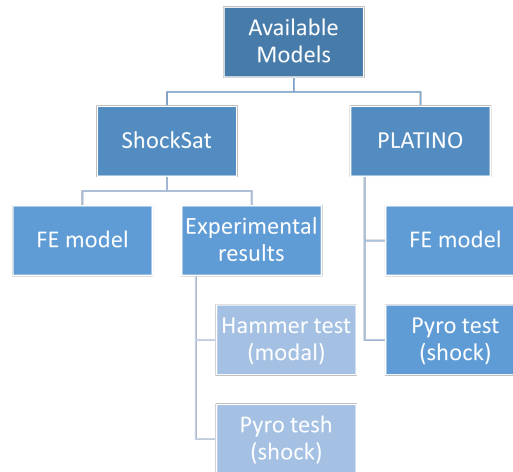


Figure 5.1: Block Diagram of the roadmap for the validation of the methodology

## 5.1 R-FRFs and Shock Transmissibility

To address the challenges associated with measuring excitation forces directly in real-world applications, [134–137] used Response-based Frequency Response Functions (R-FRFs) as an alternative to traditional FRFs. Unlike standard FRFs, which require both excitation forces and responses, R-FRFs are derived solely from structural responses. As a subset of Transmissibility Functions (TFs), they bypass the need for force measurement and rely only on the coordinates where forces act,

offering significant advantages in applications where force measurements are impractical. R-FRFs provide additional insights by introducing poles and modal information that correspond to conditions where certain DOFs are virtually constrained. This virtual constraint introduces supplementary poles in the R-FRF, enhancing the local modal information without altering the physical boundary conditions of the structure. By leveraging this property, we gain an enriched set of data specific to portions of the structure, which is invaluable for localized diagnosis and dynamic behaviour analysis, particularly in shock load contexts. The poles derived from R-FRFs reflect how the structure would behave under these virtual constraints, thus offering critical insights into how shock loads propagate and interact with different structural areas. In this chapter, R-FRFs are employed to determine shock transmissibility, as they are especially effective in local modal analysis and provide indicators of load propagation through specific structural regions. We consider a linear, time-invariant, damped vibrating system having  $N$  degrees of freedom (dofs), for which the well-known input–output relationship in the Laplace domain  $s$ , from rest initial conditions, is:

$$B(s)X(s) = F(s) \quad (5.1)$$

The dynamic stiffness matrix  $B(s)$ , the displacement  $X(s)$ , and the force  $F(s)$  vectors can be partitioned as:

$$\begin{bmatrix} B_{11}(s) & B_{12}(s) \\ B_{21}(s) & B_{22}(s) \end{bmatrix} \begin{bmatrix} Z(s) \\ Y(s) \end{bmatrix} = \begin{bmatrix} Q(s) \\ 0 \end{bmatrix} \quad (5.2)$$

where  $Z(s)$  is the displacement vector that includes the  $n$  output responses dofs in which the input forces are applied. Let's consider the transfer matrix as:

$$H(s) = B^{-1}(s) \quad (5.3)$$

It can be decomposed with the modal partial fraction decomposition:

$$H(s) = \sum_{r=1}^{N_p} \left( \frac{\psi_r L_r^T}{s - \lambda_r} + \frac{\psi_r^* L_r^H}{s - \lambda_r^*} \right) \quad (5.4)$$

where  $(.)^H$  indicates Hermitian transposition,  $(.)^*$  denotes complex conjugation,  $N_p$  is the number of modes,  $\psi_r$  are the mode shape vectors, and  $L_r$  are the modal participation vectors. In addition,  $\lambda_r$  are the complex-valued roots, appearing in complex conjugate pairs:

$$\lambda_r = -\zeta_r \omega_r \pm i \omega_r \sqrt{1 - \zeta_r^2} \quad (5.5)$$

with  $\omega_{ur}$  being the undamped natural frequency and  $\zeta_r$  the damping ratio. The defined transfer function establishes a relationship between the external force and

the resulting displacements. Since we will be computing the shock response using SRS, it may be beneficial to make this term dimensionless, thereby obtaining the system's global transmissibility. In general, a transmissibility is defined as the transfer function that relates the displacements (or velocities, accelerations) at the output and input locations. Specifically, R-FRFs, indicated here as  $T(i\omega)$ , can be calculated by using partitions of the FRF matrix throughout the following relation:

$$T(i\omega) = H_{21}(i\omega)H_{11}^{-1}(i\omega) \quad (5.6)$$

where  $H_{11}$  and  $H_{21}$  indicate the corresponding partitions of the FRF matrix  $H(i\omega) = B^{-1}(i\omega)$ . R-FRFs can also be obtained using modal decomposition. The global transmissibility can now be used to get the shock transmissibility, which ECSS [131] defines as:

$$\sqrt{T(\omega)} \leq T_{\text{shock}}(\omega) \leq \sqrt{2T(\omega)} \quad (5.7)$$

Shock transmissibility, especially at frequencies below 2000 Hz, is lower than the transmissibility obtained by the modal test. The latter is usually performed on a thick resonant plate with a hammer impact as an impulse generator. Therefore, the cross-correlation between all interface points is stronger than it would be during a pyrotechnic shock, and the shock transmissibility at low frequency can thus be overestimated. The shock transmissibility is directly used to compute the system's response to a shock load, where the input shock load is represented in the form of an SRS:

$$SRS_{\text{out}} = T_{\text{shock}}(\omega)SRS_{\text{in}} \quad (5.8)$$

The proposed methodology offers an alternative to existing approaches. Numerical methods like FEM-SEA are complex and time-consuming, requiring the development of two entirely separate models and the creation of virtual modes to link them. In contrast, calculating shock transmissibility from the modal parameters is faster, yet still reliable and less conservative than the similarity-heritage-extrapolation methods commonly used in industry.

## 5.2 Application of the method on simple systems

### 5.2.1 2-DOF System

In this section the method has been applied on a 2 degree-of-freedom system 5.2. The FRF obtained by modal partial fraction decomposition has been compared with the FRF obtained by other two methods. The former was obtained by analytical computation, using the dynamic stiffness; the latter was obtained from a

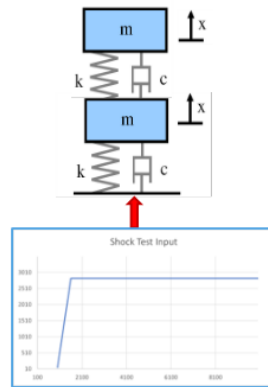


Figure 5.2: Ground acceleration applied on a 2 dof mass-spring-damper system

commercial software. We can observe how the three methods are perfectly overlapped in 5.3,5.4,5.5,5.6.

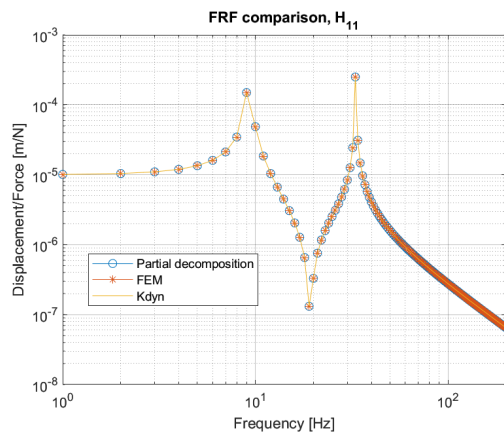


Figure 5.3: Frequency Response Function,  $H_{11}$

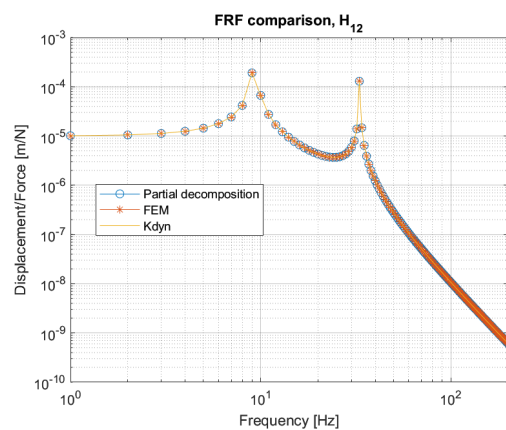


Figure 5.4: Frequency Response Function,  $H_{12}$

After that, an input was chosen from a real pyroshock test. In 5.7 the derived SRS input specification is plotted. The obtained response is shown in 5.8 and 5.9. The explanation of the 2 methodologies is explained in the following section.



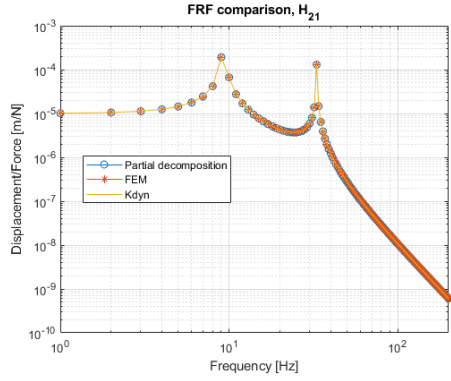


Figure 5.5: Frequency Response Function, H21

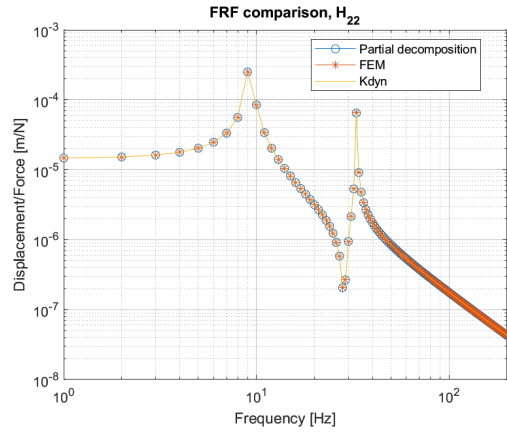


Figure 5.6: Frequency Response Function, H22

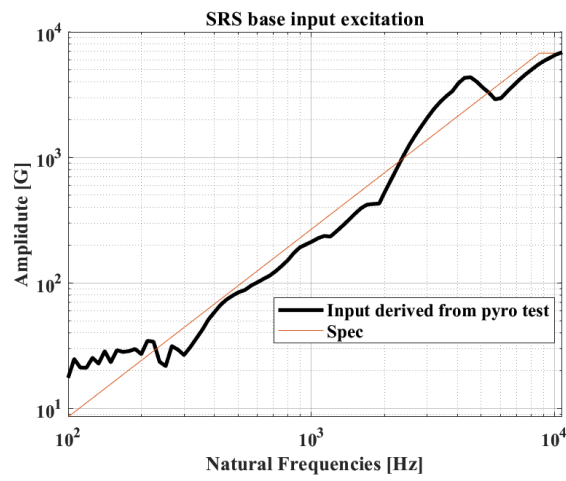


Figure 5.7

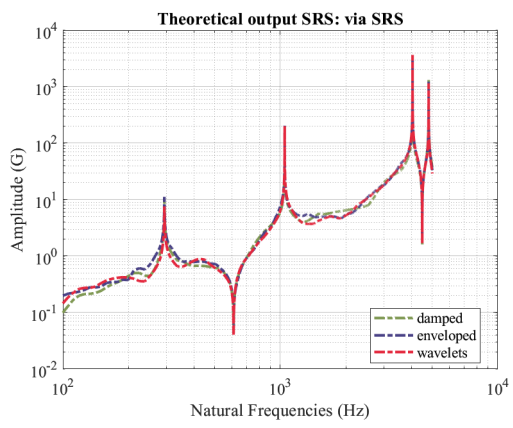


Figure 5.8: Theoretical output via SRS

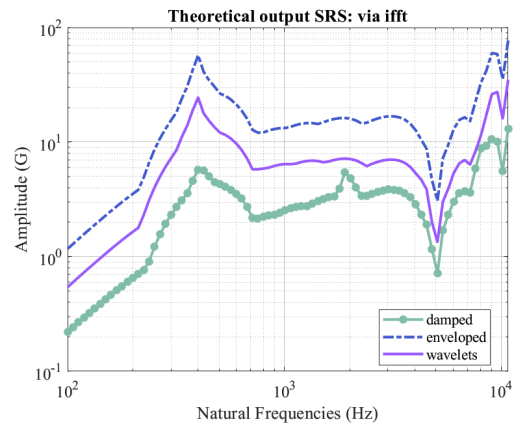


Figure 5.9: Theoretical output via Inverse Fast-Fourier Transform

## 5.3 ShockSat Case Study

NASA's ShockSat has been used as open-source case study. This project is designed to tackle the persistent challenges linked to pyroshock sources used in launch vehicles and spacecraft. While pyroshock systems are highly reliable, ensuring that separation mechanisms function seamlessly, this reliability comes with a downside: shock waves travel through the structure and can potentially harm sensitive electronics. Despite advances in many areas of spacecraft design, shock propagation prediction remains behind, with outdated semi-empirical methods from the 1970 still being used, even though numerous studies have proven them to be insufficient. Newer methods are either proprietary or come with uncertainties in data and models, making it difficult to trust the results. ShockSat aims to change that by offering data that can genuinely push the field forward in the public domain. The project focuses on creating a mobile test-bed to develop improved shock prediction methodologies and conducting a broad range of tests to build a robust database. ShockSat1 features a straightforward architecture with standard spacecraft manufacturing techniques like bolted joints, material mismatches, and multiple shock sources. Its ultimate goal is to provide unquestionable input data, engage the community with benchmark problems, and push the boundaries of current methods. ShockSat1 was designed with a simple sheet-metal structure that incorporates key shock transmission features, making it an ideal test-bed for shock studies, as in 5.10. The structure is free from any proprietary or secret restrictions, allowing for open access and community engagement. A well-correlated Finite Element Model (FEM) was developed alongside a real physical model, where hammer test data was used for characterization and correlation with the FEM modal analysis, as shown in 5.10. Additionally, ShockSat1 underwent shock tests with various pyroshock sources, including point-source tests using NSD and line-source tests with frangible joints, providing comprehensive data to validate the model's performance and refine shock prediction methodologies.

### 5.3.1 Extrapolation of Modal Data and computation of FRFs

#### Analytical FRF

To explore the dynamic behaviour of the ShockSat structure, a modal analysis was performed using NASTRAN on the FEM of ShockSat within the frequency range from 0 to 2000 Hz. The analysis provided a *.f06* file containing eigenvalues and eigenvectors, as shown in 5.12 and 5.13, which represent the natural frequencies and mode shapes of the system. This data was subsequently processed in MATLAB using a custom code, detailed in Appendix A, to synthesize the Frequency Response Function (FRF) through the modal partial fraction summation decom-

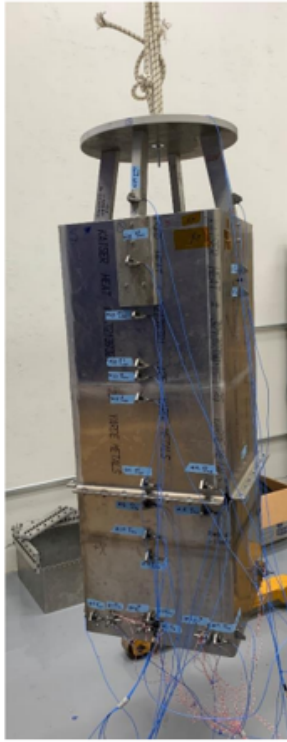


Figure 5.10: ShockSat Physical model

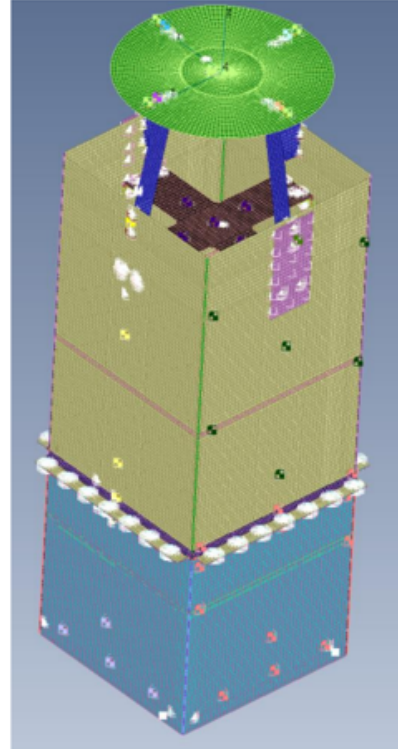


Figure 5.11: ShockSat FEM model

position approach. In this synthesis, a viscous damping ratio of 0.025 (equivalent to  $Q = 20$ ) was applied to the poles, formulated as:

$$\lambda_{1,2} = -\zeta\omega_n \pm i\sqrt{1 - \zeta^2}\omega_n$$

where  $\zeta$  denotes the damping ratio and  $\omega_n$  is the undamped natural frequency. A scaling factor,  $Q_r(j) = \frac{1}{2\omega_n(j)}$ , was applied to achieve unity modal mass normalisation. This approach provided the FRF in terms of acceleration-to-force ratio ( $g/N$ ), thus enabling a direct comparison with experimentally derived FRFs.

### Experimental FRF

On the experimental side, a characterization test was conducted on ShockSat using a hammer test in the x, y, and z directions, as in 5.14 and 5.15. The input force (an impulse) and the output accelerations recorded from accelerometers at various points on the satellite were used to compute the experimental FRFs through a system identification algorithm. 5.17, 5.16 and 5.18 show the configuration of some accelerometers, namely on top plate, +X panel and +y panel. Subsequently,

| MODE NO. | EXTRACTION ORDER | EIGENVALUE    | REAL EIGENVALUES |              | GENERALIZED MASS | GENERALIZED STIFFNESS |
|----------|------------------|---------------|------------------|--------------|------------------|-----------------------|
|          |                  |               | RADIANS          | CYCLES       |                  |                       |
| 1        | 1                | -2.379536E-05 | 4.878049E-03     | 7.763656E-04 | 1.000000E+00     | -2.379536E-05         |
| 2        | 2                | -1.626360E-05 | 4.032816E-03     | 6.418426E-04 | 1.000000E+00     | -1.626360E-05         |
| 3        | 3                | -1.365698E-05 | 3.695535E-03     | 5.881626E-04 | 1.000000E+00     | -1.365698E-05         |
| 4        | 4                | -1.146903E-05 | 3.386595E-03     | 5.389934E-04 | 1.000000E+00     | -1.146903E-05         |
| 5        | 5                | -6.756312E-06 | 2.599291E-03     | 4.136900E-04 | 1.000000E+00     | -6.756312E-06         |
| 6        | 6                | -3.877359E-06 | 1.969101E-03     | 3.133922E-04 | 1.000000E+00     | -3.877359E-06         |
| 7        | 7                | 1.188297E+05  | 3.447168E+02     | 5.486339E+01 | 1.000000E+00     | 1.188297E+05          |
| 8        | 8                | 2.133865E+05  | 4.619378E+02     | 7.351968E+01 | 1.000000E+00     | 2.133865E+05          |
| 9        | 9                | 2.156185E+05  | 4.643474E+02     | 7.390318E+01 | 1.000000E+00     | 2.156185E+05          |
| 10       | 10               | 3.076169E+05  | 5.546322E+02     | 8.827245E+01 | 1.000000E+00     | 3.076169E+05          |
| 11       | 11               | 4.133771E+05  | 6.429441E+02     | 1.023277E+02 | 1.000000E+00     | 4.133771E+05          |
| 12       | 12               | 5.088078E+05  | 7.133077E+02     | 1.135264E+02 | 1.000000E+00     | 5.088078E+05          |
| 13       | 13               | 5.411807E+05  | 7.356499E+02     | 1.170823E+02 | 1.000000E+00     | 5.411807E+05          |
| 14       | 14               | 5.876556E+05  | 7.665870E+02     | 1.220061E+02 | 1.000000E+00     | 5.876556E+05          |
| 15       | 15               | 8.388091E+05  | 9.158652E+02     | 1.457645E+02 | 1.000000E+00     | 8.388091E+05          |
| 16       | 16               | 9.106468E+05  | 9.542781E+02     | 1.518781E+02 | 1.000000E+00     | 9.106468E+05          |
| 17       | 17               | 9.148332E+05  | 9.564692E+02     | 1.522268E+02 | 1.000000E+00     | 9.148332E+05          |
| 18       | 18               | 1.017175E+06  | 1.008551E+03     | 1.605159E+02 | 1.000000E+00     | 1.017175E+06          |
| 19       | 19               | 1.111061E+06  | 1.054069E+03     | 1.677602E+02 | 1.000000E+00     | 1.111061E+06          |
| 20       | 20               | 1.123552E+06  | 1.059977E+03     | 1.687006E+02 | 1.000000E+00     | 1.123552E+06          |
| 21       | 21               | 1.320471E+06  | 1.149118E+03     | 1.828878E+02 | 1.000000E+00     | 1.320471E+06          |
| 22       | 22               | 1.344461E+06  | 1.159509E+03     | 1.845416E+02 | 1.000000E+00     | 1.344461E+06          |
| 23       | 23               | 1.356465E+06  | 1.164674E+03     | 1.853636E+02 | 1.000000E+00     | 1.356465E+06          |
| 24       | 24               | 1.417700E+06  | 1.190672E+03     | 1.895013E+02 | 1.000000E+00     | 1.417700E+06          |
| 25       | 25               | 1.453333E+06  | 1.205542E+03     | 1.918680E+02 | 1.000000E+00     | 1.453333E+06          |
| 26       | 26               | 1.456555E+06  | 1.206335E+03     | 1.920033E+02 | 1.000000E+00     | 1.456555E+06          |

Figure 5.12: Eigenvalues on the .f06 NASTRAN file

both the analytically synthesised and experimentally derived FRFs were compared, though further investigation is ongoing to finalize and validate these results.

EIGENVALUE = -2.379536E-05  
CYCLES = 7.763656E-04

REAL EIGENVECTOR NO. 1

| POINT ID. | TYPE | T1            | T2            | T3            | R1           | R2           | R3            |
|-----------|------|---------------|---------------|---------------|--------------|--------------|---------------|
| 2         | G    | 6.055483E-02  | -8.043617E-02 | -8.115526E-03 | 1.283956E-02 | 3.941686E-02 | -5.332343E-01 |
| 3         | G    | 5.858836E-02  | -8.137915E-02 | -8.232581E-03 | 1.283956E-02 | 3.941686E-02 | -5.332343E-01 |
| 1021515   | G    | 7.734913E-02  | -6.797018E-02 | -6.789652E-03 | 1.283957E-02 | 3.941685E-02 | -5.332343E-01 |
| 9900001   | G    | -1.152724E-01 | -9.466832E-02 | -1.340125E-02 | 1.283956E-02 | 3.941685E-02 | -5.332343E-01 |
| 9900002   | G    | -6.279122E-02 | -9.464550E-02 | -1.213589E-02 | 1.283956E-02 | 3.941685E-02 | -5.332343E-01 |
| 9900003   | G    | 3.948242E-02  | -9.460636E-02 | -9.670386E-03 | 1.283956E-02 | 3.941685E-02 | -5.332343E-01 |
| 9900004   | G    | 9.184350E-02  | 1.416656E-01  | 9.055696E-03  | 1.283957E-02 | 3.941685E-02 | -5.332343E-01 |
| 9900005   | G    | -1.305720E-01 | 1.746318E-01  | 6.137102E-03  | 1.283956E-02 | 3.941684E-02 | -5.332343E-01 |
| 9900006   | G    | -1.772841E-01 | 1.332258E-01  | 1.951598E-03  | 1.283955E-02 | 3.941685E-02 | -5.332343E-01 |
| 9900007   | G    | -1.495733E-01 | -8.098068E-02 | -1.321538E-02 | 1.283956E-02 | 3.941685E-02 | -5.332343E-01 |
| 9900008   | G    | -4.886493E-02 | -8.096111E-02 | -1.078901E-02 | 1.283956E-02 | 3.941684E-02 | -5.332343E-01 |
| 9900009   | G    | 5.366430E-02  | -8.096111E-02 | -8.320244E-03 | 1.283956E-02 | 3.941685E-02 | -5.332343E-01 |
| 9900010   | G    | 7.823928E-02  | -6.743653E-02 | -6.728770E-03 | 1.283957E-02 | 3.941685E-02 | -5.332343E-01 |
| 9900011   | G    | 6.456497E-02  | 1.612311E-01  | 9.845157E-03  | 1.283956E-02 | 3.941684E-02 | -5.332343E-01 |
| 9900012   | G    | -1.641204E-01 | -5.464306E-02 | -1.161877E-02 | 1.283954E-02 | 3.941685E-02 | -5.332343E-01 |
| 9900013   | G    | -3.948211E-02 | -8.375274E-02 | -1.076944E-02 | 1.283956E-02 | 3.941685E-02 | -5.332343E-01 |
| 9900014   | G    | -3.697914E-02 | -8.456805E-02 | -1.076944E-02 | 1.283956E-02 | 3.941684E-02 | -5.332343E-01 |
| 9900015   | G    | -4.022805E-02 | -7.157239E-02 | -9.887028E-03 | 1.283956E-02 | 3.941685E-02 | -5.332343E-01 |
| 9900016   | G    | -3.233666E-02 | -8.577145E-02 | -1.074661E-02 | 1.283956E-02 | 3.941685E-02 | -5.332343E-01 |

Figure 5.13: Eigenvectors on the .f06 NASTRAN file

Channel 1 Response Data, Filter = [10,20000]

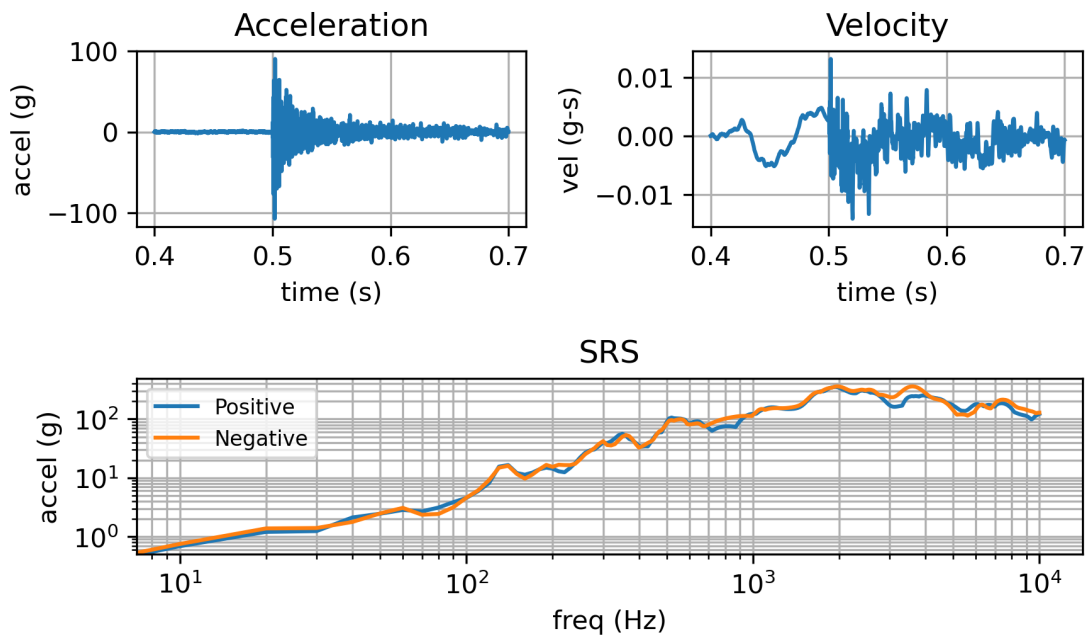


Figure 5.14: SRS experimental output, channel 1

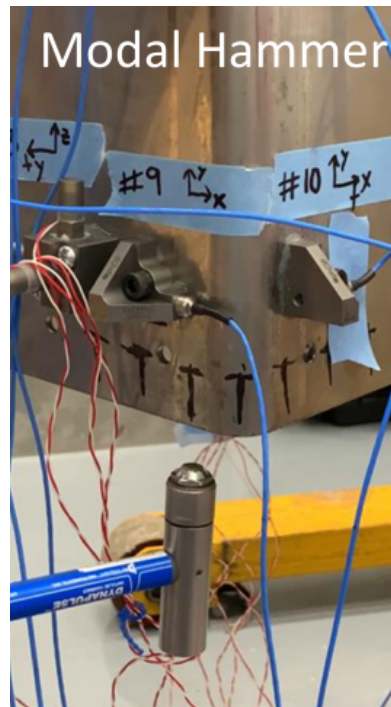


Figure 5.15: Hammer Test on Shocksat



Figure 5.16: ShockSat Top Plate

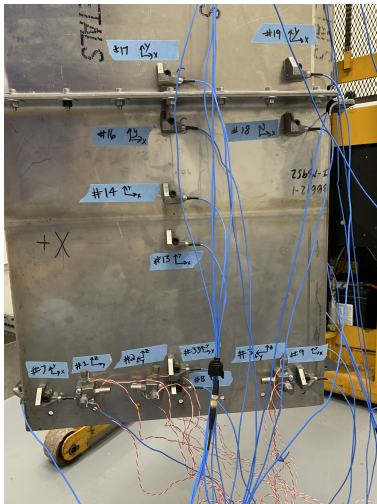


Figure 5.17: ShockSat +X Panel

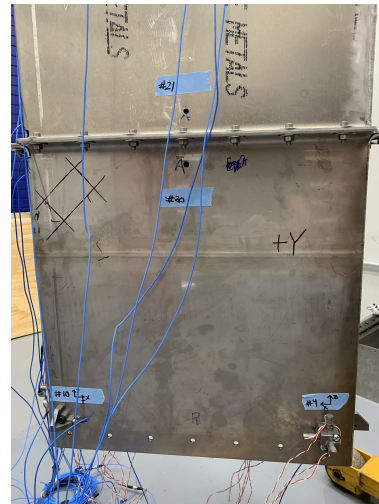


Figure 5.18: ShockSat +Y Panel



## FRF Comparison

The FRFs obtained from experimental and modal data are computed up to 10k Hz on the relevant locations. As an example, the comparison of FRFs is reported for X+ plate in 5.19,5.20,5.21, for Y+ plate in 5.22 and for top plate in 5.23.

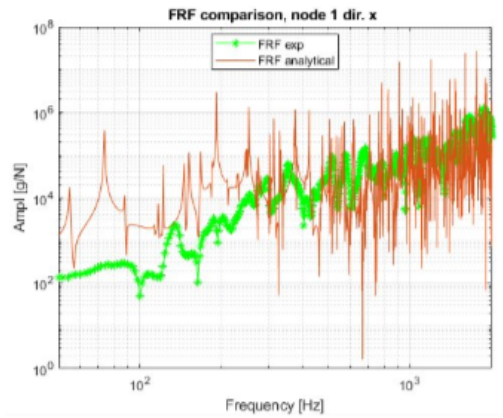


Figure 5.19: FRF of accelerometer 1, x direction

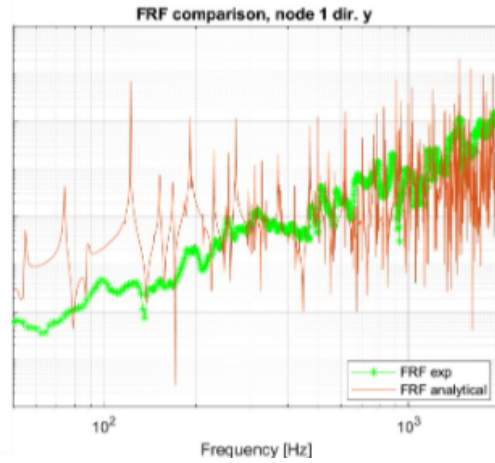


Figure 5.20: FRF of accelerometer 1, y direction

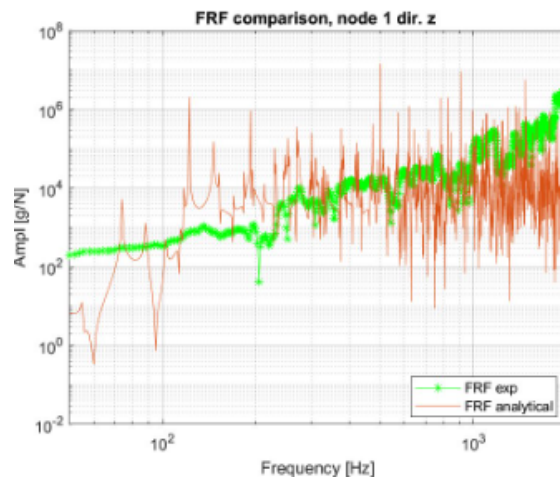


Figure 5.21: FRF of accelerometer 1, z direction

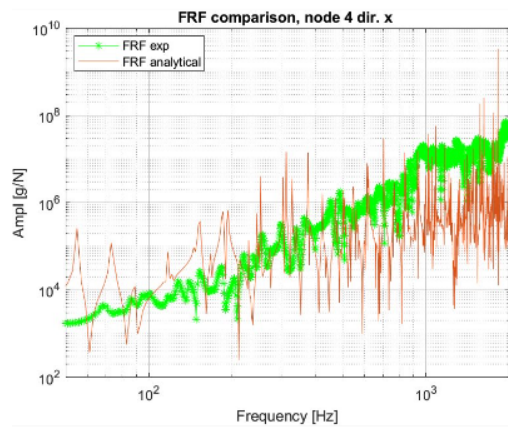


Figure 5.22: FRF of accelerometer 4, x direction

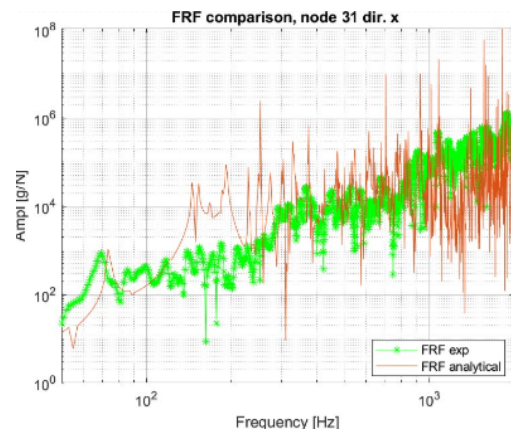


Figure 5.23: FRF of accelerometer 31, x direction

### 5.3.2 Shock Transmissibility

After deriving the FRF from modal parameters, it cannot be used directly to calculate the shock response. To address this, we must first convert it into a dimensionless form, which is where the previously introduced R-FRFs come into play. By transforming the FRF to a transmissibility function, we shift from a force-based relationship to an acceleration-to-acceleration format, which is more appropriate for shock response analysis. The transmissibility function, specifically the *global transmissibility*, represents the relationship between the dynamic responses (such as displacements, velocities, or accelerations) at various locations on the structure. It is computed by using 5.6, where  $H_{21}$  is the FRF matrix at the output location and  $H_{11}$  is the FRF matrix at the input location. This dimensionless transmissibility function encapsulates how disturbances propagate through the structure without dependency on the absolute values of the input force, making it ideal for calculating shock responses under various input conditions. Once the global transmissibility is obtained, we use it to derive the *shock transmissibility*, as detailed in Equation (5.1). On the experimental side, several pyroshock tests, as in 5.24, were performed in the configuration represented in 5.25. We extracted the recorded acceleration data from accelerometers placed in the structure along the three principal axes (X, Y, Z). To ensure that the data was correctly extracted, it has been compared with the available results in SRS form, like the ones in 5.26.

| Test No. | Date       | Source | Location             |
|----------|------------|--------|----------------------|
| 1        | 2021.08.26 | NSI    | +X Face, XYZ=(9,9,0) |
| 2        | 2021.10.13 | NSD    | +X Face, XYZ=(9,9,0) |
| 3        | 2021.10.14 | NSD    | +X Face, XYZ=(9,9,0) |
| 4        | 2021.10.14 | NSD    | +X Face, XYZ=(9,9,0) |
| 5        | 2021.10.14 | NSD    | +X Face, XYZ=(9,9,0) |

Figure 5.24: Pyroshock Tests performed on ShockSat



Figure 5.25: Shocksat Shock setup

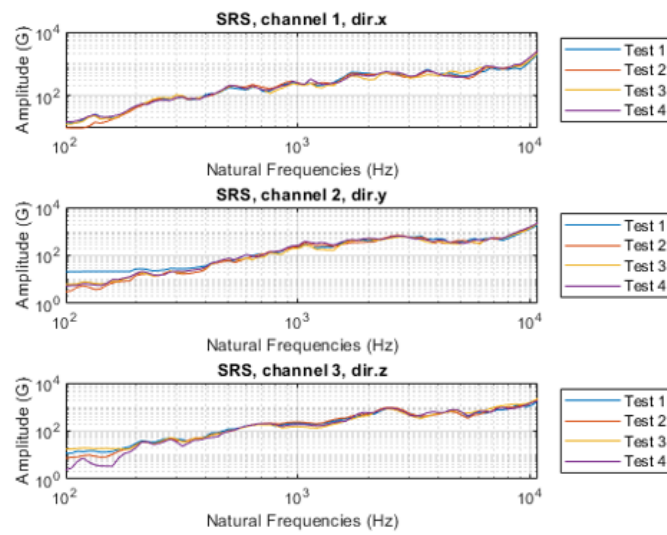


Figure 5.26: Experimental SRS responses

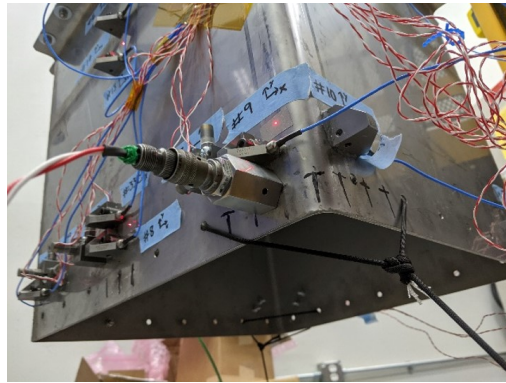


Figure 5.27: Pyroshock Test on ShockSat

### 5.3.3 Input identification

To compute the shock response, it is essential first to identify an appropriate shock input. Ideally, an experimental input that closely resembles the actual shock conditions would be used. However, precise measurements of accelerations due to pyrotechnic explosions are not feasible due to the highly non-linear nature of the phenomenon in the near field (within the first 5 cm of the shock source). Additionally, it is impractical to place sensors directly at the shock origin. As a result, we relied on accelerometer data recorded in the vicinity of the shock event, like the ones shown in 5.27. This choice was somewhat arbitrary, as different accelerometers or combinations of accelerometer data would produce variations in the computed response. The used signal can be seen in 5.28 in time domain and in 5.29 in Fast Fourier Transform form.

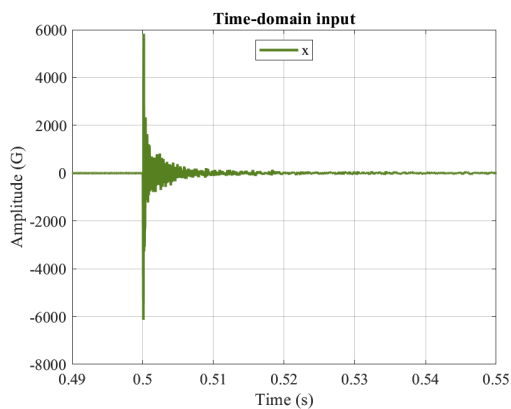


Figure 5.28: Synthesised input signal

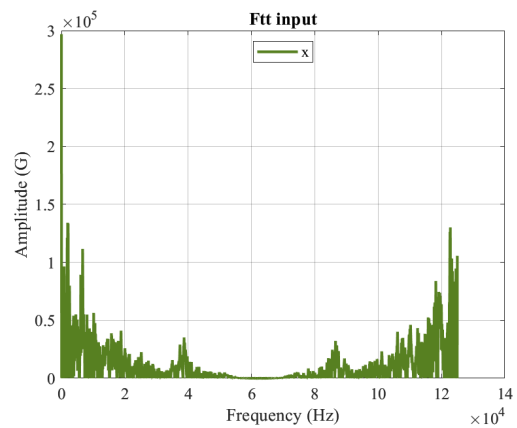


Figure 5.29: Fast Fourier Transform input signal

### 5.3.4 Shock Response Calculation

Once the shock input is selected, we employed two approaches for calculating the response:

1. **Frequency-Domain Approach:** In this approach, the chosen input acceleration signal was first converted from the time domain to a SRS. This SRS was then multiplied by the shock transmissibility to obtain the final shock response. This approach is particularly convenient because it allows for direct application of the transmissibility function in the frequency domain, yielding a straightforward prediction of the shock response.
2. **Time-Domain Approach:** In this alternative approach, the analysis was conducted directly in the time domain. The key difference between these two methods is that, in the frequency-domain approach, we work with the SRS of the input signal, while in the time-domain approach, we utilise the Fourier Transforms of the signals. The latter method is expected to be more precise, as it applies the transmissibility to the complete frequency content of the time-domain signals.

To calculate the shock response using the Inverse Fast Fourier Transform (IFFT) method, we start with an input shock signal in the time domain. The process involves transforming this time-domain signal into the frequency domain, where it can be effectively multiplied with the shock transmissibility to obtain the desired response. The detailed steps are as follows:

1. The input shock signal in the time domain of 5.28 is first transformed into the frequency domain using the Fast Fourier Transform (FFT). This transformation provides a complex frequency spectrum that represents the amplitude and phase of each frequency component of the input signal.
2. After obtaining the FFT of the input signal, we need to ensure that the frequency spectrum is symmetric. This symmetrisation step is crucial to ensure that the IFFT yields a real-valued time-domain response. When performing an IFFT on a non-symmetric frequency-domain signal, the result is generally complex. Symmetry, specifically Hermitian symmetry, around the zero frequency guarantees that the IFFT will produce a real response, which is necessary for meaningful physical interpretation. Symmetrisation is achieved by mirroring the positive frequency components across the origin into the negative frequency range, resulting in a Hermitian symmetric spectrum, as in 5.29.

3. Next, we multiply the symmetric frequency spectrum of the input signal by the shock transmissibility in the frequency domain in 5.30. The shock transmissibility is also made symmetric, as it needs to be compatible with the symmetric input spectrum. This multiplication effectively applies the frequency-dependent transfer function to the input signal, yielding the Fourier Transform of the system's response.
4. After the multiplication, we use the IFFT to transform the product back into the time domain. The shock response in time domain can be seen in 5.31
5. Finally, we convert the time-domain shock response into a SRS.

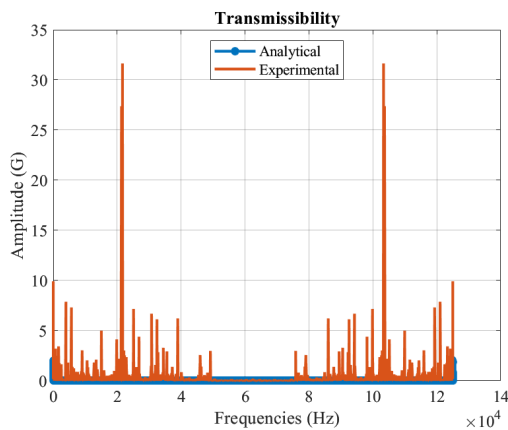


Figure 5.30: Transmissibility obtained by analytical/experimental FRF

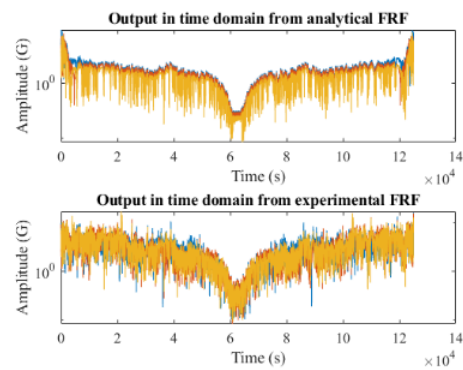


Figure 5.31: Output in time domain

In both cases, the shock response was computed using two types of transmissibility: one derived from modal FEM data and the other from experimental data obtained through hammer tests. This dual approach allowed for a comprehensive evaluation of the shock response methodology. Although the results are still under investigation, preliminary findings are presented in Figures 5.32 and 5.33. These examples show analyses conducted on accelerometer 1. Hereinafter, the differences between the shock transmissibility derived from experimental data and that obtained from modal analysis are presented in 5.34. The results shown are based on the iFFT method. These graphs illustrate that while theoretical models, whether derived from time-domain or frequency-domain analyses, offer useful insights into the shock response, they fall short of capturing the full complexity observed in experimental data. Up to approximately 500 Hz, the theoretical predictions align relatively well with the experimental results, indicating that the model captures

the general behaviour of the system in this lower frequency range. However, beyond 500 Hz, notable discrepancies begin to emerge, particularly as the frequency increases. This divergence suggests that higher frequencies introduce additional complexities, such as damping effects and non-linear interactions, which the current models do not adequately account for.

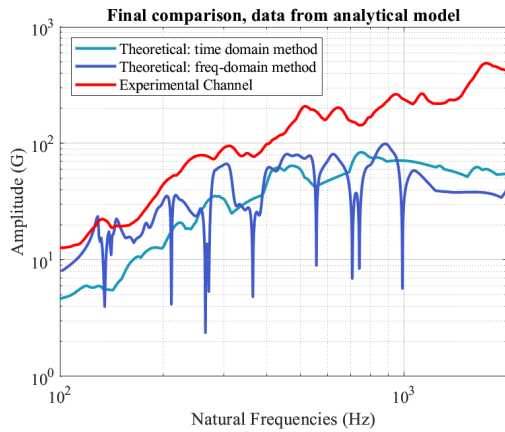


Figure 5.32: Comparison between the experimental response and the prediction obtained from modal data

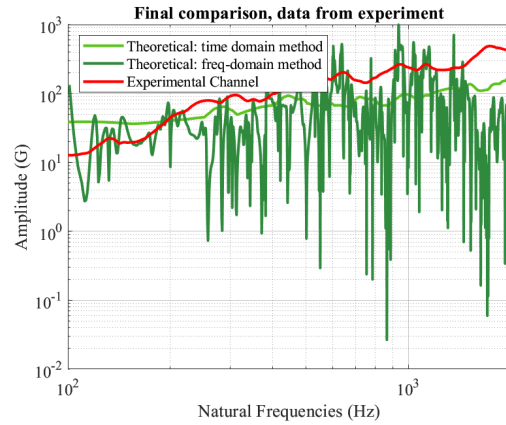


Figure 5.33: Comparison between the experimental response and the prediction obtained from experimental data

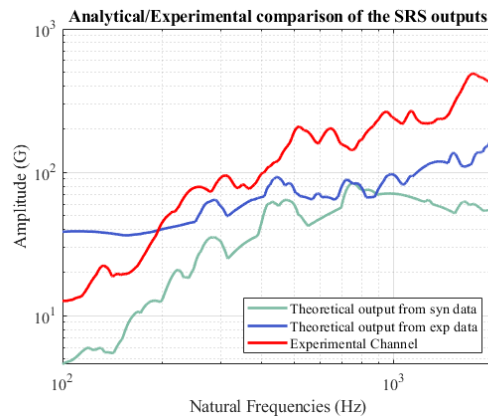


Figure 5.34: Comparison between the theoretical outputs obtained by the time domain method



## 5.4 Shock through composites

Shock propagation through composite materials has been the subject of significant research. Composite materials have gained significant attention for their ability to withstand high-impact forces while remaining lightweight, making them ideal for aerospace applications. These materials pose unique challenges due to their heterogeneous, anisotropic nature, which results in complex wave behaviour under dynamic loading. Composite laminates are formed by stacking layers of different materials and/or different fibre orientations. In general, their planar dimensions are two orders of magnitude larger than their thickness. Therefore, in many cases, composite laminates can be modelled using a shell element based on the Equivalent Single-Layer Theory (EST). This theory was initially developed to simplify the complex 3D problem of laminated composites into a 2D problem by making assumptions about displacement through the thickness. ESL theories simplify the problem by assuming a continuous displacement field through the thickness, expanded using Taylor polynomials:

$$\mathcal{U}(x, y, z, t) = F_0\mathcal{U}_0 + F_1\mathcal{U}_1 + \dots + F_N\mathcal{U}_N = F_\tau(z)\mathcal{U}(x, y, t), \quad (5.9)$$

where  $F_\tau = z^\tau$  and  $\tau = 0, 1, \dots, N$ . While EST provides accurate global responses for very thin laminates with minimal computational effort, it performs poorly in capturing local responses at the interfaces and cannot represent the zig-zag distribution of in-plane displacements. In contrast, elasticity solutions based on 3D displacement-based FEM provide precise displacement and stress fields but come with high computational costs. Layerwise Theories (LWT), considered a quasi 3D method, offer greater accuracy than most ESTs while requiring less computational power than 3D FEMs, making them increasingly popular with advances in computing technology. The method is described by the following equation:

$$\mathcal{U}^k(x, y, z, t) = F_\tau(x_k)\mathcal{U}_\tau^k(x, y, t) \quad (5.10)$$

where  $F_\tau^k$  are defined as Lagrange interpolation polynomials:

$$F_\tau^k(\zeta_k) = \prod_{i=0, i \neq \tau}^N \frac{\zeta_k - \zeta_{k_i}}{\zeta_{k_\tau} - \zeta_{k_i}} \quad (5.11)$$

in which  $-1 \leq \zeta_k \leq 1$  is the adimensional thickness coordinate in the layer  $k$ . For example  $\zeta_{k_0} = -1$  represents the bottom surface of the  $k$ -th layer, while  $\zeta_{k_N} = 1$  the top surface. [138] presents an overall review for the LWTs of the laminated composite structures and their applications. The Carrera Unified Formulation (CUF) generalises LW and ESL theories under a unified framework, allowing advanced 2D

models to approximate 3D behaviour effectively. The displacement field in CUF is expressed as:

$$\mathcal{U}(x, y, z, t) = F_\tau(z)\mathcal{U}_\tau(x, y, t), \quad (5.12)$$

where the thickness functions  $F_\tau(z)$  depend only on the  $z$  coordinate. CUF splits the original 3D problem into 2D in-plane and 1D thickness components, enabling efficient shell modelling. This flexibility makes CUF particularly suitable for analysing shock propagation in composite materials. CUF [139] uses the LWT theory to discretise the thickness with a mesh or higher-order expansion along the thickness direction. Using CUF allows to capture detailed, layer-by-layer variations in material properties providing a significant advantage over FEM in terms of accuracy and computational cost. [140] compares EST and LWT approaches in composite plates and structures using FEM and CUF. This section highlights the differences between the two methodologies when calculating shock propagation through composites structures. The objective is to show the superiority of CUF compared to FEM when studying the propagation of shock load through the thickness of the structure in a composite material. This section presents an alternative approach to evaluating the shock response of aerospace composite structures subjected to high-frequency transient loads, using a refined modeling methodology. The approach leverages CUF to describe the structure, which enhances a broad class of advanced 2D plate theories under a unified framework. This formulation provides a more comprehensive understanding of the dynamic behaviour of aerospace structures under shock loading. Applying the Finite Element (FE) approximation within the CUF framework involves introducing shape functions  $N_i$  to discretise the structural displacement field:

$$\mathcal{U}_\tau^k(x, y, t) = N_i(x, y)U_\tau^k(t), \quad (5.13)$$

where  $i = 1, \dots, n^s$ , and  $n^s$  is the number of nodes in the 2D structural element. Substituting this approximation into the displacement field expression yields:

$$\mathcal{U}_\tau^k(x, y, z, t) = F_\tau(z)N_i(x, y)U_\tau^k(t). \quad (5.14)$$

This formulation supports both ESL and LW approaches, depending on the chosen thickness functions  $F_\tau$ . The LW approach's higher-order accuracy, combined with the computational efficiency of CUF, offers a significant advantage for analysing shock propagation through composite materials, particularly under high-frequency transient loads. A key focus of this section is the comparison between the modal analyses obtained from commercial FEM software and those derived using the MUL2 code, which has shown superior accuracy for modeling composite materials. Using the modal analysis results from MUL2, the shock response of the composite structure is synthesised along its thickness, offering insights into its dynamic behaviour under high-frequency loading conditions. The methodologies discussed in

this section aim to improve the accuracy of predictive models, helping to ensure that spacecraft structures can withstand shock loads without requiring extensive redesigns. The findings contribute to enhancing the resilience of aerospace composite structures, reducing discrepancies between predicted and tested structural behaviour, and ultimately optimizing the spacecraft development process.

### 5.4.1 Comparison of FEM and MUL2

In this section, the response of a plate to a shock input is calculated using the previously described methodology. A half-sine pulse, shown in Fig. 5.35, is used as the input.

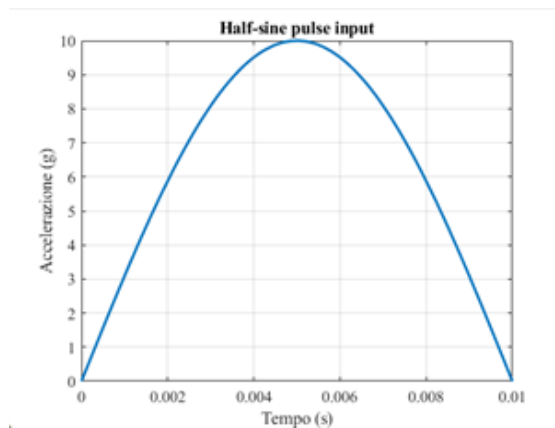


Figure 5.35: Half-sine pulse input

The time domain signal is converted to SRS, as shown in Fig. 5.36, to be used in Eq. 5.8.

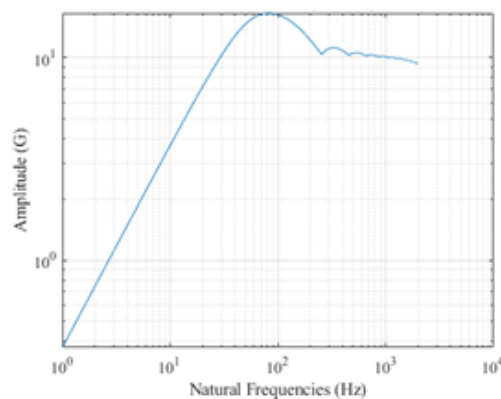


Figure 5.36: SRS of the half-sine pulse input

The response to this input has been applied on two different models: an isotropic aluminium plate and a composite plate composed of two layers of orthotropic material. Both models use a modal analysis computed up to 2000 Hz, and the differences between FEM and CUF methodologies are highlighted.

### 5.4.2 Aluminium Isotropic Plate

The system that has been studied is a thin plate of aluminium, with dimensions  $1 \times 1 \times 0.01$  m. The plate is clamped around all the edges. The FEM mesh is formed by QUAD elements with dimension 0.05 m. The mesh on MUL2 is composed of MITC elements that prevent locking phenomena, which could affect the analysis in the high-frequency range.

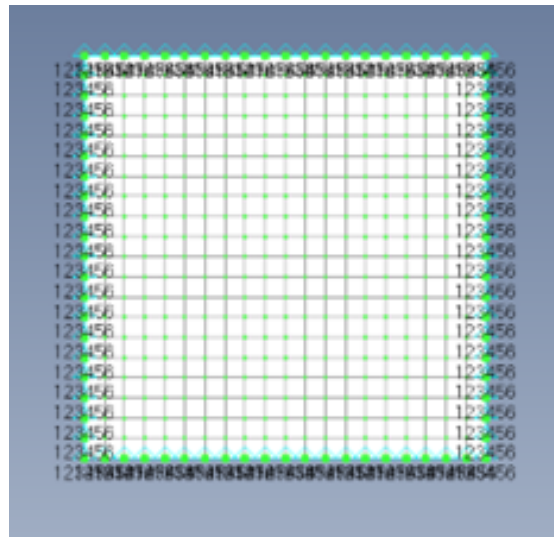


Figure 5.37: Clamped plate mesh on FEMAP

A modal analysis up to 2000 Hz has been performed on two commercial software packages, FEMAP and MUL2. The resulting natural frequencies present evident differences in the higher frequency range.

Then, the FRF (Frequency Response Function) of the structure has been computed using modal partial fraction decomposition of Eq. 5.4. The results obtained for the point located at  $[0.75, 0.75, 0]$  in the out-of-plane direction are shown in Figures 5.39 and 5.40.

The transmissibility is computed with Eq. 5.6.

The half-sine input is applied to the centre node of the plate at  $[0.5, 0.5, 0]$ . The shock response is then calculated using Eq. 5.8, and the results are shown in 5.42.

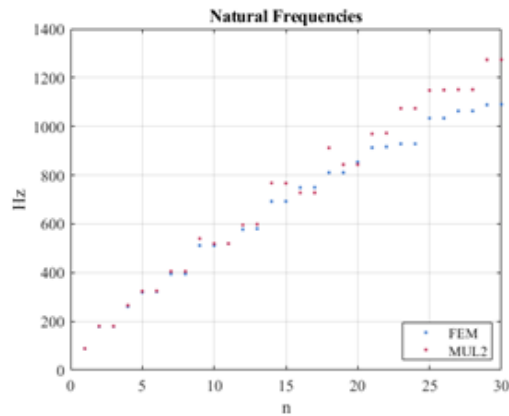


Figure 5.38: Natural frequencies comparison of the isotropic plate

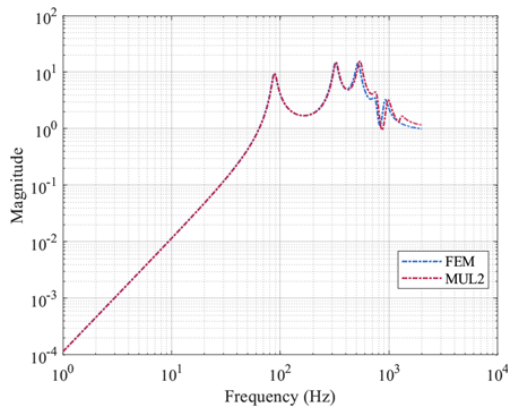


Figure 5.39: Isotropic composite plate, FRF Analysis - Magnitude

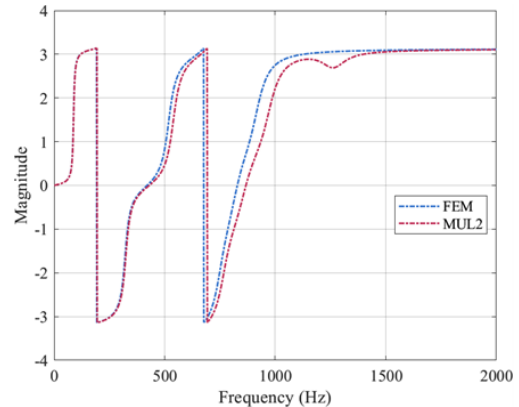


Figure 5.40: Isotropic composite plate, FRF Analysis - Phase

### 5.4.3 Composite Orthotropic Plate

The same procedure is applied to a plate with the same geometry and boundary conditions. The material is substituted with two layers of orthotropic composite material, positioned at 90 degrees to one another. The natural frequencies, FRF, and transmissibility comparison, as well as the response at the same location of the previous case, are shown in 5.43 ,5.44, 5.45, 5.46 and 5.47.

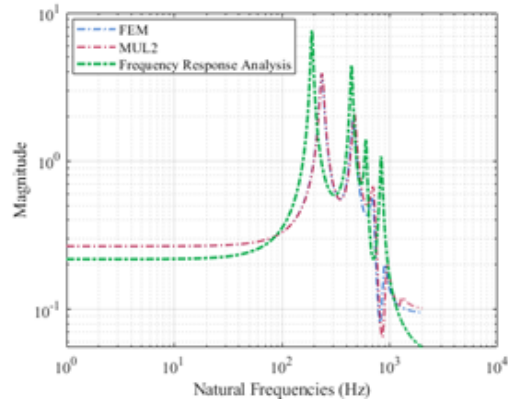


Figure 5.41: Transmissibility of the isotropic plate

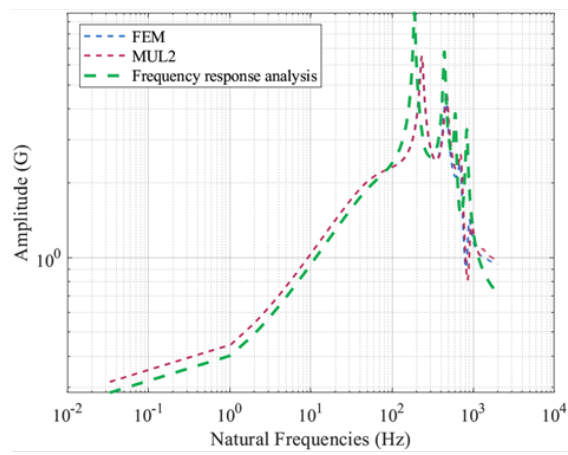


Figure 5.42: SRS output to half-sine input, isotropic plate

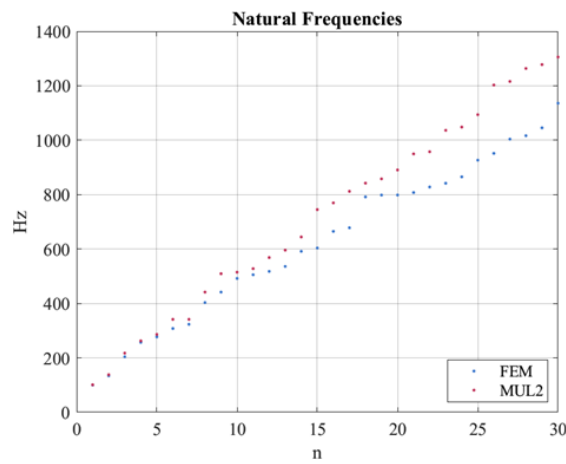


Figure 5.43: Natural frequencies comparison of the orthotropic plate

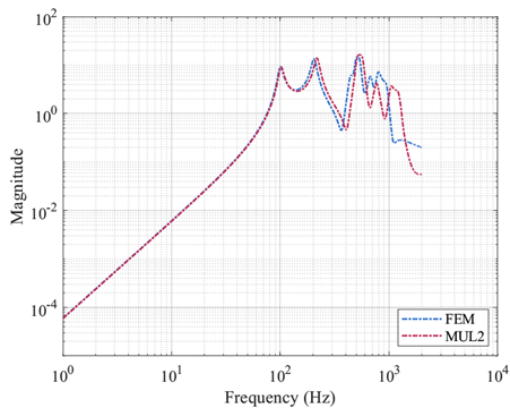


Figure 5.44: Orthotropic composite plate, FRF Analysis - Magnitude

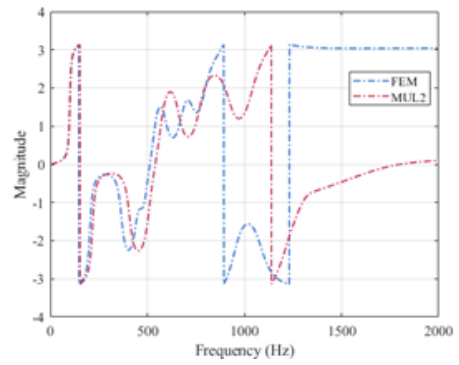


Figure 5.45: Orthotropic composite plate, FRF Analysis - Phase

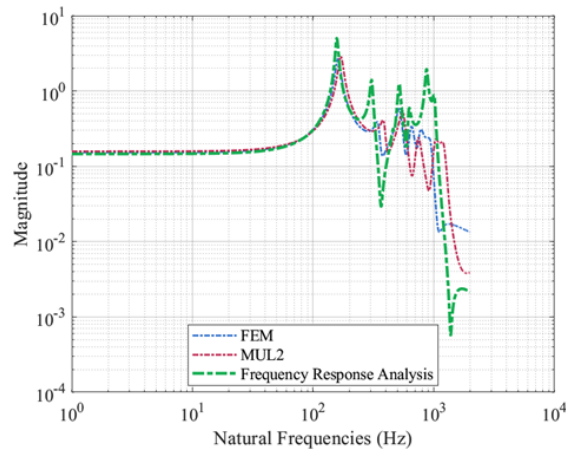


Figure 5.46: Transmissibility of the orthotropic plate

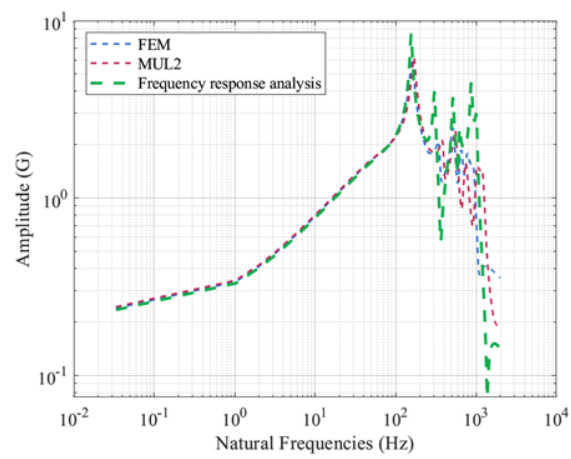


Figure 5.47: SRS output to half-sine input, orthotropic plate



**In a synthesis**

- Presentation of a predictive methodology for calculating shock responses in mechanical structures using modal decomposition and transfer functions.
- Application of the proposed methodology to both simple (2-DOF systems) and complex cases (e.g., ShockSat).
- Evaluation of shock propagation in composite materials, utilizing CUF to improve the accuracy of dynamic modeling in aerospace applications.
- Validation of the methodology through real-world data, including FEM models and physical shock tests, underscoring the method's effectiveness in predicting shock response across various aerospace structures.

# Conclusions

In response to the growing need for accurate shock prediction in the aerospace industry, this thesis presents a new methodology for analysing shock loads on satellite structures. Satellite launches expose structures to complex dynamic loads, including shocks from pyrotechnic events and stage separations, which challenge traditional modelling and validation methods. This thesis has thus focused on addressing these challenges, ultimately developing an adaptable, resource-efficient predictive model. The proposed model emphasizes modal analysis over traditional force-based measurements and extensive Finite Element Modelling (FEM), offering a practical alternative for the industry's cost-sensitive, high-stakes design and testing requirements. The scene was set by discussing the unique environmental challenges satellites encounter during launch and the critical need for structural resilience. Shock prediction models must account for the extreme and varied loads a satellite undergoes from the moment of lift-off through orbit insertion. Traditionally, the aerospace industry has relied on highly conservative methods that require considerable testing and over-design, which lead to increased costs. The challenge, therefore, is to find a balance between reducing the intensity and volume of physical tests while ensuring that models remain reliable across different satellite platforms and missions. The introduction also emphasized the unique role of this research in contributing to sustainable satellite development, particularly for reusable platforms. To start the research, an extensive review of current methods provided context for this research. Deterministic methods, like FEM, have long been industry standards, especially for low-frequency shock responses. However, deterministic approaches often fail to capture the nuances of high-frequency loads, which are characteristic of many launch and in-orbit events. Statistical approaches, such as Statistical Energy Analysis (SEA), address some of these limitations by averaging responses across the system, offering better predictive accuracy at higher frequencies. The chapter also examined hybrid methods, which blend deterministic and statistical techniques to enhance the flexibility and accuracy of predictions. The most innovative part of the state-of-art come from of data-driven and machine-learning-based approaches, which have seen increasing use in shock prediction modelling. The rise of Digital Twins, virtual representations of

physical systems updated in real-time with sensor data, has opened new possibilities for shock analysis. The chapter explored how integrating Digital Twins with Artificial Intelligence (AI) and Machine Learning (ML) can offer dynamic shock predictions. However, while these data-driven techniques present exciting opportunities, the research highlighted limitations, including reliance on high-quality data, potential inaccuracies in data fusion, and the need for further refinement to ensure consistency across diverse shock scenarios. In developing the shock prediction methodology, a strong theoretical foundation was laid by examining vibration analysis and shock phenomena from both microscopic and macroscopic perspectives. This involved studying modal analysis for single-degree-of-freedom (SDOF) and multi-degree-of-freedom (MDOF) systems, which provided insights into how structures respond to transient, non-periodic excitations such as shocks. By modelling the structure as discrete mass-spring-damper systems, this approach allowed complex satellite structures to be broken down into analysable components, enabling a clear understanding of both local and global shock responses. The study introduced Frequency Response Functions (FRFs) as essential tools, enabling precise calculations of the structure's reaction to shocks across a wide frequency range. This method provided a framework to assess how shock energy propagates through a structure, which is critical for accurately simulating high-frequency events like launch-induced shocks. Furthermore, SEA was incorporated to address high-frequency behaviours that are difficult to capture through deterministic models. Part of the research was dedicated to deepen the understanding of how shock inputs could be characterized and synthesised to match real-world conditions. SRS synthesis is vital in shock prediction as it captures the peak response of a structure to a transient shock event. Three primary synthesis techniques—wavelets, damped sinusoids, and enveloped sinusoids—were explored and applied to linear time-invariant (LTI) single degree-of-freedom (SDOF) systems as well as more complex viscoelastic SDOF systems. Afterwards, the research transitioned from theory to real-world implementation. The fourth chapter is focused on the activities carried out in SITAEL, specifically on the Multi-Application Minisatellite platform as a case study, showcasing the challenges faced in validating shock loads for satellites with repeated design features. Additionally, the chapter covered the requirements for shock testing, as well as the test setup that I helped design and implement to meet these stringent requirements. By reviewing existing shock tests and empirical methods currently used in industry, the chapter highlighted the limitations of traditional approaches and underscored the need for a more precise, efficient shock prediction model. This industry-focused analysis provided both a practical perspective on shock testing and validation, as well as a benchmark against which the proposed methodology could be compared and refined. Reaching the core of the research, a novel methodology based for calcu-

lating shock responses in both frequency and time domains was presented. Initial case studies were conducted on simplified mechanical models, beginning with a 2-degree-of-freedom (2-DOF) mass-spring-damper system. Although these early applications did not provide full experimental validation, they served as valuable test-beds for evaluating the consistency and coherence of the method. Synthesised input SRS values were derived using multiple approaches, and comparisons with the calculated system responses indicated a promising alignment with expected behaviours. This stage of research not only confirmed the feasibility of the method in a controlled setting but also laid the foundation for more complex applications. Over the following months, the methodology was systematically applied to increasingly intricate configurations, including single plates, orthogonal plate assemblies, and even composite materials. Another advancement in this research was the decision to integrate Carrera's Unified Formulation (CUF) as an alternative to traditional FEM analysis, especially for composite materials. Composites, with their anisotropic and layered structures, present unique challenges under dynamic loads, and CUF provided an innovative way to capture the localised shock propagation along the thickness of these materials. By addressing the limitations of conventional isotropic assumptions, CUF integration offered a pathway towards more precise, reliable predictions for shock-sensitive components made of advanced materials. The methodological development reached its peak of complexity with the application to NASA's ShockSat platform, a comprehensive test-bed designed explicitly for validating shock prediction models. Leveraging ShockSat's FEM and its rich set of experimental data, including modal tests and pyroshock tests, allowed a robust assessment of the proposed methodology's real-world applicability. Although full validation remains pending, ShockSat case study highlighted the potential of the methodology to align closely with observed experimental outcomes. This milestone not only underscored the scalability of the approach but also served as a stepping stone towards potential industry-standard applications. The next steps for this methodology include its application to the Multi-Application Minisatellite platform, with planned pyroshock tests at SITAEL, furthering the development of a fast and efficient approach to shock validation for recurrent satellite structures. This capability could enable SITAEL to streamline the structural validation process, reducing the need for repeated physical testing each time the platform structure is reused. This represents a highly valuable outcome for a company focused on creating reusable satellite platforms. The methodology has been investigated both frequency-domain and time-domain shock response calculations. In the frequency domain, the dimensionless shock transmissibility function was applied to the synthesised input SRS to model shock load propagation through various points on the structure. The time-domain approach, meanwhile, involved transforming the input shock signal into the frequency domain, symmetrising it,

and applying the shock transmissibility, followed by an inverse Fourier transform to return the response to the time domain. Reflecting on the broader implications, this thesis highlights the potential of this shock prediction methodology to drive industry-wide advancements in satellite design and testing. By reducing the dependency on extensive FEM simulations and direct force measurements, the R-FRF-based approach offers a practical and versatile alternative to current methods. This adaptability is particularly relevant for companies like SITAEL, which focus on developing reusable satellite platforms. The model's reduced computational burden and reliance on response-based rather than force-based data make it suitable for a range of satellite configurations, from simple plates to complex, multi-material assemblies.

The original contribution of the thesis is summed up as following:

- Provided an in-depth evaluation of deterministic, statistical, data-driven and hybrid shock prediction techniques, highlighting their limitations and proposing improvements tailored to the aerospace industry's needs.
- Developed a novel framework leveraging response-based transmissibility functions, offering a practical alternative to traditional FE methods.
- Applied the methodology to increasingly complex configurations, including composite materials, demonstrating its scalability and coherence with expected behaviours.
- Outlined the major obstacles to implementing shock analysis methodologies at an industry-wide level, paving the way for targeted advancements in shock prediction and validation techniques.

However, the research also revealed several limitations that need to be addressed to fully realize the model's potential:

- The absence of direct experimental validation remains a critical gap, particularly in assessing the accuracy of the model in real-world conditions. Collaborations with industry partners and aerospace institutions, including ESA and additional testing phases with SITAEL's Multi-Application Minisatellite platform, would be invaluable in achieving full experimental validation.
- The arbitrary selection of accelerometers as inputs introduces variability in the shock response, and further work is required to establish a standardized protocol for input selection to reduce these uncertainties.
- Capturing the precise shock characteristics of pyrotechnic events poses inherent challenges, as near-field recordings are impractical, and the shock

behaviour is highly non-linear. This research relied on accelerometer data from nearby locations, acknowledging the inherent limitations of such an approach.

Promising future improvements include:

- Incorporate advanced techniques to better account for damping effects in dynamic load propagation.
- Extend the methodology to address non-linear behaviour, which is a main characteristic of shock loads.
- Conduct experimental validation using simplified models as a starting point, progressing towards full-scale satellite tests.
- Development of a user-friendly interface accessible to engineers, allowing seamless application of the methodology in industrial settings.
- Expand the model's applicability to frequencies up to 10 kHz, ensuring compatibility with a broader range of shock events.
- Integrating machine learning techniques for model calibration, particularly in input selection and shock response prediction, could also enhance the adaptability of the model. AI-based calibration could allow the model to dynamically adjust to different shock scenarios, reducing the need for extensive input data and further streamlining the prediction process.

In conclusion, the R-FRF-based approach stands out as a practical and precise alternative to current shock prediction methods. It shows the potential to surpass the traditional ECSS empirical approach in accuracy, avoiding overly conservative assumptions, while being simpler and faster to implement than the complex FEM-SEA models, which require separate setups for different frequency ranges. By balancing accuracy with efficiency, this methodology promises to become an invaluable tool for the aerospace industry, supporting sustainable and cost-effective satellite design and validation.

# Acknowledgments

I would like to express my gratitude to SITAEL and the Structure's team of ESA-ESTEC for their support and for the opportunities they provided during my research. My thanks also go to my supervisors for their guidance throughout this project. I am particularly grateful to the team behind NASA ShockSat, whose work provided invaluable data and insights that greatly contributed to my study.

# Appendix A

---

```
1 %FRF Synthesis
2 %Generation of a synthetic FRF that matches the frequency
   resolution of the experimental FRF
3 file = 'modal-000.f06';
4 NaturalFrequencies = natf(file); %Hz
5 ModeShapes = eigenfind(file);
6
7 %Read the eigenvectors for the desired nodes, include input node
   at the beginning
8 Node 3 is X+ face, where the pyro test occurred, 1021515 is Y face
   , 2 is Z direction
9 node = [2,3,1021515,9900001:1:9900034];%3 X+ (pyro), 1021515 Y, 2
   Z
10
11 Phi_input_x = [ModeShapes.T1(7:end,2)];
12 Phi_input_y = [ModeShapes.T2(7:end,3)];
13 Phi_input_z = [ModeShapes.T3(7:end,1)];
14
15 INPUT = cat(2, Phi_input_x,Phi_input_y,Phi_input_z);
16 INPUT = permute(INPUT, [2 1]);
17
18 phi_x = ModeShapes.T1(7:end,[4:end]);
19 phi_y = ModeShapes.T2(7:end,[4:end]);
20 phi_z = ModeShapes.T3(7:end,[4:end]);
21
22 phiR_x = ModeShapes.T1(1:6,[4:end]);
23 phiR_y = ModeShapes.T2(1:6,[4:end]);
24 phiR_z = ModeShapes.T3(1:6,[4:end]);
25
26 PHI = cat(3, phi_x,phi_y,phi_z);
27 PHI = permute(PHI, [3 2 1]); % [m]
28
29 PHIreshaped = reshape(PHI,[size(PHI,1)*size(PHI,2) size(PHI,3)]);
30
31 PHI_R = cat(3, phiR_x,phiR_y,phiR_z);
32 PHI_R = permute(PHI_R, [3 2 1]); % [m]
33
```



```

34 PHI_Rreshaped = reshape(PHI_R, [size(PHI_R,1)*size(PHI_R,2) size(
    PHI_R,3)]);
35
36 %Scaling factor
37 wn = NaturalFrequencies(7:end)*2*pi';
38 nmodes = numel(wn);
39 Q = zeros(1, nmodes);
40
41 for j = 1:nmodes
42     Q(j) = 1/(2*wn(j));
43 end
44
45 Q = Q';
46
47 PHIA11 = nan(size(PHIreshaped,1)+3, size(PHIreshaped,2));
48 for mi = 1:nmodes
49     PHIA11(:,mi) = [INPUT(:,mi); PHIreshaped(:,mi)];
50 end
51
52 ngdl = size(PHIA11,1)
53
54 % FRF calculation
55 frequencies = f_frf;
56 numFreqs = length(frequencies);
57
58 omg = 2*pi*frequencies;
59
60 % Viscous damping
61 zita = 0.05; %1/20
62 wnd = -zita*wn+1i*sqrt(1-zita^2)*wn;
63
64 FRF = zeros(ngdl,3,numFreqs);
65 FRFmodal_acc_ms = zeros(ngdl,3,numFreqs);
66
67 for fi = 1:numFreqs
68     for p = 1:3
69         for mi = 1:nmodes
70             FRF(:,p,fi) = FRF(:,p,fi) + PHIA11(:,mi) .* ...
71                 ((-1i*Q(mi)*INPUT(p,mi)' / (1i*omg(fi) + wnd(mi)))
72                 + ...
73                 (1i*Q(mi)*INPUT(p,mi)' / (1i*omg(fi) + conj(wnd(mi)
74                 ))));
75             FRFmodal_acc_ms(:,p,fi) = FRFmodal_acc_ms(:,p,fi)
76                 - omg(fi).^2 * FRF(:,p,fi);
77         end
78     end
79 end
80 FRFsyn = FRFmodal_acc_ms / 9.81;

```

---

```

1
2 %% % Transmissibility calculation %%
3 addpath '\FRF_synthesis'
4 addpath '\Hammer_test'
5 load('FRFexp.mat', 'f_frf', 'FRFexp'); %Experimental FRF
6 load('FRFsyn.mat', 'FRFsyn'); %Analytical FRF
7
8 %% Tsyn
9
10 Tsyn = FRFsyn(1:end-1, :, :) ./ FRFsyn(end, 1, :);
11
12 sizeTsyn = size(Tsyn);
13
14 Tsyn2 = reshape(Tsyn, [sizeTsyn(1)*sizeTsyn(2) sizeTsyn(3)]);
15
16 %% Texp
17
18 Texp = (FRFexp(1:end-1, :, :) ./ FRFexp(end, 1, :));
19
20 sizeTexp = size(Texp);
21
22 Texp2 = reshape(Texp, [sizeTexp(1)*sizeTexp(2) sizeTexp(3)]);
23
24 %% %... impose symmetry of FRFs...
25
26 % Symmetry
27 N = size(Texp2, 2);
28
29 Tsynsym = nan(103, N);
30 Texpsym = nan(103, N);
31
32 for idrow = 1:103
33     % Analytical FRF symmetry
34     Tsyn_pos = real(Tsyn2(idrow, 1:ceil((N+1)/2)));
35     Tsyn_neg = fliplr(real(Tsyn2(idrow, 2:ceil(N/2))));
36     Tsynsym(idrow, :) = [Tsyn_pos, Tsyn_neg];
37
38     % Experimental FRF symmetry
39     Texp_pos = real(Texp2(idrow, 1:ceil((N+1)/2)));
40     Texp_neg = fliplr(real(Texp2(idrow, 2:ceil(N/2))));
41     Texpsym(idrow, :) = [Texp_pos, Texp_neg];
42 end

```

---

# References

- [1] A. García-Pérez, F. Sorribes-Palmer, G. Alonso, A. Ravanbakhsh, Overview and application of fem methods for shock analysis in space instruments, *Aerospace Science and Technology* 80 (2018) 572–586.
- [2] B. Li, Q. Li, Damage boundary of structural components under shock environment, *International Journal of Impact Engineering* 118 (2018) 67–77.
- [3] H. Zhao, W. Liu, J. Ding, Y. Sun, X. Li, Y. Liu, Numerical study on separation shock characteristics of pyrotechnic separation nuts, *Acta Astronautica* 151 (2018) 893–903.
- [4] J. Lee, D.-H. Hwang, J.-H. Han, Study on pyroshock propagation through plates with joints and washers, *Aerospace Science and Technology* 79 (2018) 441–458.
- [5] L. Meirovitch, *Fundamentals of Vibrations*, McGraw-Hill, 2001.
- [6] R. J. Allemang, *Vibrations: Experimental Modal Analysis*, University of Cincinnati, Cincinnati, Ohio, 1999, uC-SDRL-CN-20-263-663/664.
- [7] R. J. Allemang, *Vibrations: Analytical and Experimental Modal Analysis*, University of Cincinnati, Cincinnati, Ohio, 1999, uC-SDRL-CN-20-263-662.
- [8] D. J. Ewins, *Modal Testing: Theory, Practice and Application*, 2nd Edition, Research Studies Press, 2000.
- [9] H. G. Pasha, R. J. Allemang, A. W. Phillips, Techniques for synthesizing frfs from analytical models, *Vibrations: Analytical and Experimental Modal Analysis* (Year of publication if known).
- [10] S. D. Rosa, F. Ricci, F. Franco, *Introduzione alla Tecnica Statistico-Energetica (S.E.A.) per la Dinamica Strutturale e l'Acustica Interna*, Liguori Editore, 1999.

- 
- [11] D. E. Newland, *An Introduction to Random Vibrations, Spectral & Wavelet Analysis*, 3rd Edition, Dover Publications, Inc., Mineola, New York, 2005.
- [12] F. S. Tse, I. E. Morse, R. T. Hinkle, *Mechanical Vibrations: Theory and Applications*, 2nd Edition, Allyn and Bacon, Inc., Boston, London, Sydney, Toronto, 2004.
- [13] N. Maia, J. M. N. Silva, W. M. To, *Theoretical and Experimental Modal Analysis*, Research Studies Press, 1997.
- [14] C. Lalanne, *Mechanical Shock*, 3rd Edition, CRC Press, 2020. doi:10.1201/9780367810993.
- [15] K. J. Bathe, *Finite Element Procedures*, Prentice Hall, 1996.
- [16] R. D. Cook, *Concepts and Applications of Finite Element Analysis*, Wiley, 2017.
- [17] V. I. Bateman, H. Himelblau, R. Merritt, [Validation of pyroshock data](#), *Journal of the IEST* 55 (1) (2012) 1–13, accessed: YYYY-MM-DD. doi:10.17764/jiet.55.1.2q4650xqt7j0k506.  
URL [https://www.researchgate.net/publication/277361943\\_Validation\\_of\\_Pyroshock\\_Data](https://www.researchgate.net/publication/277361943_Validation_of_Pyroshock_Data)
- [18] European Space Agency (ESA), *Shocks Propagation Prediction in Satellite Structures*.
- [19] European Space Agency (ESA), *Shocks Propagation Prediction in Satellite Structures*.
- [20] F. J. Fahy, [Statistical energy analysis: a critical overview](#), *Philosophical Transactions of the Royal Society of London. Series A: Physical and Engineering Sciences* 346 (1681) (March 1994). doi:10.1098/rsta.1994.0027.  
URL <https://doi.org/10.1098/rsta.1994.0027>
- [21] A. J. Keane, W. G. Price, *Statistical Energy Analysis: An Overview, with Applications in Structural Dynamics*, Cambridge University Press, 1997.
- [22] R. H. Lyon, *Statistical Energy Analysis of Dynamical Systems*, MIT Press, 1975.
- [23] E. Sarradj, *Statistical energy analysis in vibroacoustics: Recent advances and applications*, *Applied Acoustics* 174 (2021) 107740. doi:10.1016/j.apacoust.2020.107740.

- [24] R. Lyon, What good is statistical energy analysis, anyway?, *The Shock and Vibration Digest* 2 (6) (1970).
- [25] X. Wang, W. Liu, X. Li, Y. Sun, [The shock response prediction of spacecraft structure based on hybrid fe-sea method](#), *Applied Sciences* 11 (18) (2021) 8490. doi:10.3390/app11188490. URL <https://www.mdpi.com/2076-3417/11/18/8490>
- [26] J.-R. Lee, C. Chen, C.-W. Kong, Review of pyroshock wave measurement and simulation for space systems, *Measurement* 45 (2012) 631–642.
- [27] B. Troclet, B. Hiverniau, M. Ichchou, L. Jezequel, K. Kayvantash, T. Bekkour, J. Mouillet, A. Gallet, FEM/SEA hybrid method for predicting mid and high frequency structure-borne transmission, *Open Acoustics Journal* 2 (2009).
- [28] E. Dalton, I. S.B. Chambers, Analysis and validation testing of impulsive load response in complex, multi-compartmented structures, in: *Proceedings of the Structures, Structural Dynamics and Materials Conference*, New Orleans, LA, USA, 1995, pp. 759–767.
- [29] E. Dalton, A. Frydman, A. Li, M. Berman, High frequency shock predictions in armored vehicles: Ags case study, in: *Proceedings of the 16th International Symposium on Ballistics*, San Francisco, CA, USA, 1996, pp. 1198–1210.
- [30] E. Dalton, R. Loper, A. Frydman, D. Li, M. Berman, Simulation of ballistic shock in composite armored vehicles, in: *Proceedings of the 68th Shock and Vibration Symposium*, Hunt Valley, MD, USA, 1997, pp. 992–1016.
- [31] E. Dalton, M. White, A. Frydman, Parameter sensitivity for statistical energy analysis methods of ballistic shock simulation, in: *Proceedings of the 69th Shock and Vibration Symposium*, Minneapolis, MN, USA, 1996, pp. 688–702.
- [32] E. Dalton, High Frequency Shock Prediction, Short Course Notes, Military Technology Inc., New York, NY, USA, 1999.
- [33] X. Wang, Z. Qin, J. Ding, F. Chu, Finite element modeling and pyroshock response analysis of separation nuts, *Aerospace Science and Technology* 68 (2017) 380–390.
- [34] J. Lee, J.-H. Han, Y. Lee, H. Lee, Separation characteristics study of ridge-cut explosive bolts, *Aerospace Science and Technology* 39 (2014) 153–168.

- [35] G. Bikakis, C. Dimou, E. Sideridis, Ballistic impact response of fiber-metal laminates and monolithic metal plates consisting of different aluminum alloys, *Aerospace Science and Technology* 69 (2017) 201–208.
- [36] H.-J. Hwang, H.-K. Yoon, S.-M. Han, J.-H. Lee, [Analysis and test for spacecraft structure under pyroshock environment](#), *Journal of the Korean Society for Aeronautical and Space Sciences* 38 (9) (2010) 1040–1048. doi: [10.5139/JKSAS.2010.38.9.1040](https://doi.org/10.5139/JKSAS.2010.38.9.1040).  
URL <https://koreascience.kr/article/JAKO201019657416371.pdf>
- [37] Y. Liu, Z.-J. Yang, Z.-Z. Wang, W.-Q. Xu, L.-H. Zhang, H.-H. Su, [A comparative study of the pyroshock response prediction for a spacecraft using different shock response spectrum estimation methods](#), *Acta Astronautica* 173 (2020) 424–434. doi: [10.1016/j.actaastro.2020.05.027](https://doi.org/10.1016/j.actaastro.2020.05.027).  
URL <https://doi.org/10.1016/j.actaastro.2020.05.027>
- [38] H. Zhao, J. Ding, W. Zhu, Y. Sun, Y. Liu, [Shock response prediction of the typical structure in spacecraft based on the hybrid modeling techniques](#), *Aerospace Science and Technology* (2019) 1–8 Accessed: YYYY-MM-DD. doi: [10.1016/j.ast.2019.04.018](https://doi.org/10.1016/j.ast.2019.04.018).  
URL <https://doi.org/10.1016/j.ast.2019.04.018>
- [39] X. Wang, W. Liu, J. Ding, Y. Sun, Y. Dang, [Pyroshock response prediction of spacecraft structure in wide frequency domain based on acceleration frf](#), *Aerospace* 9 (2) (2022) 54. doi: [10.3390/aerospace9020054](https://doi.org/10.3390/aerospace9020054).  
URL <https://doi.org/10.3390/aerospace9020054>
- [40] European Space Agency (ESA), Shock Response Predictions on Electronic Units.
- [41] J. H.-J. Hwang, G. Borello, J. P. Fernandez, Improved pyrotechnic shock scaling method based on shock response spectrum and statistical energy analysis, in: *Proceedings of the European Conference on Spacecraft Structures, Materials and Environmental Testing (ECSSMET)*, ESTEC, Noordwijk, The Netherlands, 2018, p. N/A.
- [42] NASA Goddard Space Flight Center, General environmental verification standard (gevs) for gsfc flight programs and projects, Tech. Rep. GSFC-STD-7000A, NASA Goddard Space Flight Center, Greenbelt, Maryland (2013).
- [43] H. Wang, K. Yu, R. Zhao, [Prediction of the transient local energy by energy finite element analysis](#), *Mathematics* 11 (22) (2023) 4590. doi: [10.3390/math11224590](https://doi.org/10.3390/math11224590).  
URL <https://doi.org/10.3390/math11224590>

- [44] N. Vlahopoulos, S. Lee, [Energy Finite Element Analysis](#), John Wiley & Sons, Ltd., 2016. doi:10.1002/9781118693988.  
URL <https://doi.org/10.1002/9781118693988>
- [45] W. Desmet, Mid-frequency vibro-acoustic modelling: Challenges and potential solutions, in: Proceedings of the ISMA, Lueven, Belgium, 2002, p. 12.
- [46] C. Roque, A. Ferreira, J. Reddy, Analysis of timoshenko nanobeams with a nonlocal formulation and meshless method, *International Journal of Engineering Science* 49 (2011) 976–984. doi:10.1016/j.ijengsci.2011.01.001.
- [47] J. Banerjee, Free vibration analysis of a twisted beam using the dynamic stiffness method, *International Journal of Solids and Structures* 38 (2001) 6703–6722. doi:10.1016/S0020-7683(00)00378-6.
- [48] J. Banerjee, A. Ananthapuvirajah, An exact dynamic stiffness matrix for a beam incorporating rayleigh–love and timoshenko theories, *International Journal of Mechanical Sciences* 150 (2019) 337–347. doi:10.1016/j.ijmecsci.2018.10.018.
- [49] N. Atalla, R. Bernhard, Review of numerical solutions for low-frequency structural acoustic problems, *Applied Acoustics* 43 (1994) 271–294.
- [50] M. Cinefra, A. G. de Miguel, M. Filippi, C. Houriet, A. Pagani, E. Carrera, Homogenization and free-vibration analysis of elastic metamaterial plates by cuf finite elements, *Mechanics of Advanced Materials and Structures* (2019) 1–10.
- [51] E. Carrera, M. Cinefra, M. Petrolo, E. Zappino, *Finite Element Analysis of Structures Through Unified Formulation*, John Wiley & Sons, 2014.
- [52] S. Danu, N. Saini, Y. Khan, H. Sharma, Composites for vibro-acoustics—a review, *International Journal of Applied Engineering Research* 14 (2019) 6–11.
- [53] D. J. Gorman, W. Ding, Accurate free vibration analysis of completely free symmetric cross-ply rectangular laminated plates, *Composite Structures* 60 (2003) 359–365.
- [54] Y. Kagan, L. Knopoff, [Earthquake risk prediction as a stochastic process](#), *Physics of the Earth and Planetary Interiors* 14 (2) (1977) 97–108. doi:10.1016/0031-9201(77)90003-8.  
URL [https://doi.org/10.1016/0031-9201\(77\)90003-8](https://doi.org/10.1016/0031-9201(77)90003-8)

- [55] M. Papadrakakis, G. Stefanou, Efficient monte carlo simulation in stochastic finite element analysis using coarse and fine meshes, *Computer Methods in Applied Mechanics and Engineering* 213-216 (2012) 135–144. doi:10.1016/j.cma.2011.12.013.
- [56] G. Stefanou, The stochastic finite element method: Past, present and future, *Computer Methods in Applied Mechanics and Engineering* 198 (9-12) (2009) 1031–1051. doi:10.1016/j.cma.2008.11.007.
- [57] V. Yotov, M. Remedia, G. Aglietti, Decomposition based stochastic fem for spacecraft vibroacoustic simulations, *Protection Against Increased Noise and Vibration Conference Proceedings* (2022) 277–284.
- [58] R. G. Ghanem, P. D. Spanos, *Stochastic Finite Elements: A Spectral Approach*, Springer, 1991.
- [59] D. Xiu, *Numerical Methods for Stochastic Computations: A Spectral Method Approach*, Princeton University Press, 2010.
- [60] F. J. Montáns, F. Chinesta, R. Gómez-Bombarelli, J. N. Kutz, **Data-driven modeling and learning in science and engineering**, *Data-Based Engineering Science and Technology / Sciences et technologies de l'ingénierie basées sur les données* Author links open overlay panel (Published Online).  
URL <InsertspecificURLhere>
- [61] P. Sjövall, T. Abrahamsson, Substructure system identification from coupled system test data, *Mechanical Systems and Signal Processing* 22 (1) (2008) 15–33. doi:10.1016/j.ymsp.2007.06.003.
- [62] A. Meixedo, J. Santos, D. Ribeiro, R. Calçada, M. Todd, Damage detection in railway bridges using traffic-induced dynamic responses, *Engineering Structures* 238 (2021) 112189. doi:10.1016/j.engstruct.2021.112189.
- [63] L. Rosafalco, M. Torzoni, A. Manzoni, S. Mariani, A. Corigliano, Online structural health monitoring by model order reduction and deep learning algorithms, *Computers & Structures* 255 (2021) 106604. doi:10.1016/j.compstruc.2021.106604.
- [64] A. Roeder, H. Zhang, L. Sanchez, Y. Yang, C. Farrar, D. Mascareñas, Identification of full-field dynamic loads on structures using computer vision and unsupervised machine learning, in: *Shock & Vibration, Aircraft/Aerospace, Energy Harvesting, Acoustics & Optics, Volume 9, Conference Proceedings of the Society for Experimental Mechanics Series (CPSEMS)*, 2017, pp. 41–48. doi:FirstOnline:18April2017.



- [65] J. J. Pannell, Surrogate modelling strategies for the prediction of near-field blast impulse, Phd thesis, University of Sheffield (2022).
- [66] C. Cheung, J. J. Valdes, M. Li, Use of evolutionary computation techniques for exploration and prediction of helicopter loads, in: 2012 IEEE Congress on Evolutionary Computation, IEEE, 2012, p. N/A. doi:10.1109/CEC.2012.6256494.
- [67] M. Castellani, Y. Lemmens, J. E. Cooper, Parametric reduced order model approach for rapid dynamic loads prediction, Aerospace Science and Technology 52 (2016) 29–40. doi:10.1016/j.ast.2016.01.012.
- [68] K. Hickmann, D. Shutt, A. K. Robinson, J. Lind, Data-driven learning of impactor strength properties from shock experiments with additively manufactured materials, in: Proceedings Volume 11843, Applications of Machine Learning 2021, 2021, p. N/A. doi:10.1117/12.2594898. URL <https://doi.org/10.1117/12.2594898>
- [69] B. Shaheen, Á. Kocsis, I. Németh, Data-driven failure prediction and rul estimation of mechanical components using accumulative artificial neural networks, Engineering Applications of Artificial Intelligence 119 (2023) 105749. doi:10.1016/j.engappai.2023.105749.
- [70] N. Chen, H. Liu, F. Lu, Shock trace prediction by reduced models for a viscous stochastic burgers equation, Chaos: An Interdisciplinary Journal of Nonlinear Science 32 (4) (2022) 043113. doi:10.1063/5.0084970. URL <https://doi.org/10.1063/5.0084970>
- [71] S. Waimer, S. Manzato, B. Peeters, A. Carrella, M. Wagner, P. Guillaume, Experimental data driven approach for numerical spacecraft vibration test prediction, in: Proceedings of the European Conference on Spacecraft Structures, Materials and Environmental Testing (ECSSMET), ESTEC, Noordwijk, The Netherlands, 2018, p. N/A.
- [72] N. A. Kartam, I. Flood, Artificial Neural Networks for Civil Engineers: Fundamentals and Applications, American Society of Civil Engineers, Reston, VA, 1998.
- [73] J. Ma, S. Dong, G. Chen, P. Peng, L. Qian, A data-driven normal contact force model based on artificial neural network for complex contacting surfaces, Mechanical Systems and Signal Processing 156 (2021) 107612. doi:10.1016/j.ymsp.2021.107612.

- [74] S. Mouloudi, H. Rahmanpanah, S. Gohari, C. Burvill, H. M. S. Davies, Feed-forward backpropagation artificial neural networks for predicting mechanical responses in complex nonlinear structures: A study on a long bone, *Journal of the Mechanical Behavior of Biomedical Materials* 128 (2022) 105079. [doi:10.1016/j.jmbbm.2022.105079](https://doi.org/10.1016/j.jmbbm.2022.105079).
- [75] I. E. Lagaris, A. Likas, D. I. Fotiadis, Artificial neural networks for solving ordinary and partial differential equations, *IEEE Transactions on Neural Networks* 9 (5) (1998) 987–1000. [doi:10.1109/72.712178](https://doi.org/10.1109/72.712178).
- [76] S. Gantasala, J.-C. Luneno, J.-O. Aidanpää, Investigating how an artificial neural network model can be used to detect added mass on a non-rotating beam using its natural frequencies: A possible application for wind turbine blade ice detection, *Energies* 10 (2) (2017) 184. [doi:10.3390/en10020184](https://doi.org/10.3390/en10020184).
- [77] P. Tsou, M. H. Shen, Structural damage detection and identification using neural networks, *AIAA Journal* 32 (1) (1994) 176–183. [doi:10.2514/3.11964](https://doi.org/10.2514/3.11964).
- [78] H. Luo, S. Hanagud, Dynamic learning rate neural network training and composite structural damage detection, *AIAA Journal* 35 (9) (1997) 1522–1527. [doi:10.2514/2.7480](https://doi.org/10.2514/2.7480).
- [79] S. M. Statham, S. V. Hanagud, B. J. Glass, Automated, real-time health monitoring of structures for interplanetary exploration systems, *AIAA Journal* 50 (12) (2012) 2670–2682. [doi:10.2514/1.J051173](https://doi.org/10.2514/1.J051173).
- [80] T. Wang, W. Altabey, M. Noori, R. Ghiassi, A deep learning based approach for response prediction of beam-like structures, *Structural Durability and Health Monitoring* 14 (2020) 315. [doi:10.32604/sdhm.2020.09752](https://doi.org/10.32604/sdhm.2020.09752).
- [81] S. Rajasekaran, H. Khaniki, M. Ghayesh, On the mechanics of shear deformable micro beams under thermo-mechanical loads using finite element analysis and deep learning neural network, *Mechanics Based Design of Structures and Machines* 51 (2022) 6612–6656. [doi:10.1080/15397734.2022.2039284](https://doi.org/10.1080/15397734.2022.2039284).
- [82] H. Tan, W. Liu, Deep autoencoders for feature extraction in mechanical shock data, *IEEE Transactions on Industrial Electronics* 68 (9) (2021) 1278–1289.
- [83] Y. Huang, X. Han, L. Zhao, Recurrent neural networks for complicated seismic dynamic response prediction of a slope system, *Engineering Geology* 289 (2021) 106198. [doi:10.1016/j.enggeo.2021.106198](https://doi.org/10.1016/j.enggeo.2021.106198).

- [84] Z. Xu, J. Chen, J. Shen, M. Xiang, Recursive long short-term memory network for predicting nonlinear structural seismic response, *Engineering Structures* 250 (2022) 113406. doi:10.1016/j.engstruct.2021.113406.
- [85] M. Grieves, J. Vickers, Digital twin: Mitigating unpredictable, undesirable emergent behavior in complex systems (excerpt), in: *Trans-Disciplinary Perspectives on System Complexity*, All rights reserved, n.d., p. N/A.
- [86] R. Rosen, G. Von Wichert, G. Lo, K. D. Bettenhausen, About the importance of autonomy and digital twins for the future of manufacturing, *IFAC PapersOnLine* 48 (3) (2015) 567–572. doi:10.1016/j.ifacol.2015.06.141.
- [87] T. Gabor, L. Belzner, M. Kiermeier, M. T. Beck, A. Neitz, A simulation-based architecture for smart cyber-physical systems, in: *2016 IEEE International Conference on Autonomic Computing (ICAC)*, IEEE, 2016, pp. 374–379. doi:10.1109/ICAC.2016.41.
- [88] M. Bajaj, B. Cole, D. Zwemer, Architecture to geometry-integrating system models with mechanical design, in: *AIAA SPACE 2016*, American Institute of Aeronautics and Astronautics, 2016, p. 5470.
- [89] Y. Bazilevs, X. Deng, A. Korobenko, F. Lanza di Scalea, M. D. Todd, S. G. Taylor, Isogeometric fatigue damage prediction in large-scale composite structures driven by dynamic sensor data, *Journal of Applied Mechanics* 82 (9) (2015). doi:10.1115/1.4030353.
- [90] K. Reifsnider, P. Majumdar, Multiphysics stimulated simulation digital twin methods for fleet management, in: *54th AIAA/ASME/ASCE/AHS/ASC Structures, Structural Dynamics, and Materials Conference*, American Institute of Aeronautics and Astronautics, 2013, p. 1578.
- [91] E. Tuegel, The airframe digital twin: Some challenges to realization, in: *53rd AIAA/ASME/ASCE/AHS/ASC Structures, Structural Dynamics and Materials Conference, 20th AIAA/ASME/AHS Adaptive Structures Conference, 14th AIAA*, American Institute of Aeronautics and Astronautics, 2012, p. 1812.
- [92] C. Semeraro, M. Lezoche, H. Panetto, M. Dassisti, Digital twin paradigm: A systematic literature review, *Computers in Industry* 130 (2021) 103469. doi:10.1016/j.compind.2021.103469.
- [93] E. Glaessgen, D. Stargel, The digital twin paradigm for future nasa and u.s. air force vehicles, in: *51st AIAA/ASME/ASCE/AHS/ASC Structures*,

- Structural Dynamics, and Materials Conference, NASA, Reston, VA, 2012, p. N/A. [doi:10.2514/6.2010-1234](https://doi.org/10.2514/6.2010-1234).
- [94] R. K. Phanden, P. Sharma, A. Dubey, A review on simulation in digital twin for aerospace, manufacturing and robotics, *Materials Today: Proceedings* 38, Part 1 (2021) 174–178. [doi:10.1016/j.matpr.2020.08.474](https://doi.org/10.1016/j.matpr.2020.08.474).
- [95] L. Li, S. Aslam, A. Wileman, S. Perinpanayagam, Digital twin in aerospace industry: A gentle introduction, *IEEE Access* 10 (2021) 3136458, received November 7, 2021; accepted December 3, 2021; published December 20, 2021; current version January 27, 2022.
- [96] I. Pan, L. R. Mason, O. K. Matar, Data-centric engineering: Integrating simulation, machine learning and statistics. challenges and opportunities, *Chemical Engineering Science* 249 (2022) 117271. [doi:10.1016/j.ces.2021.117271](https://doi.org/10.1016/j.ces.2021.117271).
- [97] M. Farid, Data-driven method for real-time prediction and uncertainty quantification of fatigue failure under stochastic loading using artificial neural networks and gaussian process regression, *International Journal of Fatigue* 155 (2022) 106415. [doi:10.1016/j.ijfatigue.2021.106415](https://doi.org/10.1016/j.ijfatigue.2021.106415).
- [98] A. M. Stanković, A. A. Sarić, A. T. Sarić, M. K. Transtrum, Interleaving physics- and data-driven models for power system transient dynamics, *Electric Power Systems Research* 189 (2020) 106824. [doi:10.1016/j.epsr.2020.106824](https://doi.org/10.1016/j.epsr.2020.106824).
- [99] S. B. Cooper, D. DiMaio, Static load estimation using artificial neural network: Application on a wing rib, *Advances in Engineering Software* 125 (2018) 113–125. [doi:10.1016/j.advengsoft.2018.07.007](https://doi.org/10.1016/j.advengsoft.2018.07.007).
- [100] H. B. Kong, S.-H. Jo, J. H. Jung, J. M. Ha, Y. C. Shin, H. Yoon, K. H. Sun, Y.-H. Seo, B. C. Jeon, A hybrid approach of data-driven and physics-based methods for estimation and prediction of fatigue crack growth, *International Journal of Prognostics and Health Management* 11 (1) (2023) Article 2605. [doi:10.36001/ijphm.2020.v11i1.2605](https://doi.org/10.36001/ijphm.2020.v11i1.2605).
- [101] P. T. Brewick, M. Abdelbarr, A. Derkevorkian, A. R. Kolaini, S. F. Masri, J.-S. Pei, [Fusing state-space and data-driven strategies for computational shock response prediction](#), *AIAA Journal* Published Online: 2 Mar 2018 (2018). [doi:10.2514/1.J056446](https://doi.org/10.2514/1.J056446).  
URL <https://doi.org/10.2514/1.J056446>

- 
- [102] A. Derkevorkian, A. R. Kolaini, P. T. Brewick, S. F. Masri, M. Abdelbarr, J.-S. Pei, A novel computational shock prediction approach using hybrid data-driven methodology, in: Proceedings of the European Conference on Spacecraft Structures, Materials and Environmental Testing (ECSSMET), ESTEC, Noordwijk, The Netherlands, 2018, p. N/A.
- [103] M. A. Biot, The elastic and viscoelastic response of systems to transient loads, *Journal of Applied Physics* 13 (6) (1942) 213–221.
- [104] D. E. Hudson, Response spectrum techniques in engineering seismology, in: Proceedings of the World Conference on Earthquake Engineering, 1956, p. N/A.
- [105] P. C. Jennings, G. W. Housner, N. C. Tsai, Simulated earthquake motions, Tech. rep., California Institute of Technology, Earthquake Engineering Research Laboratory, Pasadena, CA, USA (1968).
- [106] J. P. Den Hartog, *Mechanical Vibrations*, McGraw-Hill, 1956.
- [107] N. M. Newmark, A method of computation for structural dynamics, *Journal of the Engineering Mechanics Division, ASCE* 85 (EM3) (1959) 67–94.
- [108] Bureau of Ships, Shock design of shipboard equipment, dynamic design-analysis method, Tech. rep., Navy Department, Bureau of Ships, Washington, D.C., USA (1961).
- [109] Department of Defense, Mil-std-810g, environmental engineering considerations and laboratory tests, Tech. rep., Military Standard (2008).
- [110] National Aeronautics and Space Administration (NASA), NASA-STD-7003A: Pyroshock test criteria, Tech. rep., National Aeronautics and Space Administration (NASA) (2003).
- [111] H. Himmelblau, J. Manning, D. Kern, A. Piersol, Dynamic environmental criteria, Handbook NASA HDBK-7005, NASA (2001).
- [112] T. Irvine, Introduction to the shock response spectrum, vibrationdata (2000).
- [113] D. O. Smallwood, An improved recursive formula for calculating shock response spectra, *Journal of Sound and Vibration* 63 (3) (1979) 449–457.
- [114] D. O. Smallwood, A. R. Nord, Matching shock spectra with sums of decaying sinusoids compensated for shaker velocity and displacement limitations, *Shock and Vibration Bulletin* 44 (1974) 43–56.

- 
- [115] D. O. Smallwood, Shock testing on shakers by using digital control, Tech. rep., Institute of Environmental Sciences, Mount Prospect, IL, USA (1986).
- [116] J. E. Alexander, Shock response spectrum – a primer, in: IMAC-XXVII, 27th International Modal Analysis Conference, Society for Experimental Mechanics, Orlando, FL, 2009, p. N/A.
- [117] T. Irvine, Shock Response Spectrum Synthesis Via Damped Sinusoids, *Vibrationdata* (2012).
- [118] T. Irvine, Shock Response Spectrum Synthesis Via Wavelets, *Vibrationdata* (2000).
- [119] J. E. Alexander, A new method to synthesize an srs compatible base acceleration with energy and temporal moments to improve mdof system response, in: IMAC 36, Orlando, 2018, p. 7.
- [120] J. E. Alexander, A nonlinear ddam procedure, in: SAVIAC Proceedings of the 66th Shock and Vibration Symposium, Vol. 1, Biloxi, MS, USA, 1995, pp. 251–262.
- [121] D. Gasparini, E. H. Vanmarcke, Simulated earthquake motions compatible with prescribed response spectra, Tech. Rep. Pub. No. R76-4, Report No. 2, MIT, Department of Civil Engineering, evaluation of Seismic Safety of Buildings (1976).
- [122] A. K. Ghosh, On the generation of ground motion accelerogram compatible with a specified response spectrum and a fourier amplitude spectrum, in: SMiRT 11 Transactions, Vol. 11, 1991, pp. 7–12.
- [123] S. Levy, J. P. Wilkinson, Generation of artificial time-histories, rich in all frequencies, from given response spectra, *Nuclear Engineering and Design* 38 (1976) 241–251.
- [124] G. Kost, T. Tellkamp, A. Gantayat, F. Weber, Automated generation of spectrum-compatible artificial time histories, *Nuclear Engineering and Design* 45 (1978) 243–249.
- [125] R. H. Scanlan, K. Sachs, Earthquake time histories and response spectra, *Journal of the Engineering Mechanics Division* 100 (1974) 635–655.
- [126] A. Ranieri, Comparative study of shock response synthesis techniques for aerospace applications, in: Proceedings of the Aeronautics and Astronautics Conference, 2023, p. N/A. [doi:10.21741/9781644902813-159](https://doi.org/10.21741/9781644902813-159).

- [127] L. Hua-cha, [Research on the time-history waveform synthesis of shock response spectrum](#), Environmental Technology (2007).  
URL <https://api.semanticscholar.org/CorpusID:111433612>
- [128] Hale, Adhami, Time-frequency analysis in shock response spectrum synthesis, in: Proceedings of IEEE Conference, 1991, p. N/A.
- [129] A. Grasps, An introduction to wavelets, IEEE Computational Science and Engineering 2 (2) (1995).
- [130] M. S. Giuseppe Carbone, Mechanical System Dynamics, Politecnico di Bari, Department of Mechanics, Mathematics and Management, Bari, Italy, master's Degree Programme: Mechanical Engineering (2024).
- [131] European Cooperation for Space Standardization (ECSS), ECSS-E-HB-32-26A: Space engineering - Spacecraft mechanical loads analysis handbook, Tech. rep., European Cooperation for Space Standardization (ECSS) (Feb. 2013).
- [132] European Cooperation for Space Standardization (ECSS), ECSS-E-HB-32-25A: Space engineering - Mechanical shock design and verification handbook, Tech. rep., European Cooperation for Space Standardization (ECSS) (Jul. 2015).
- [133] H. Zhao, W. Liu, J. Ding, Y. Sun, X. Li, Y. Liu, Numerical study on separation shock characteristics of pyrotechnic separation nuts, Acta Astronautica 153 (2018) 383–392. doi:10.1016/j.actaastro.2018.07.040.
- [134] A. Messina, [Local diagnoses in modal analysis through additional poles](#), Mechanics of Advanced Materials and Structures Published online: 12 Jul 2019 (2019). doi:10.1080/15376494.2019.1614704.  
URL <https://doi.org/10.1080/15376494.2019.1614704>
- [135] A. Messina, L. Soria, G. Mantriota, [Experimental analyses on local diagnoses through additional poles extracted by r-frfs](#), Mechanics of Advanced Materials and Structures 28 (17) (2021) 1765–1774, published online: 27 Dec 2019. doi:10.1080/15376494.2019.1705448.  
URL <https://doi.org/10.1080/15376494.2019.1705448>
- [136] W. J. Yan, M. Y. Zhao, Q. Sun, W. X. Ren, Transmissibility-based system identification for structural health monitoring: Fundamentals, approaches, and applications, Mechanical Systems and Signal Processing 127 (2019) 327–356.

- 
- [137] S. D. Carolis, A. Messina, L. Soria, Modal analysis through response-based frfs: Additional modes for local diagnoses, *Journal of Sound and Vibration* 549 (2023) 117574.
- [138] G. Li, M. Cinefra, E. Carrera, Layerwise theories of laminated composite structures and their applications: A review, *Archives of Computational Methods in Engineering* 28 (2021) 577–600.
- [139] E. Carrera, M. Cinefra, G. Li, Mitc9 shell finite elements with miscellaneous through-the-thickness functions for the analysis of laminated structures, *Composite Structures* 154 (2016) 360–373.
- [140] M. Cinefra, M. C. Moruzzi, S. Bagassi, E. Zappino, E. Carrera, Vibro-acoustic analysis of composite plate-cavity systems via cuf finite elements, *Composite Structures* 259 (2021) 113428.